

**INTEGRATED GEOSCIENTIFIC STUDIES ON
UNCONVENTIONAL PERMIAN SHALE GAS RESOURCES
OF KOMMUGUEDEM AND MANDAPETA AREA, KRISHNA
GODAVARI BASIN, INDIA**

**A thesis submitted to the
*University of Petroleum and Energy Studies***

**For the award of the degree of
*Doctor of Philosophy***

**in
*Earth Science***

**by
SHUBHANGI KALA**

March 2022

**Supervisor (s)
Dr Javaregowda Devaraju
Dr Mohammed Abdul Rasheed**



**Department of Petroleum Energy and Earth Science
School of Engineering
University of Petroleum & Energy Studies
Dehradun-248007: Uttarakhand**

**INTEGRATED GEOSCIENTIFIC STUDIES ON
UNCONVENTIONAL PERMIAN SHALE GAS RESOURCES
OF KOMMUGUDEM AND MANDAPETA AREA, KRISHNA
GODAVARI BASIN, INDIA**

A thesis submitted to the
UNIVERSITY OF PETROLEUM AND ENERGY STUDIES

For the award of the degree of
DOCTOR OF PHILOSOPHY

in

EARTH SCIENCE

by

**SHUBHANGI KALA
(SAP ID- 500051008)**

March 2022

Internal Supervisor

DR JAVAREGOWDA DEVARAJU

Professor

**Department of Petroleum Engineering & Earth Sciences
University of Petroleum and Energy Studies**

External Supervisor

DR MOHAMMED ABDUL RASHEED

Scientist C

Petroleum Research Wing

Gujarat Energy Research and Management Institute



**Department of Petroleum Energy and Earth Science
School of Engineering
University of Petroleum & Energy Studies
Dehradun-248007: Uttarakhand**

DECLARATION

I declare that the thesis entitled “**Integrated geoscientific studies on unconventional Permian shale gas resources of Kommugudem and Mandapeta area, Krishna Godavari Basin, India**” has been prepared by me under the guidance of **Dr Javaregowda Devaraju**, Professor of Department of Petroleum Engineering & Earth Sciences, Energy Cluster-School of Engineering, University of Petroleum and Energy Studies and **Dr Mohammed Abdul Rasheed**, Scientist C of Petroleum Research Wing, Gujarat Energy Research and Management Institute. The content of this thesis has not been submitted elsewhere for the award of any degree or fellowship previously.



Shubhangi Kala

*Department of Petroleum Engineering & Earth Sciences
School of Engineering
University of Petroleum and Energy Studies
Dehradun-248007: Uttarakhand.*

DECLARATION

I declare that the thesis entitled “**Integrated geoscientific studies on unconventional Permian shale gas resources of Kommugudem and Mandapeta area, Krishna Godavari Basin, India**” has been prepared by me under the guidance of **Dr Javaregowda Devaraju**, Professor of Department of Petroleum Engineering & Earth Sciences, Energy Cluster-School of Engineering, University of Petroleum and Energy Studies and **Dr Mohammed Abdul Rasheed**, Scientist C of Petroleum Research Wing, Gujarat Energy Research and Management Institute. The content of this thesis has not been submitted elsewhere for the award of any degree or fellowship previously.

Shubhangi Kala

Department of Petroleum Engineering & Earth Sciences
School of Engineering
University of Petroleum and Energy Studies
Dehradun-248007: Uttarakhand.

CERTIFICATE

I certify that **Shubhangi Kala** has prepared her thesis entitled "**Integrated geoscientific studies on unconventional Permian shale gas resources of Kommugudem and Mandapeta area, Krishna Godavari Basin, India**" for the award of the PhD degree submitted to the University of Petroleum & Energy Studies, under my guidance. She has carried out work at the Department of Petroleum Engineering & Earth Sciences, University of Petroleum & Energy Studies. The content of this thesis has not been submitted elsewhere for the award of any degree or fellowship previously.



INTERNAL SUPERVISOR

Dr Javaregowda Devaraju

Professor

Department of Petroleum Engineering & Earth Sciences

Energy Cluster-School of Engineering

University of Petroleum and Energy Studies

Dehradun-248007, Uttarakhand.

Date: 8th March 2022

Energy Building,
Pandit Deendayal Petroleum University Campus,
Raisan Village, Gandhinagar - 382 007, Gujarat, INDIA
Phone : +91-79-23275757
Fax : +91-79-23275380
E-mail : information@germi.org
Website : www.germi.org

ISO 9001 : 2015 CERTIFIED



ENERGY EDUCATION
ENERGY RESEARCH & DEVELOPMENT
ENERGY TRAINING
ENERGY CONSULTANCY

N^o 003896

CERTIFICATE

I certify that **Shubhangi Kala** has prepared her thesis entitled **“Integrated geoscientific studies on unconventional Permian shale gas resources of Kommugudem and Mandapeta area, Krishna Godavari basin, India”** for the award of the PhD degree of the University of Petroleum & Energy Studies, under my guidance. She has carried out work at the Department of Petroleum Engineering & Earth Sciences, University of Petroleum & Energy Studies. The content of this thesis have not been submitted elsewhere for the award of any degree or fellowship previously.

EXTERNAL SUPERVISOR
Dr Mohammed Abdul Rasheed
Scientist C, Petroleum Research Wing
Gujarat Energy Research and Management Institute, Gandhinagar
Date: 8th March, 2022



ABSTRACT

Shales are major prospective unconventional reservoirs contributing globally as an alternative energy source. The contribution of natural gas production in the US and China shale gas industry has been globally impactful. Hence, shale gas prospect characterization has been initiated in Krishna-Godavari (KG), Damodar, Cambay, Cauvery and Vindhyan basins in India. Shale gas reserves exhibit complex lithological and microstructural heterogeneity with free or adsorbed gases of biogenic or thermogenic origin in matrix, pores and microfractures. The exploitation of unconventional reservoir is enormously challenging and require a systematic understanding of geological and petrophysical factors that can influence the gas storage capacity.

As per the Directorate General of Hydrocarbons (DGH), the KG Basin has reported hydrocarbon accumulations and exploration studies have led to the discovery of more than 225 prospective zones with 75 proven prospects. The KG Basin has immense potential for shale gas and oil exploitation where detailed compositional and pore structure heterogeneity studies were needed. Lower Gondwanan, Kommugudem Formation of the prolific KG Basin records complex, heterogeneous litho-unit of shale-sandstone-coal. Kommugudem shales from six deep borewells (i.e. Wells A, B, C, D, E and F) have been studied for the petrographical, organic geochemical and pore-associated parameters to elucidate the provenance, source rock properties and depositional settings, which provide significant insights on the shifts in the Gondwanan paleoenvironment and its climatic controls during the Early Permian. The possible control of pore characteristics by paleoenvironmental indices and their complex mechanisms were also attempted.

Thus, the present research is a systematic core sample investigation with methodology following four essential modules for enhanced gas shale reservoir

characterization. In the first phase of the study, extensive petrographic analysis to understand the mineralogical and elemental composition of Kommugudem shales was explored by various techniques like thin section studies, XRD, FE-SEM, XRF and ICPMS. Secondly, organic matter characteristics and source rock potential analysis were executed through RockEval supported by organic petrography, biomarker analysis and FTIR. In the third stage of the study, micro-, meso- and macro-pore characteristics were studied by low-pressure N₂ adsorption with FE-SEM as a supportive study. Finally, all the analyses were integrated to understand the sedimentary environment and its effect on pore characteristics.

Petrographically, the shales comprise silt-sized quartz, feldspar, mica, clay and organic matter with the carbonaceous and argillaceous matrix. Maceral identification reveals the dominance of vitrinite and inertinite, which is distinctive to organic-rich Permian Gondwana sediments. The main petrographic facies are carbonaceous shale, carbonaceous silty shale, silty shale and fine-grained micaceous sandstone. The XRD and FE-SEM analyses demonstrated the occurrence of siliceous mineral matter with low clay and carbonates. Organic mudstone classification implies that the formation comprises silica-dominated lithotype and clay-rich siliceous mudstone. The Kommugudem Formation's high mineralogical brittleness index postulates favourable conditions for hydraulic fracturing.

The chemical maturity index of selected shale samples revealed that the sediments were immature, having been derived and deposited close to the source without being recycled during sedimentation. This also implies that the Kommugudem shale has a higher concentration of detrital clay minerals. The CIA and CIW suggest moderate to strong weathering conditions during the deposition of Kommugudem shales. Al₂O₃/TiO₂ ratio and the La/Sc vs Th/Co plot suggest felsic volcanic rocks as the probable source of origin for the Kommugudem Formation. The paleoproductivity assessed using the P/Ti values ranges low in Kommugudem shales (<0.34) suggesting that reduced primary productivity characterized the sedimentary environment. The tectonic setting discriminatory

diagram of Log (K₂O/Na₂O) versus SiO₂ and La-Th-Sc ternary plot represents the deposition of sediments in a passive continental margin setting. A climatic shift from cold, arid to warmer post-glacial conditions is corroborated by the variation of $\delta^{13}C_{org}$, CIA, Sr/Cu and Ga/Rb ratios. Paleosaline proxy, Rb/K ratio indicates an influx of freshwater in the marine environmental system. Redox-sensitive elements dominantly indicate dysoxic to oxic water column conditions. These observations are consistent with the REEs as reflected by Europium and Cerium anomalies.

The RockEval pyrolysis investigation revealed the existence of primarily Type III kerogen in admixture with Type II-III and Type IV with high TOC and Tmax, implying the presence of substantial organic matter in the dry and wet gas windows. The vitrinite reflectance measurements also corroborate that mature to post-mature shale was dominant in the gas generation window. Owing to the higher TOC content, FTIR functional group analysis indicated the existence of aromatics and aliphatics in greater abundance. The RockEval parametric and FTIR study suggests that Wells A and B have excellent hydrocarbon generation potential for oil and gas sources, but Wells C, D, E and F have significantly lesser potential.

The elemental proxies supported by biomarkers are indicative of a fluvio-marine transitional environment that was preserved mainly under suboxic to oxic conditions. The depositional environment and climate, as interpreted in the Kommugudem sedimentary records, have important implications in envisaging these conditions for other stratigraphic equivalents in Gondwanan basins of peninsular India and adjoining landmasses of the Upper Early Permian age.

The N₂ adsorption isotherms indicate adsorption is low at low relative pressures and increases steadily exhibiting characteristics of a Type IV curve of IUPAC classification. The adsorption-desorption hysteresis loop indicates the abundance of micropores and mesopores with the presence of complex slit and cylindrical pores also supported by FE-SEM results. The BET-specific surface area (BET – SSA) ranges between 2.47 m²/g to 24.57 m²/g, total pore volume (total PV) ranges between 0.012 cc/g to 0.78 cc/g, micropore volume ranges between 0.00051 cc/g

to 0.0044 cc/g and average pore diameter ranges between 36.08 nm to 26.22 nm. Fractal dimensions estimated for all the samples vary between 2 and 3 with an average value of 2.65, indicating that the samples are rough and exhibit complex and heterogeneous pore structures. The FE-SEM assessments revealed the existence of microfractures and micropores in the form of inter and intragranular pore sites in mineral and organic matter, which might function as hydrocarbon storage sites. Natural microfracture presence in Kommugudem may augment hydraulic fracturing efficiency by providing a migration pathway for hydrocarbons. The clay, TOC and Tmax have a positive correlation with micropore volume indicating a good contribution of clay micropore and associated organic matter. Poor correlation of trace elements with Tmax and TOC was observed which may be the result of a statistically low number of samples. The REEs and Cr exhibit a probable role in the pore genesis of silicate minerals supporting the positive effect of the environment. The redox proxies are strongly correlated with TOC and total PV indicating possible development of organopores, also supported by FE-SEM imagery indications. Thus, stated investigations indicate complex mechanisms with possibly significant influence of the sedimentary environment, climate, redox and salinity conditions on pore characteristics. Though further investigations are required with more extensive data to demonstrate better insight into paleoenvironmental influence.

Keywords: Mineralogical brittleness index, paleoclimate, paleoenvironment, pore characterization, hydrocarbon potential.

ACKNOWLEDGEMENTS

I would like to express my gratitude to my revered PhD supervisors, Dr J. Devaraju and Dr M. A. Rasheed for their persistent guidance and encouragement throughout my research journey. They have put enormous efforts in guiding me on research and people skills required ahead in the professional sphere of life. My PhD journey would not be worthy without the consistent support of Dr D. M. Tiwari, UGC Assistant Professor, University of Hyderabad. In the meagre time I have known her she has educated me on paper writing skills, analytical thinking and enhanced research aptitude that has helped build my confidence and become a qualified researcher. The immense support and guidance of my supervisors and Dr Mani have moulded me to be a better, self-reliant, balanced version and accomplish my research goals.

I thank the Department of Science and Technology for financial support by awarding the INSPIRE Fellowship (IF160661). Dr S. J. Chopra (Chancellor), Dr Gurvinder Singh Virk (Dean-SOE) and Dr D. K. Avasthi (R&D-Dean), UPES are acknowledged for providing infrastructural and instrumental support. I am extremely grateful to Dr J.K. Pandey, (presently, Pro-Vice-Chancellor, Adamas University) and the R&D team at UPES for continuous encouragement and support through all stages of PhD work. I would also like to thank the faculty and non-faculty staff of the Department of Petroleum Engineering & Earth Sciences for consistent support. It gives me immense pleasure to thank Dr D.N. Singh (HOI-KDMIPE), Dr K.K. Das (Retired General Manager, GM), Mr K. Yadagiri (Retired GM) and Mr S. Uppal (Retired GM) from ONGC for providing samples and well-related data. Mr Harbir Singh (Retired GM) and Mr Natarajan Munusamy (GM), ONGC are acknowledged for RockEval and FE-SEM analysis respectively. Drs. Pradeep Srivastava (Associate Professor, IIT-Roorkee) and A.K. Singh (Scientist-

E) are acknowledged for C-isotope and elemental analysis at WIHG, Dehradun. Dr R. P. Mathews (Scientist-C) is acknowledged for biomarker analysis at BISP, Lucknow and Dr Keshav Krishna A. (Principal Scientist) for XRF analysis at NGRI, Hyderabad, India. I would also especially like to thank Dr K. M. Reddy, Associate Professor-Chemistry, UPES for allowing lab access and guidance on biomarker-associated interpretations.

I wish to convey a special word of thanks to friends and collaborators, Mr V. Y. Turlapati, Dr S. De and Dr N. Lakhan. I am tremendously grateful for them standing by my ideas and working synchronously to achieve our common goals. Many thanks to Dr Jaquilin Joseph, Dr Siddharth Prizomwala, Dr Avinash Chauhan, Ms Apurva Shitole, Ms Aashima Sodhi and Ms Manisha Chaudhary for inspiration, insightful discussions and encouragement through various stages of research work. Also especially thankful for patient friends and support system, Mr Naresh Sharma, Mr G.B. Hermon, Dr Dipin Kasana, Ms Sukruti Khadepav, Mr Uday Kiran, Dr Shantanu Bhowmik, Dr Mainak Mukherjee, Mrs Meenakshi Pundir, Mr Madam Chakradar and Mr Vinay Dwivedi. Massive gratitude to all my dear friends and colleagues for their unceasing encouragement.

Saving the best for last, I am forever indebted to the most loving and supportive parents, grandparents and siblings that are responsible for making me a decent being. They have seen me burn the midnight oil and stood by my supposedly whimsy decisions. I love you Mr P.K. Kala and Mrs Rama Kala and I dedicate all my life's work to you.

Dedicated to my forebears and parents

TABLE OF CONTENTS

DECLARATION.....	ii
CERTIFICATE.....	iii
ABSTRACT.....	v
ACKNOWLEDGMENT.....	ix
TABLE OF CONTENTS.....	xii
LIST OF FIGURES.....	xvi
LIST OF TABLES.....	xx
LIST OF SYMBOLS AND ABBREVIATIONS.....	xxii
CHAPTER 1: INTRODUCTION.....	1
1.1 Preamble.....	1
1.2 Research gap.....	4
1.3 Objectives.....	5
1.4 Scope of the study.....	5
1.5 Work plan.....	8
1.6 Organization of the thesis: Chapter scheme.....	9
CHAPTER 2: LITERATURE SURVEY.....	10
2.1 Introduction: Shale gas reservoir fundamentals.....	10

2.2 Critical appraisal of the state of the art.....	13
2.3 Shale gas scenario in India.....	16
2.4 Geology of the study area.....	19
2.5 Geological settings and stratigraphy.....	20
CHAPTER 3: MATERIALS AND METHODS.....	23
3.1 Chapter overview.....	23
3.2 Study area and core samples.....	23
3.3 Megascopic study.....	25
3.4 Thin section analysis.....	25
3.5 X-Ray Diffraction (XRD) analysis.....	25
3.6 Field Emission Scanning Electron Microscope (FE-SEM) analysis.....	25
3.7 X-Ray fluorescence (XRF) analysis.....	26
3.8 Inductively Coupled Plasma Mass Spectrometry (ICP-MS) analysis...	26
3.9 RockEval Pyrolysis.....	26
3.10 Vitrinite reflectance analysis.....	27
3.11 Biomarker extraction and analysis.....	27
3.12 Kerogen isolation and bulk carbon isotope ($\delta^{13}\text{C}_{\text{org}}$) analysis.....	28
3.13 Fourier-transform infrared spectroscopy (FTIR) analysis.....	28
3.14 Low-pressure N_2 adsorption analysis (LPNA)	29
CHAPTER 4: MINERALOGICAL AND ELEMENTAL ANALYSIS	32
4.1 Chapter overview.....	32
4.2 Megascopic characterization.....	32

4.3 Petrographic analysis of mineral matter.....	33
4.4 Mineralogical composition and associated brittleness index.....	35
4.5 FE-SEM associated morphological and mineralogical characteristics.....	40
4.6 Major oxides.....	42
4.7 Trace and rare earth elements analysis.....	46
4.7.1 Detrital proxy and tectonic setting.....	48
4.7.2 Paleoredox conditions.....	50
4.7.3 Paleoclimate and paleosalinity.....	52
CHAPTER 5: ORGANIC GEOCHEMICAL ANALYSIS.....	54
5.1 Chapter overview.....	54
5.2 RockEval-based source rock characteristics.....	54
5.3 Maceral and vitrinite reflectance studies.....	58
5.4 Biomarker analysis.....	62
5.5 Stable carbon isotope ratios ($\delta^{13}\text{C}_{org}$).....	65
5.6 Functional groups assessment.....	66
CHAPTER 6: PORE-ASSOCIATED ANALYSIS.....	69
6.1 Chapter overview.....	69
6.2 Low-pressure N ₂ adsorption.....	69
6.3 Fractal analysis.....	71
6.4 Pore morphology.....	72
CHAPTER 7: DISCUSSIONS.....	74

7.1 Chapter overview.....	74
7.2 Paleoclimate and depositional environment.....	74
7.3 Paleoceanography and organic productivity.....	79
7.4 Mineral assemblage and their influence on pore structure parameters.....	82
7.5 Source rock characterization and its influence on pore structure parameters.....	84
7.6 Thermal maturity effect on trace element enrichment.....	85
7.7 Paleoenvironmental indices and their influence on pore parameters.....	86
CHAPTER 8: CONCLUSIONS AND FUTURE SCOPE.....	89
8.1 Conclusions.....	89
8.2 Future work.....	90
REFERENCES.....	92
APPENDIX.....	113
CURRICULUM VITAE WITH LIST OF PUBLICATIONS.....	135

LIST OF FIGURES

Fig. 1.1 Work accomplished and the novelty.....	7
Fig. 1.2 (a) Work plan and (b) location of accomplishment.....	8
Fig. 2.1 Geological map of the KG Basin in the backdrop of Gondwana basins of peninsular India (modified after Gupta, 2006).....	21
Fig. 2.2 Generalized litho-stratigraphy of Kommugudem Formation, KG Basin.....	22
Fig. 3.1 Photomicrographs indicating core samples in cross-section: a) Carbonaceous shale; b) & c) Mica-rich carbonaceous shale; d) Fe-rich shale; Longitudinal view of e) Carbonaceous shale; f) Sandy-shaly intercalation.....	24
Fig. 4.1 Photomicrographs in the cross-polarized light show a) poorly sorted quartz and mica grain floating in a matrix of organic matter; b) clay-sized microquartz in association with carbonaceous and argillaceous matrix; c) silt-sized and clay-sized quartz (subangular-subrounded), feldspars and mica with argillaceous matrix; d) silt-sized quartz associated with mica grains displaying parallel lamination with carbonaceous and argillaceous matrix.....	34
Fig. 4.2 (a) XRD crystallograph (B/C2/B8 sample) representing distinct mineral phases. Abbreviations: I: Illite; K: Kaolinite; F: Feldspar; C: Chlorite; Q: quartz; D: Dolomite; S: Siderite and P: Pyrite; (b) sCore lithotype classification (modified after Gamero Diaz et al., 2013) with superimposition of ternary diagram of mineralogical composition from the selected Kommugudem shale samples. Abbreviations: QFM= sum of the weight percentage of quartz, feldspars and mica.....	36

Fig. 4.3 (a) Ternary plot showing the range of composition from selected Kommugudem shale samples, Barnett, Eagle Ford and a clay-rich mudrock (modified from Passey et al., 2010); (b) Ternary plot with classification for organic mudstones (modified after Allix et al., 2010) displaying average composition of the main shale plays from North America and Kommugudem shale.....	39
Fig. 4.4 FE-SEM photomicrograph representing (a) Feldspar laths in the argillaceous matrix with intergranular pores; (b) Spongy network of organic matter with intragranular pores; (c) and (d) Kaolinite and illite clay with intergranular pores respectively; (e) and (f) Pyrite framboids; (g) Silica occurring as over-growth grains or recrystallized silica exhibiting dissolution pores; (h) Natural microfracture developed in quartz grain.....	41
Fig. 4.5 Lithological classification of Kommugudem shales based on the chemical composition of $\text{SiO}_2/\text{Al}_2\text{O}_3$ versus $\text{Fe}_2\text{O}_3/\text{K}_2\text{O}$ (modified after Herron, 1988).....	43
Fig. 4.6 (a) Ternary diagram showing relative proportions of quartz-clay-carbonates in Kommugudem shales; (b) Ternary diagram showing the relative proportion of $\text{Al}_2\text{O}_3\text{-CaO+Na}_2\text{O-K}_2\text{O}$ in Kommugudem shales. UCC = upper continental crust and PAAS = Post Archaean Australian shales (modified after Nesbitt & Young, 1984).....	45
Fig. 4.7 Tectonic discriminatory diagram ($\text{Log K}_2\text{O/Na}_2\text{O vs. SiO}_2$) for Kommugudem samples (modified after Roser & Korsch, 1986).....	46
Fig. 4.8 PAAS normalized REE concentration (ppm) in Kommugudem Formation, KG Basin.....	47
Fig. 4.9 (a) La-Th-Sc ternary plot visualizing tectonic setting for Kommugudem Formation where, A, B, C and D represent oceanic island arc, active continental margin, continental arc and passive margin respectively (modified after Bhatia & Crook, 1986) and (b) La/Sc vs Th/Co plot indicating felsic volcanic rocks as the source of origin for Kommugudem Formation (modified after Cullers and Podkovyrov, 2000).	49

Fig. 4.10 (a) Ni vs V correlation (ppm) indicating the depositional nature of Kommugudem shales; (b) EF _U vs EF _{MO} in Kommugudem shales reflecting the paleoredox conditions (modified after J. Ding et al., 2018).....	51
Fig. 5.1 (a) Hydrogen index-Oxygen index cross plot indicating the type of hydrocarbon generation for the Kommugudem Formation (modified after Espitalié, 1986); (b) Hydrogen index-Tmax cross plot showing maturity range and kerogen type (modified after Espitalié, 1986).....	55
Fig. 5.2 Production Index-Tmax cross plot (modified after Peters & Cassa, 1994).....	56
Fig. 5.3 (a) S ₂ -TOC cross plot (wt %) indicating hydrocarbon potential of the Kommugudem Shale (after Hunt, 1996; Peters, 1986); (b) HI-TOC cross plot indicating hydrocarbon potential of the Kommugudem shale.....	57
Fig. 5.4 S ₁ vs. TOC correlation of organic components in Kommugudem Shales.....	58
Fig. 5.5 Photomicrograph exhibiting a) dominant accumulation of collotellinite (Cot); b) collotellinite and vitrodetrinite (Vd) in association with semifusinite (Sf), micrinite (Mic) and inertodetrinite (Ind) and sporinite (Sp); c) collotellinite assemblage with vitrodetrinite and inertodetrinite; d) Sporinite, resinite (R) and liptodetrinite (Ld) accumulation.....	59
Fig. 5.6 (a) Mean vitrinite reflectance-Depth cross plot for Kommugudem shale (modified after Peters and Cassa, 1994); (b) Vitrinite reflectance-Tmax cross plot for the Kommugudem shale.....	61
Fig. 5.7 A representative total ion chromatogram (B4/C1/B8) indicating n-alkane peaks in the organic extract of the Kommugudem shale.....	62
Fig. 5.8 (a) Pristane/n-C ₁₇ and Phytane/n-C ₁₈ cross plot signifying depositional environment of Kommugudem shales; (b) Aromatic biomarker ratios (Dibenzothiophene/Phenanthrene vs Pristane/Phytane) indicating the depositional environment of Kommugudem shales.....	64

Fig. 5.9 (a) FTIR spectra of a representative sample from each well. Abbreviations: 1. Kaolinite, 2. Hydroxyl group, 3. Aromatic C-H stretching, 4. Aliphatic C-H stretching, 5. Carbonyl/Carboxyl group, 6. Aromatic C=C stretching, 7. Aliphatic CH₂ and CH₃ bending, 8. Quartz, 9. Feldspar + Quartz, 10. Kaolinite, 11. Quartz, 12-13. Kaolinite and 14. Quartz; (b) Genetic potential (GP) versus Index for hydrocarbon generation (IHG) plot of the studied shale samples (modified after Misra et al., 2018)..... **68**

Fig. 6.1 Low-pressure N₂ adsorption/desorption isotherms of Kommugudem shale samples..... **70**

Fig. 6.2 Pore size distributions estimated from desorption data using BJH model of all samples..... **71**

Fig. 7.1 (a) SiO₂ vs. Al₂O₃+K₂O+Na₂O plot of samples from Kommugudem Formation depicting paleoclimate conditions; (b) Sr/Cu vs. Ga/Rb cross plot depicting the paleoclimate conditions during the deposition of Kommugudem Formation (modified after J. Ding et al., 2018)..... **77**

Fig. 7.2 Depositional setting of Kommugudem shales based on log(MgO/Al₂O₃) and log(K₂O/Al₂O₃) ratios. DP= Devonian marine pelites, DSGP= Devonian marine subgreywacke pelites and PAAS = Post Archaean Australian shales (modified after Roaldest, 1978)..... **78**

Fig. 7.3 (a) Gondwana continental assemblage during Early Permian showing possible marine incursion pathways (indicated by green arrows) in KG Basin; (b) Variation of TOC, CIA and δ¹³C_{org} in Kommugudem shales of KG Basin..... **81**

LIST OF TABLES

Table 3.1 Summary of experimental procedures and associated results attained.....	113
Table 4.1 Semi-quantitative mineral assessment (%) and associated brittleness index for selected Kommugudem shale samples.....	115
Table 4.2 Major Oxide distribution (wt %) in the Kommugudem Formation.....	120
Table 4.3 Depositional environment and paleoproductivity parameters for Kommugudem shales.....	121
Table 4.4 Aluminum normalized trace elements concentration (ppm) in Kommugudem Formation.....	123
Table 4.5 REE concentrations (ppm) in Kommugudem Formation, KG Basin.....	124
Table 4.6 Paleoredox, paleoclimate and paleosalinity indicators are considered in Kommugudem shales of the KG Basin.....	125
Table 5.1 RockEval-VI pyrolysis data of the Kommugudem Formation. Abbreviations: S1 = total free hydrocarbon; S2 = hydrocarbon released by cracking of kerogen; S3 = organic carbon dioxide; Tmax =Temperature at which the maximum amount of pyrolyzed hydrocarbon (S2 peak) is generated from the kerogen; Hydrogen Index, HI= $[100 \times S2]/TOC$; Oxygen Index, $OI=[100 \times S3]/TOC$; Production Index, $PI = S1/[S1+S2]$; TOC= Total organic carbon; Generation potential, $GP= S1+S2$; PC: Principle carbon content ; RC: Residual carbon content.....	126
Table 5.2 Vitrinite reflectance data of shale samples from the Kommugudem Formation.....	129

Table 5.3 <i>n</i> -alkane biomarker ratios for Kommugudem shales.....	130
Table 5.4 Peak assignment of absorbance of the shales from FTIR spectral analysis. Abbreviations: M=medium and W=weak.....	131
Table 6.1 Pore characterization parameters estimated from low-pressure N ₂ adsorption isotherm experiment.....	134

LIST OF SYMBOLS AND ABBREVIATIONS

List of Symbols

$\delta^{13}\text{C}_{org}$	Stable carbon isotope ratio
EF_U	Uranium Enrichment Factor
EF_{MO}	Molybdenum Enrichment Factor
Cot	Collotellinite
Vd	Vitrodetrinite
Sf	Semifusinite
Mic	Micrinite
Ind	Inertodetrinite
Sp	Sporinite
R	Resinite
Ld	Liptodetrinite
P_o	Saturation vapor pressure, bar
P	Experimental pressure, bar
V	Volume of gas adsorbed, cc/g
V_m	Monolayer volume, cc/g
C	BET constant
a_m	Cross-sectional area occupied by Nitrogen molecule
L	Avogadro number
t	Statistical thickness, nm
R	Universal gas constant
V_L	Molar volume of the liquid absorptive, cc/g
γ	Liquid surface tension
D	Fractal Dimension
V_{qtz}	Volume of quartz

V_{dolomite}	Volume of dolomite
V_{clay}	Volume of clay
V_{calcite}	Volume of calcite
V_{TOC}	Volume of Total Organic Content
W_{QFM}	Weight percentage of quartz-feldspars-mica
W_{CAR}	Weight percentage of carbonate minerals
W_{CLAY}	Weight percentage of clay minerals
R²	Coefficient of determination
S1	Total free hydrocarbon
S2	Hydrocarbon released by cracking of kerogen
S3	Organic carbon dioxide

List of Abbreviations

KG	Krishna-Godavari
DGH	Directorate General of Hydrocarbon
Tcf	Trillion cubic feet
XRD	X-Ray Diffraction
FE-SEM	Field Emission Scanning Electron Microscope
XRF	X-Ray Fluorescence
FTIR	Fourier-Transform Infrared Spectroscopy
CIA	Chemical Index of Alteration
CIW	Chemical Index of Weathering
TOC	Total Organic Carbon
T_{max}	Temperature of the maximum of the Rock-Eval S2 peak, °C
IUPAC	International Union of Pure and Applied Chemistry
BET-SSA	BET surface area, <i>m</i> ² / <i>g</i>
PV	Pore Volume
REE	Rare Earth Element

ICP-MS	Inductively Coupled Plasma Mass Spectrometry
LPNA	Low-Pressure N ₂ Adsorption Analysis
UCC	Upper Continental Crust
PAAS	Post Archaean Australian Shales
HI	Hydrogen Index
GP	Genetic Potential
IHG	Index for Hydrocarbon Generation
BJH	Barrett-Joyner-Halenda
DP	Devonian Marine Pelites
DSGP	Devonian Marine Subgreywacke Pelites
OI	Oxygen Index
PI	Production Index
PC	Principle Carbon Content
RC	Residual Carbon
EIA	U.S. Energy Information Administration
OET	Oxygen exposure time
MBI	Mineralogical brittleness index
PSD	Pore size distribution
GC-MS	Gas Chromatography–Mass Spectrometry
GC-IRMS	Gas Chromatography Combustion Isotope Ratio Mass Spectrometry
RSD	Reproducibility Standard Deviation
ESH	Enhanced Slow Heating
FHR	Fluid-Like Hydrocarbon Residue
TEM	Transmission Electron Microscope
CT	Computed Tomography
FIB-SEM	Focused Ion Beam Scanning Electron Microscopy
MICP	Mercury Intrusion Capillary Porosimetry
SAXS	Small-Angle X-Ray Scattering
NMR	Nuclear Magnetic Resonance

LPGA	Low-Pressure Gas Adsorption
PG	Pranhita-Godavari
ICDD	International Centre For Diffraction Data
SE	Secondary Electron
BSE	Back Scattered Electron
LOI	Loss on Ignition
FHH	Frenkel-Halsey-Hill
BI	Brittleness Index
AS	Average Shale
CMI	Chemical Maturity Index
EF	Element Enrichment Factor
TCP	Terrigenous Component Percentage
ICV	Index Of Compositional Variability
LREE	Light Rare Earth Elements
HREE	Heavy Rare Earth Elements
LILE	Large-Ion Lithophile Elements
ICCP	International Committee for Coal and Organic Petrology
CPI	Carbon Preference Index
OEP	Odd-to-Even Predominance Ratio
OM	Organic Matter
PAH	Polycyclic Aromatic Hydrocarbon
IAL	Index for Aliphaticity
IAR	Index of Aromaticity
TAR	Terrigenous Aquatic Ratio
ACL	Average Chain Length Index

CHAPTER 1: INTRODUCTION

1.1 Preamble

Shale gas reserves are a worldwide promising energy source and shale gas resource exploration is in the budding stage in India. Exploration and production of shale gas is critical to meeting rising energy demands. India's risked, technically recoverable gas shale deposits are estimated to be 96 Tcf, with the most likely reserves in the basins of Assam-Arakan, Krishna-Godavari, Cambay, Cauvery, Gondwana, Vindhyan, Rajasthan and Bengal (DGH, 2012; EIA, 2013). Exploration in the Krishna-Godavari Basin led to the discovery of 225 prospects with proven hydrocarbon accumulations in 75 prospects (22 oil and 53 gas) (DGH, 2012; Rao, 2001). Thus, ONGC intends to drill 17 shale gas and oil wells with 11, 5 and 1 well in the Cambay, Krishna-Godavari and Cauvery basins respectively (Economic Times, 2016). Due to the probable abundance of hydrocarbon and coal reserves over a wide areal extent, the Permian aged (Lower Gondwana), Kommugudem Formation is being considered a promising gas shale prospect in India (DGH, 2012).

Shale gas reserves are a source-reservoir complex system comprising lithological heterogeneity with free or adsorbed gases of biogenic or thermogenic origin in the matrix, pores and microfractures (J. B. Curtis, 2002; Jarvie et al., 2007; Josh et al., 2012). Natural gas is stored in shale reservoirs in a) organic matter and clay minerals (adsorbed gas state) and b) natural fractures and large mineral pores (free state) (Clarkson & Haghshenas, 2013; Leahy-Dios et al., 2011; T. Zhang et al., 2012). Natural gas gets irregularly distributed among the pores of varied morphology and sizes due to the complex heterogeneous composition exhibited in shale reservoirs (Wei et al., 2018). Identifying the diverse and complicated pore

characteristics can lead to a better understanding of flow in porous medium and its storage capacity thereby leading to profitable hydraulic fracturing operations (Liu et al., 2018, 2019; Liu & Ostadhassan, 2017a, 2017b). As natural gas may get stored in pores and flows through connected pores, pore-associated analysis is critical. Utilizing Low-Pressure N₂ Adsorption (LPNA) isotherms and Field Emission Scanning Electron Microscope (FE-SEM) images, pore characteristics, including fractal dimensions are determined in the present study.

Shale constitutes complicated pore structure also reliant on sedimentation intricacies (Abarghani et al., 2018, 2020; X. Li et al., 2020; Shao et al., 2017; Yu et al., 2020). The concentration and distribution of trace elements and REEs throughout the formation provide vital information on paleoenvironmental conditions. Additionally, compositional heterogeneity is influenced by varying physical and chemical properties in depositional settings of shales (Loucks et al., 2009; Yu et al., 2020). Sedimentary facies, paleoredox setting, paleoclimate, paleoproductivity and paleosalinity influence pore attributes (Yu et al., 2020). The preservation of variable minerals and organic matter during the deposition is dependent on paleoredox conditions (Abarghani et al., 2018, 2020; Hazen et al., 2008). The oxygen exposure time (OET) influences the preservation mechanism of organic matter being dependent on paleoredox and paleoproductivity (S. Zheng et al., 2020). The paleosalinity and paleoclimate of the sedimentary water medium regulate certain trace elements, which in turn have an impact on the pore attributes (Tuttle et al., 2014). Consequently, comprehension of paleoenvironmental influence on pore attributes and identification of influencing factors is critical. The paleoenvironmental indices were computed using mineralogical composition and elemental concentrations measured using X-Ray Diffraction (XRD), X-Ray Fluorescence (XRF) And Inductively Coupled Plasma Mass Spectroscopy (ICP-MS) analysis.

Systematic laboratory characterization of gas shales for resource evaluation is essential based on qualitative and quantitative data to ascertain organic and mineral matter abundance, associated mineral texture, mechanical properties (brittleness)

and petrophysical properties (porosity and permeability) (Josh et al., 2012). Mineralogical composition and associated microstructures were analyzed by thin section, XRD and FE-SEM. Brittleness of gas shale reserves is dependent on mineralogical composition, elastic, mechanical properties, pore and fracture existence and has a substantial impact on hydraulic fracturing (Z. Guo et al., 2012). Shale brittleness is furthermore impacted by the mineral texture, dependent on intricate postdepositional processes (Milliken et al., 2012; Peng et al., 2020). The mineralogical brittleness index (MBI) investigation in the present study is brittleness/ductility assessment of gas-bearing shales vital for fracture initiation and propagation understanding (Britt et al., 2009). Quartz-rich shales tend to be brittle with relatively easy fracture development and do not self-seal, as detected in clay-rich shales (more ductile) (Kumar et al., 2018; Ross & Bustin, 2008). Comprehensive geochemical analysis based on RockEval, maceral, biomarker and FTIR studies quantifies the organic matter type and abundance, thermal maturity and source rock potential.

The current study takes into account the petroliferous Kommugudem Formation with shale-sand-coaly sequence formed in a transitional environment (Gupta, 2006; Prasad et al., 2000). The transitional environment investigations provide a distinctive perspective in analyzing the depositional environment's role on pore characteristics of variable sedimentary facies. Stratigraphic palynology has been comprehensively adopted to understand the depositional environment of the Kommugudem Formation in the KG Basin. Diverse perspectives have been expressed, based on their lateral equivalents. Deltaic-lacustrine, fluvio-lagoonal and/or transitional marine-lagoonal depositional environments have been suggested based on the spores of terrestrial land plants representing pteridosperms and the apparent lack of marine fossils (Prasad et al., 2000). Petrological investigations in concurrence with the geochemical proxies along the stratigraphic formations offer essential resolution where significant biostratigraphic markers are deficient. The variations in the Lower Gondwanan depositional environment and paleoclimate and the possible continental-marine transition in the Eastern Indian continental

margin were revealed by the multiproxy approach. Such implications are also applicable to the stratigraphic equivalent Gondwana formations of peninsular India and adjoining regions of the Early Permian age.

Previously, detailed pore attribute characterization of the Kommugudem Formation and its relationship with geochemical and petrographic assessments had not been reported. In the current study, qualitative and quantitative estimation of representative samples from six deep borewells by petrographic, geochemical and pore-associated analysis was carried out. This was followed by the integration and correlation of organic and inorganic matter associated attributes, hydrocarbon potential, pore attributes and paleoenvironmental indices.

1.2 Research gap

There is a lack of systematic geo-scientific evaluation of shale gas resources of the Kommugudem Formation of Krishna-Godavari Basin, India. The unconventional shale reservoir exhibits complex lateral heterogeneity in composition, texture, pores and kerogen characteristics. Each shale play is unique with wide variations observed within the same play as well as different shale formations. Thus, current work aims to bridge the gap by carrying out an integrated geo-scientific study on the aforementioned characteristics in Permian aged alternations of organic matter-rich shales of Kommugudem Formation in the Bhimadolu and Mandapeta troughs of the KG Basin. These Permian shales have been selected based on the published data indicating the presence of substantial organic matter and organic-rich interval with thickness up to 1000 feet covering the prospective areal extent of 4340 mi² (EIA, 2011). This makes the Kommugudem Formation a lucrative site amongst the potential shale gas-producing prospects from various basins of India.

Based on a thorough literature survey following gaps were observed:

1. Lack of thorough understanding of mineralogical and elemental set-up of Kommugudem shale and its associated brittleness.
2. Comprehensive hydrocarbon potential and petrophysical characterization of Kommugudem shales.

3. Assessment of sedimentary environmental setup and its influence on the above stated.

1.3 Objectives (approved by DST and UPES Research Committee)

The following objectives were adopted to address the research gaps:

Objective I: Petrographical analysis for reservoir characterization.

Objective II: Geochemical analysis for estimating organic matter type and abundance, thermal maturity and hydrocarbon potential.

Objective III: Integration of geochemical and petrographical factors and correlation with key geological factors and processes to validate shale gas prospects in the KG Basin.

1.4 Scope of the study

The KG Basin is a category-I basin that is critical to India's energy security. The discovery of the gas shale well RNSG-1 in the Damodar Valley Basin has piqued the interest of Indian researchers in other Category-I basins (Bakshi et al., 2018; Padhy et al., 2013). Thus, Permian shales of the Kommugudem Formation were chosen based on published data indicating a significant organic-rich interval and a massive prospective areal extent.

Although many researchers have reviewed and characterized prospective gas shale formations around the world, the relationship between organic-inorganic matters, associated depositional setting and pore attributes is not well understood. Comprehensive microscale characterization of organic-inorganic pores can eventually lead to a better understanding of sorption, gas entrapment and flow behaviour. Such assessments are imperative if gas production, enhanced shale gas recovery and/or carbon capture storage are to be considered in a basin. Each shale play is distinct, with wide lateral variations within the same play and different shale formations. As a result, there are no standard classifications based on shale composition and each formation must be thoroughly analyzed.

Thus, the Permian shales of the KG Basin were characterized based on their organic-inorganic constituents, associated depositional setting and influence on

pore attributes (Fig. 1.1). Shale core samples from the Lower Permian Kommugudem Formation of the KG Basin were collected for multiple analyses in this study. The assessment of source rock characteristics was based on the findings of RockEval pyrolysis, biomarker, FTIR, carbon isotope and vitrinite reflectance analyses. The mineral matter and elements were determined using petrographic, FE-SEM, XRD, XRF and ICPMS analysis. LPNA isotherm supported by FE-SEM studies characterizes the pore volume, specific surface area and pore size distribution. The relationships between mineralogical, organic composition, pore parameters and depositional setting of Permian gas shales from the KG Basin were deduced using the critical data analyses presented in this thesis.

The Kommugudem Formation has been studied as a “source rock” so far and in the present study, its nature as a “reservoir” was observed. Moreover in India, shale gas characterization emphasis has been concentrated on the Raniganj and Barakar Formations of the Damodar Basin. Thus, in the present study of the Kommugudem Formation comprehensive petrographic, pore attribute and geochemical signatures were assessed due to significant organic-rich interval and a massive prospective areal extent. The hydrocarbon potential and zones of interest were categorized where two of the six wells have fair to excellent potential for gas. Facies and mineralogical assessments lead to the identification of brittle zones. Microfractures and micropores formed in organic matter and minerals have been identified as potential hydrocarbon storage sites. Natural microfractures in Kommugudem Formation may augment hydraulic fracturing efficiency by providing a migration pathway for hydrocarbons. Paleoredox and paleoclimate studies revealed marine influx in fluvial-dominated Lower Gondwana during the Early Permian. The predominant contribution of micropore in clay and associated organic matter with the limited role of quartz was identified. The probable role of REEs and Cr in the pore genesis of silicate minerals supports the positive influence of the sedimentary environmental system. The redox proxies supported by FE-SEM imagery indicate the possible development of organopores.

Thus, based on stated inferences wells A and B seem to have relatively higher hydrocarbon potential and good brittleness signatures. These wells can be promising sites for gas shale exploration as well as future carbon storage sites. Further detailed geomechanical characterization can give a better representation of the prospectivity.

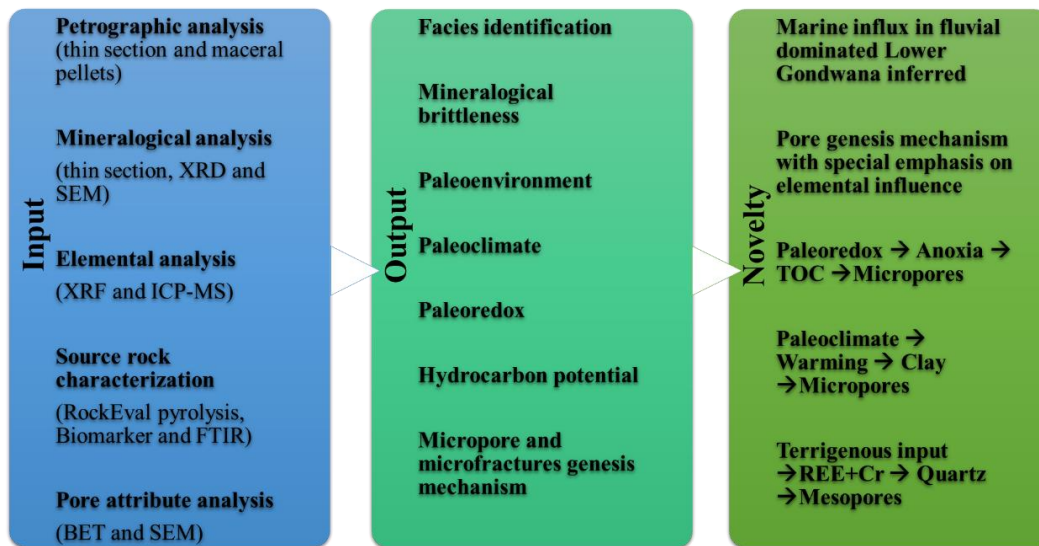


Fig. 1.1 Work accomplished and the novelty.

1.5 Work plan

The flow of work and their location of accomplishment are given in pictorial format in Fig. 1.2.

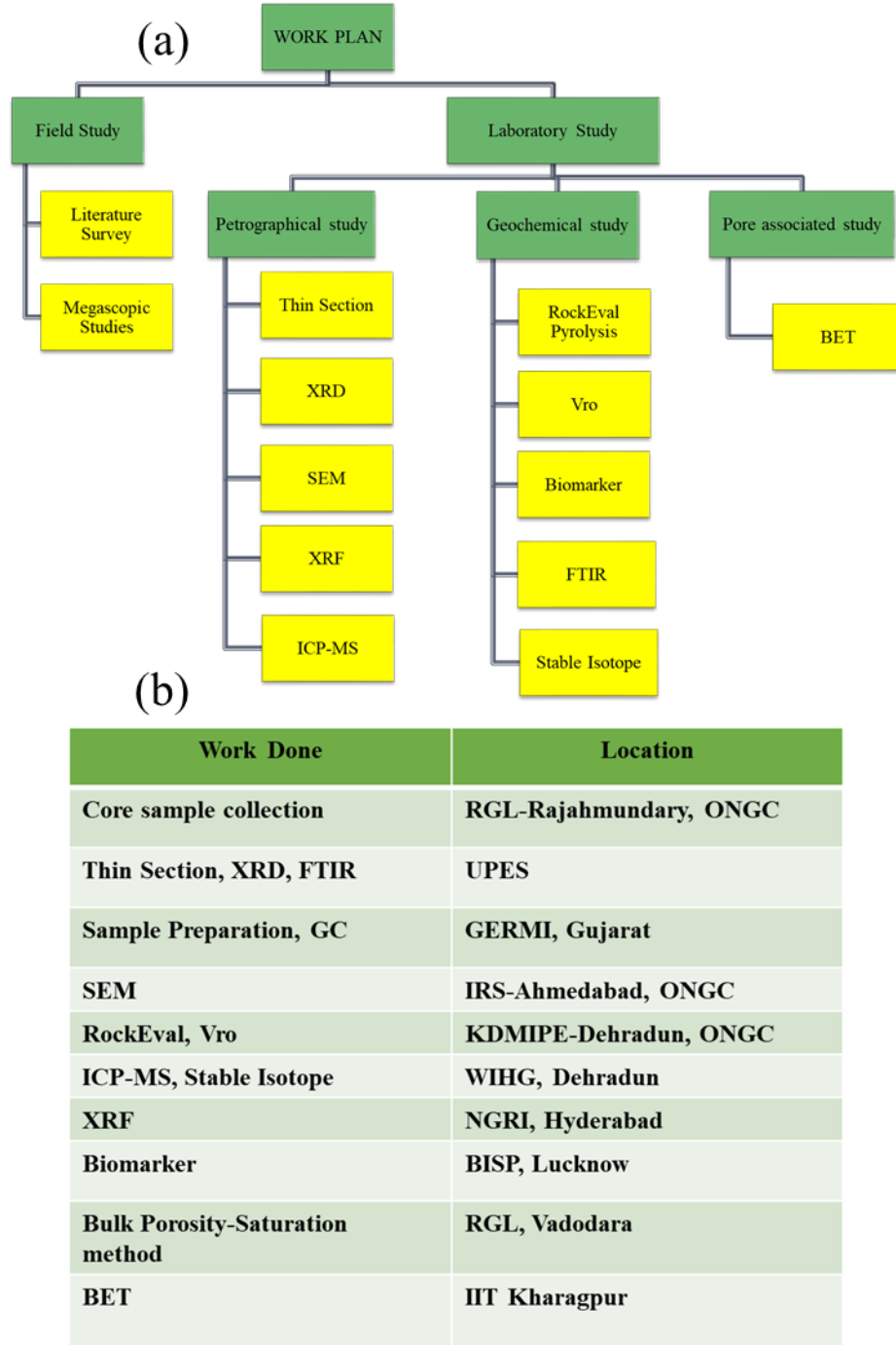


Fig. 1.2 (a) Work plan and (b) location of accomplishment.

1.6 Organization of the thesis: Chapter scheme

The thesis has been organized as follows:

Chapter 1: The chapter gives a brief overview of the shale gas scenario in India, fundamentals of shale reservoir and associated parameters, research gap, objectives, the scope of study and associated work plan.

Chapter 2: In this chapter extensive literature review on shale rock fundamentals is discussed with emphasis on shale as a nonconventional reservoir. Theories related to the pore characteristics, geochemical, geomechanical and petrographical properties of shale have been thoroughly described. A comprehensive shale gas scenario in India and comparison with prolific US shale plays have been described. Also, the geology of the study area with emphasis on lithology, depositional and tectonic setting is given in greater detail.

Chapter 3: The procedures of sample collection, sample preparation and analytical characterization techniques for different experiments are described in this chapter.

Chapter 4: Petrographical, mineralogical and elemental analysis based on thin-section XRD, FE-SEM, XRF and ICPMS are investigated in this chapter.

Chapter 5: In this chapter, geochemical analysis for estimating organic matter type and abundance, thermal maturity and hydrocarbon potential have been discussed.

Chapter 6: Pore-associated parameters based on FE-SEM and low-pressure N₂ isotherm studies have been described in this chapter.

Chapter 7: In this chapter, geochemical and petrographical findings are integrated and correlated with key geological factors.

Chapter 8: The findings based on petrographical, geochemical and pore-associated analysis are summarized. This chapter also includes a brief overview of future work.

CHAPTER 2: LITERATURE SURVEY

2.1 Introduction: Shale gas reservoir fundamentals

Shales are abundant, fine-grained, fissile, siliciclastic sedimentary rocks formed in low-energy environmental settings (Boggs, 2001). Shales constitute clay to silt-sized grained minerals and exhibit compositional heterogeneity where gas shales are silt-rich, carbonate-rich (transitioning into “tight gas sands”) or clay-rich (Josh et al., 2012).

Shales typically constitute clay minerals, quartz (detrital and authigenic), feldspar, carbonate minerals and iron oxides. The depositional environment plays a major role in the mineral genesis and thus, controls grain size and fabric. Quartz can manifest in detrital and authigenic forms where clay-sized microquartz cement may bind silt-size detrital quartz and increase brittleness (Milliken et al., 2012; Peng et al., 2020). Majorly clay minerals in shale are smectite, kaolinite, chlorite, illite, glauconite and montmorillonite. Clay genesis is dependent on the depositional environment, paleoclimate, provenance and diagenetic history. Kaolinite and smectite are generated during chemical weathering in humid and tropical climates and depend on provenance conditions (Weaver, 1989). In shallower depths, kaolinite (which is stable at low pH) and montmorillonite (which is stable at high pH) are more concentrated. Chlorite and illite are more prominent with higher depth ranges and may suggest higher sediment maturity. Clay minerals and their associated micropores can affect gas sorption by providing adsorption sites (order of sorption capacity: Smectite> Kaolinite>Chlorite>Illite) (Ji et al., 2012). Other minerals like feldspars, carbonates and Fe-rich minerals are important to be identified and quantified as they also affect the brittleness and storage capacity of shales. Mineralogy, grain size and fabric (structure and orientation) determine the bedding and lamination development (papery, flaggy, fissile and platy) in shales

(O'Brien, 1970). Fissility generally increases with higher clay, organic matter concentration, clay crystallinity and development of oriented mica laths (O'Brien, 1970).

Under favourable conditions shales constitute organic matter, which is a precursor to hydrocarbons, making shale-related exploration economically viable. The hydrocarbon formation is dependent on pressure and temperature conditions during deposition and post-depositional processes. Hydrocarbon potential depends on thermal maturity, organic matter type and abundance (Hunt, 1996). The nature of hydrocarbon generated depends on kerogen types (insoluble fraction of organic matter) (Tissot & Welte, 1984). The thermal maturity of organic matter is a function of depth geothermal gradient, rate of sedimentation and burial time, organic matter type and overburden pressure (Hunt, 1996). Slow sedimentation under an anoxic setting leads to high organic matter preservation with 1 to 2 percent Total Organic Carbon (TOC) being associated with a reducing to intermediate oxic environment. More than 2 percent TOC generally indicates a highly reducing environment with significant hydrocarbon production potential (Tissot & Welte, 1984).

The pores of shales lie in the nanometer range and tend to be relatively more complex than the conventional reservoirs due to the compositional heterogeneity. The permeability of shale reservoirs is very low (ranges in nanodarcy) generally due to poor pore connectivity (Sondergeld, Ambrose, et al., 2010). The pore size distribution and porosity are important pore-associated attributes. Total water-accessible porosity is equivalent to the total porosity, whereas effective porosity is equivalent to the total porosity sans clay-bound water (Kuila & Prasad, 2013). The pore-size distribution (PSD) assesses varying pore sizes and their relative volumes. According to the International Union of Pure and Applied Chemistry (IUPAC), pores are segmented as micropores (pores smaller than 2 nm), mesopores (pores between 2 nm and 50 nm) and macropores (pores larger than 50 nm) (Sing, 1985). This categorization is generally based on the kinetics of carbon dioxide and nitrogen adsorption at -197.3°C (77.3K) and 1 atmospheric pressure in porous materials with varying pore diameters (Kuila & Prasad, 2013). The downside of

these techniques is that pores bigger than 50 nm are not further subdivided and are termed macropores (Kuila & Prasad, 2013). The fractal dimension (D) is used to quantify pore surface roughness and associated structural irregularity to define the pore geometry (Schlueter et al., 1997; Shao et al., 2017). It is a roughness index that ranges from 2 to 3, with 2 denoting a smooth surface and 3 denoting a rough surface.

Adsorption is the mechanism by which fluids concentrate on a solid surface by either pore volume filling or monolayer formation (Ross & Bustin, 2009b). Physical adsorption is reversible and occurs owing to the weak Van der Waal's forces of attraction between the adsorbent (pore surface) and the adsorbate (fluid) (Brunauer et al., 1938). During this process, depending on the adsorbate-adsorbent type, a monolayer or multilayer forms at lower pressures and higher pressures respectively. Chemical adsorption unlike physisorption is an irreversible process characterized by significant electron transfer bonding between solid and gas molecules (Webb, 2003). Gas shales tend to be microporous adsorbents where the adsorption of methane occurs onto the organic matter and/or clay mineral surfaces. During drilling, fractures are generated and gas molecules flow toward the low-pressure zones. Due to differential pressure, compressed gas is released and then the adsorbed gas also starts desorbing (Javadpour, 2009). Thus, quantifying the adsorption capacity of shale and its primary controls is essential. Due to catalytic cracking potential clay minerals can influence kerogen to form lighter hydrocarbons (Tannenbaum et al., 1986). Hence organic matter and clay minerals can affect the total storage capacity. Therefore it is essential to understand the mineralogical setup and its control on pore attributes. Adsorption isotherm studies are critical for estimating total adsorbed gas capacity and predicting gas storage capacity in shale. The isotherm illustrates the nature of the process occurring on the adsorbent's surface, exhibiting its porosity, pore morphology and surface area. There are six types of adsorption isotherms as per the IUPAC, indicating adsorbate nature as well as pore shapes (Sing, 1985).

The overall understanding of the gas storage mechanism and evaluation of transport efficiency is dependent on comprehensive pore attribute studies in gas shales (Labani et al., 2013; Ross & Bustin, 2009b). Petrophysical parameters such as porosity and permeability are a further function of shale composition (Ross & Bustin, 2009b; Sondergeld, Newsham, et al., 2010). The evaluation of pore attributes is exceptionally challenging as most shale formations have a unique depositional environment and also exhibit compositional heterogeneity. The micropores and finer mesopores in shale are generally associated with organic matter and clay minerals fraction, whereas the macropores are generated by the mineral grain arrangement (M. E. Curtis, 2010; M. E. Curtis et al., 2013; Loucks et al., 2012). Multiple studies have indicated methane sorption generally tends to increase with TOC and micropore volume (Cui et al., 2009; Ross & Bustin, 2007). Further, kerogen type (Type III>Type II>Type I) also influence the methane sorption capacity in shales (Bakshi et al., 2018; T. Zhang et al., 2012). Type III kerogen tends to have higher methane sorption capacity due to its microporous nature and higher concentration of aromatics (T. Zhang et al., 2012). Thermal maturity is also known to affect the organopores due to pore restructuring on the higher thermal regime (Behar et al., 1992; Behar & Vandenbroucke, 1987). Although shale reservoirs generally exhibit lower porosity and permeability than conventional reservoirs, they may have storage in matrix and transport via fractures, making them a feasible candidate for CO₂ sequestration (H. Wang et al., 2012). Also, the methane generation process, storage and transport in shales are comparable to that of coal (Lutynski & González, 2016). Thus, it is essential to understand controlling factors on pore mechanisms for both gas shale production and CO₂ sequestration.

2.2 Critical appraisal of the state of the art

Shale characterization as an unconventional resource requires comprehensive analysis of (1) Organic geochemical assessment (organic matter type, abundance and associated thermal maturity), (2) Petrophysical assessments (porosity–

permeability and pore size distribution) and (3) Geomechanical and mineralogical assessment (mineralogy and rock fabric and its relationship with brittleness) (Josh et al., 2012).

Organic matter characterization based on organic petrography, RockEval, GC-MS and GC-IRMS is extensively pursued with steady enhancement in critical hydrocarbon prospectivity assessments. The reproducibility standard deviation (RSD) of TOC measurements using the conventional RockEval and the Enhanced Slow Heating (ESH) cycle was less than 1% (Sanei et al., 2015). The ESH cycle detects hydrocarbon for longer period and can be useful for unconventional resource estimation by providing sufficient time to evolve volatile free hydrocarbons (Sanei et al., 2015; X. Zheng et al., 2021). The ESH cycle allows for the volatilization of free hydrocarbons by lowering the minimum starting isotherm in samples to 150 °C for 10 minutes (X. Zheng et al., 2021). Gradually this temperature was ramped to 650 °C slowly at 10 °C per minute. Consequently, the traditional S_1 and S_2 peaks were quantitatively split into free light oil (S_{1ESH}), fluid-like hydrocarbon residue (FHR; S_{2aESH}) and solid bitumen (S_{2bESH} + residual carbon) (Sanei et al., 2015). The FHR may influence wettability by forming hydrophobic matrix pore networks in reservoir zones that are not filled with solid bitumen (Sanei et al., 2015; X. Zheng et al., 2021). The categorization of kerogen type and parameters like thermal maturity help understand hydrocarbon potential and its influence on porosity (Kala, Turlapati, et al., 2021). Organic matter and associated clay have positive control on micropore volume (Kala, Turlapati, et al., 2021; Turlapati et al., 2020). Thus, enhanced parametric organic geochemical analysis helps give a better outlook on nonconventional resources.

Shale pore network and fracture assessment are critical for drilling operations (Kala, Turlapati, et al., 2021). Depositional and burial process (diagenesis) and tectonic history depth can influence and alter primary porosity (Kala, Turlapati, et al., 2021; Temizel et al., 2020). Shales generally constitute micropores and have low permeability (nanodarcy) with a gas storage mechanism dependent on primarily gas adsorption, dissolved gas in kerogen and free gas in matrix and

fractures (Temizel et al., 2020). Shale reservoirs constitute nanoscale pores dominantly in organic matter (10nm-500nm) and inorganic matter (10nm-100nm) (Loucks et al., 2012). Hydrocarbon adsorption is higher in organic pores and is also facilitated by clays due to their virtue of catalytic cracking potential (Tannenbaum et al., 1986).

Presently variable 2D (SEM, TEM) and 3D (X-Ray CT, FIB-SEM) imaging techniques are available for mineralogical and morphological feature assessments (Chandra et al., 2022; Chandra & Vishal, 2021; Josh et al., 2012; Vishal et al., 2019). 3D imaging techniques are better for visualizing fractures and flow dynamics in shale (Chandra & Vishal, 2021). 2D imaging techniques are better for higher resolution micropore identification and enhanced pore morphology detection (Chandra & Vishal, 2021). Post imaging processing and Machine Learning are being utilized for high image resolution, time-efficient and fast interpretation of a huge volume of data (Bihani et al., 2022; Chandra & Vishal, 2021; Davletshin et al., 2020).

Mercury Injection Capillary Pressure (MICP), Low-Pressure Gas Adsorption (LPGA), Small-Angle X-Ray Scattering (SAXS) and Nuclear Magnetic Resonance (NMR) further validate pore attributes (Chandra & Vishal, 2021; Temizel et al., 2020). MICP by immersion method at 60000 psi provides total porous volume in a dry sample (Temizel et al., 2020). LPGA using N₂ and Ar gases is utilized for probing mesopores and CO₂ for micropore determination (Turlapati et al., 2020). Further LPGA provides attributes like surface area, pore size distribution, pore volume and fractal assessments (Kala, Turlapati, et al., 2021). SEM coupled SAXS helps in resolving and comparing accessible and inaccessible pore parameters in heterogeneous shales (Chandra & Vishal, 2021). NMR results are being considered to quantify shale saturation and porosity determination at different saturation levels and temperatures (Temizel et al., 2020).

The geomechanical and mineralogical assessment further facilitates the understanding of shale brittleness. Shales with higher concentrations of brittle minerals (silicates like quartz, feldspars and carbonates) exhibit high young's

modulus and low Poisson's ratio (W. Ding et al., 2012). Such shales tend to have the formation of natural and induced fractures on the application of external forces and are thus efficient hydrofracking candidates (Josh et al., 2012). Further mineral form and texture also govern shale brittleness which is dependent on provenance and depositional environment (Kala, Devaraju, De, et al., 2021; Milliken et al., 2012; Peng et al., 2020). Sonic logs, seismic data, triaxial compression test, atomic force microscopy and nano-indentation tests have been used for Young's modulus estimation from macro to nanoscale in shales (Temizel et al., 2020). Depending on mineralogy, fabric and fracture network it was observed that shale with lamellar structures has higher Young's modulus and is thus more fracable provided there is a lower degree of microfracture presence (Temizel et al., 2020). Thus, shales with a higher concentration of authigenic quartz with microfractures and high Young's modulus (15-25 GPa) are good fracking candidates (Temizel et al., 2020). Systematic and comprehensive assessment of shale play can help in "sweet spot" identification. Thus, methodical investigation of regional geology, geochemical, petrophysical evaluations and geomechanical aspects are of utmost significance in gas shale assessments.

2.3 Shale gas scenario in India

Exploratory work is been carried out in variable Category-I and Category-II basins like KG, Cambay, Assam, Damodar, Cauvery and Vindhyan (Dayal et al., 2014; Khan et al., 2000; Kumar et al., 2017; Loucks et al., 2009; Tripathy et al., 2019). The Cambay Basin constitutes five tectonic blocks with petroleum plays of Paleocene to Miocene age (DGH, 2012). The basin has a prospective areal extent of 940 mi² with risked recoverable resource of 20 Tcf (EIA, 2011). The organic-rich zone of 1500 feet thickness in the depth interval of 11500-16400 feet in Cambay shale was assessed by EIA, 2011. Hydrofracking was carried out in the Tarapur block (two wells in Dholka Field) and led to modest gas shale production from shallow Miocene sediments (Sharma & Kulkarni, 2010). Padhy et al., 2016 reported a comprehensive geochemical and petrophysical study of Cambay shale from a well of the Broach-Jambusar block. Kumar et al., 2017 and Padhy et al.,

2016 reported the presence of Type III kerogen in admixture with Type II with an average TOC of 2%. Elemental and mineralogical evidence indicated Cambay shale formation in the marginal marine environment with the prevalence of anoxia. Kumar et al., 2017 have characterized Cambay shale formation comprehensively based on organic geochemical, morphological and mineralogy. The Cambay shale has silica-rich argillaceous mudstone to argillaceous siliceous mudstones with low to medium mineralogical brittleness (Kumar et al., 2018). Hydrofracking in the well of interest (3200m depth) led to oil production from Paleocene-Eocene sediments. Kumar & Ojha, 2021 have integrated organic geochemical and geothermal studies using PetroMod®, BPSM software by Schlumberger. Their assessment revealed that the study area constitutes shale mainly in the early to main oil generation window with shale oil prospects in deep sections of the south Cambay Basin.

Upper Assam Basin has reported oil and gas from shale and coal of Barail Group of Upper Eocene-Oligocene age (DGH, 2012). TOC content ranges 1-10% and oil window was reported in shallower parts with the onset of gas generation in the south to southwest deeper parts (Sain et al., 2014). As per, Biswas et al., 2020 Oligocene shales from Makum Coal Basin were deposited in fluvio-deltaic to the lagoonal environment under dysoxic to anoxic conditions. Bakshi et al., 2020 reported organic (high vitrinite; Type II-III kerogen) and clay-rich shales with the presence of micropores and mesopores. Bakshi et al., 2017 inferred that shale porosity was strongly affected by organic matter type and clay has a positive influence on shale porosity.

Damodar valley Basin has been studied comprehensively with organic-rich sequences of Barren Measure and Barakar Formation. The basin has a prospective areal extent of 1080 mi² with risked recoverable resource of 7 Tcf (EIA, 2011). Organic rich zone of 1050 feet thickness in the depth interval of 3280-6560 feet in Barren Measure shale was assessed by EIA, 2011. Barren Measure constitutes Type III, gas prone with TOC and VRo ranging 4.2-6.6% and 1.0-1.3% respectively. TOC (4.4-8.3%) is higher in the Barakar Formation and a site of greater interest (Sain et al., 2014).

Cauvery is a petroliferous pericratonic basin with formations ranging from Jurassic to Pliocene. The basin has a prospective areal extent of 1005 mi² with risked recoverable resource of 9 Tcf (EIA, 2011). The organic-rich zone of 800 feet thickness in the depth interval of 7000-13000 feet in the Andimadam Formation was assessed by EIA, 2011. As per DGH, 2012, the main source rock with Type II and III kerogen from Andimadam Formation and Sattapadi shale have TOC of 1-3%. The source rock has reported thermogenic natural gas with vitrinite reflectance ranging 0.69-1.13 % (DGH, 2012; Sain et al., 2014). Damodar valley comprises sub-basins from east to west being- Raniganj, Jharia Bokaro, Ramgarh, Karanpura, Auranga, Daltonganj and Hutar. The sub-basins have similar tectonic and geological history but vary in terms of thickness and depth of Barren Measure Formation.

Vindhyan basin in central India is an intracontinental, Proterozoic-aged basin (DGH, 2012). Singh & Chakraborty, 2021 evaluated the organic geochemistry of variable shaly sequences (Arangi, Bijaygarh, Koldaha, Rewa, Rampur and Sirbu) present within the Vindhyan Supergroup. Bijaygarh and Arangi shale assessment revealed the presence of Type-III kerogen and gas prone hydrocarbon source. Hinota and Pulkova shales of the Vindhyan Basin with high TOC up to 3.8% are prospective exploration sites. Type I and II kerogens are reported and deposited in the marine environment (DGH, 2012; Sain et al., 2014).

Comparing India's prospective shales with the US producing shale plays suggest geological, petrophysical and geochemical based differences. Indian shales have higher clay content, lower brittleness, Type III kerogen of the relatively lower thermal regime, less oil saturation (<2%) and low matrix permeability (A. Singh et al., 2018). Indian prospective shales are generally deeper formations of Permian and Tertiary-Cretaceous ages deposited in the fluvio-marine transitional environment (Sinha et al., 2010). The US producing shales plays (Devonian aged) are shallower with Type II/III kerogen and higher brittleness (A. Singh et al., 2018; Sinha et al., 2010) The Indian shales exhibit distinct variation from producing

prolific shales of US and thus require detailed geological, petrophysical and geomechanical investigations.

2.4 Geology of the study area

The KG Basin along the eastern margin of India resulted from rifting of the Gondwanaland during the late Jurassic period (Sastri et al., 1981). Of the four major linear belts of peninsular India along which the Gondwana basins got evolved, the KG Basin forms the coastal tract of the NNW-SSE trending Wardha-Pranhita-Godavari Valley belt (Fig. 2.1; Mukhopadhyay et al., 2010). Overlying the southern extension of the Pranhita-Godavari (PG) paleo-rift, the Gondwana sediments in KG exist beyond the established limits of the PG graben and spread across the entire basin (Shandilya, 2017). Stratigraphically, the Gondwana Supergroup is divided into Permian Lower Gondwana Group of about 2300 m thickness with Gangomopteris-Glossopteris flora and Mesozoic Upper Gondwana Group with a thickness of about 3000 m, characterized by Dicroidium–Lepidopteris-Ptylophylum flora (Mani et al., 2016; Mukhopadhyay et al., 2010). Sediment deposition in the Gondwana basins of India evolved through a complex interplay of faulting and changes in sea level and climate, due to which the depositional patterns in individual Gondwana basins exhibit wide variations (Mukhopadhyay et al., 2010). KG manifests a typical tectonic-sedimentary assemblage of more than 5 km thickness, ranging from Permian to Recent age (Rao, 2001). These petroleum systems range from the oldest Permo-Triassic K-M-R system (onland) to the youngest Pleistocene channel levee complexes in deep water (offshore) (DGH, 2012). The well-developed and preserved Lower Gondwana sediments form part of an important Permo–Triassic Kommugudem–Mandapeta–Red Bed (K-M-R) petroleum system of the basin (Gupta, 2006; Mani et al., 2016).

This study focuses on the Early Permian Kommugudem Formation characterized by alterations of sandstone–shale–coal sequences. Being organically rich and thermally mature, it forms the main source rock for the Permo-Triassic petroleum system of KG. Palynological studies suggest the Early Permian (Artinskian) age for

the Kommugudem Formation (Prasad et al., 2000). It is considered to be the stratigraphic equivalent of the well-studied, coal-bearing Barakar Formation of the Indian Gondwanas (Casshyap et al., 1988). The widely separated Gondwana basins of peninsular India exhibit gross similarity in the litho-fill composition variations. The deglacial sequences of Barakar represent a warm humid climate, in contrast to the arid and cold exhibited by glacial deposits of the Talchir that underlie it. A predominant fluvial depositional system has been reported for Barakar, however, the depositional characteristics of the Upper Barakar Formation indicate a source different from the sediments of Lower Barakar and possible marine influences and/or incursions have also been reported (Bhattacharjee et al., 2018).

2.5 Geological settings and stratigraphy

The evolution of the KG Basin was initiated with the drifting and consequent break-up of Gondwanaland. It got evolved in the ‘rift phase’ which was active during the Jurassic-Lower Cretaceous and the ‘drift phase’, which continued from Upper Cretaceous to Holocene (Gupta, 2006; Mani et al., 2016). In the first phase of intracratonic rifting in the Gondwanaland, the NW-SE trending Pranhita-Godavari (PG) basin originated (Mani et al., 2016). It hosts the complete sequence of Gondwanan Supergroup ranging in age from Permian to Lower Cretaceous. The continental stretching of the rift-fill sediments of PG graben along the NE-SW strike of primeval structural grain leads to the development of the NE-SW pericratonic, passive margin KG Basin.

KG Basin is a deltaic plain formed by rivers Krishna and Godavari with an aerial extent of 28000 sq. km onland and 24000 sq. km (up to 200m isobath) offshore in the Bay of Bengal (Shandilya, 2017). KG Basin is characterized by its echelon horst and graben system. It is divided into three sub-basins, Krishna, West Godavari and East Godavari, which are separated by the Bapatla and Tanuku horsts, respectively (Mani et al., 2016). The West Godavari is further sub-divided into two grabens, Gudivada and Bantumilli, which are separated by the Kaza–Kaikaluru horst (Mani et al., 2016; Rao, 2001). On either side of the Tanuku horst, lie the Kommugudem

and Mandapeta troughs. Initial phases of rifting led to the deposition of more than 3 km thick Permo-Carboniferous sedimentary column, known as Pre-rift sediments (Shandilya, 2017). The second phase of NE-SW pericratonic rifting led to the fragmentation of Gondwanaland during the Late Jurassic- Early Cretaceous. It led to the deposition of nearly 3 km of syn-rift and post-rift sediments (Shandilya, 2017). Gondwana sediments of the KG Basin have been categorised as the coastal and continental Gondwana, based on the palynoflora and litho-assemblage (Lakshminarayana, 2002; Mani et al., 2016).

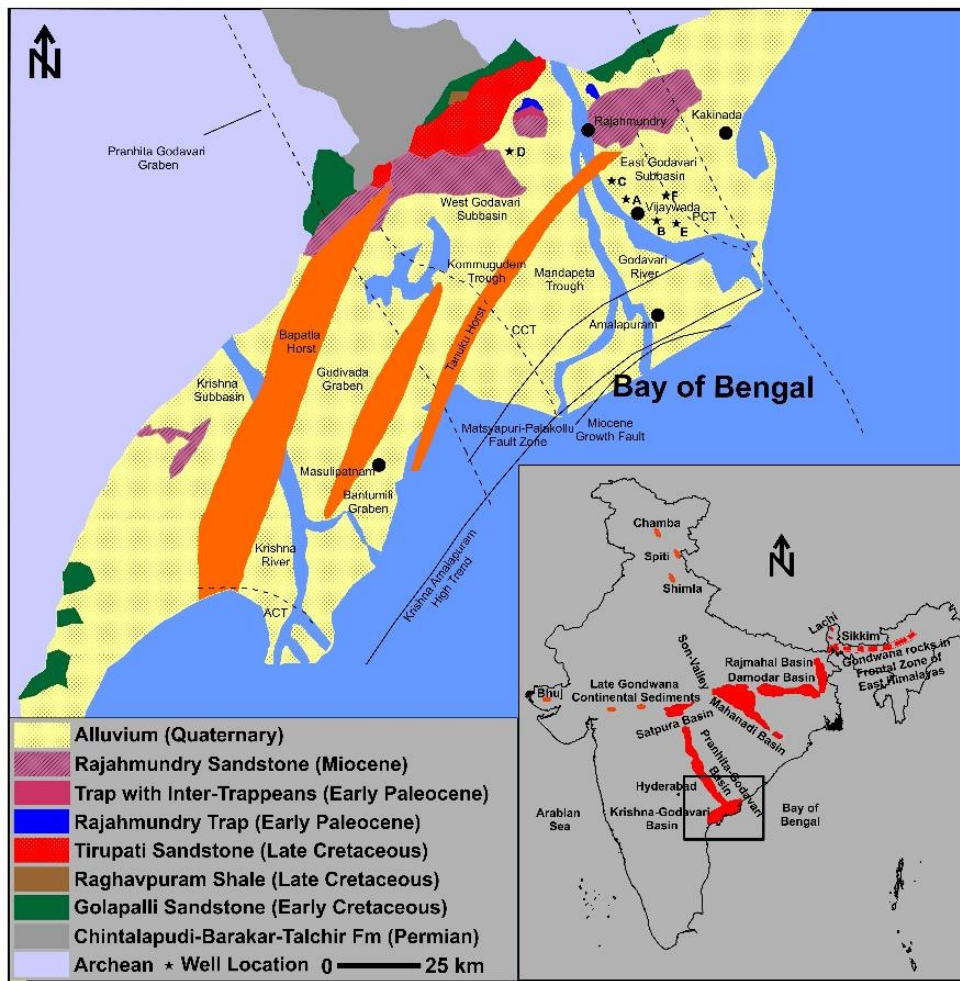


Fig. 2.1 Geological map of the KG Basin in the backdrop of Gondwana basins of peninsular India (modified after Gupta, 2006).

Generalized lithostratigraphy of the Kommu-gudem Formation, KG Basin is presented in Fig. 2.2. The Archean basement of gneisses and granites underlies the

Permo-Triassic section of the KG Basin (Rao, 2001). Kommugudem Formation of the alternate sand-shale-coal sequence is overlain unconformably by Late Permian, Lower Gondwana Mandapeta sandstone with minor shales deposited under a fluvial channel environment. Red Beds of the Late Triassic to Early Jurassic age lie unconformably over Mandapeta Formation. It consists of ferruginous sandstone, alternating with claystone deposited in the fluvial environment (Rao, 2001). The intracratonic tectonic-sedimentation cycle of the Permian Kommugudem Formation and the dominant Triassic sandstone of Mandapeta Formation constitutes a southern extension of Gondwanan sedimentation of Pranhita-Godavari in the KG basin. Kommugudem has been encountered in the wells near Kakinada, Mandapeta and Endamuru area, as well as in the Bhimadolu graben of the KG Basin. In general, the formation exhibits a depth interval of 2800m to 4300m with a maximum thickness of 950m with hydrocarbon potential assessed to be 330 million tons (DGH, 2012; Jain et al., 2004; Rao, 2001). The type well Kommugudem-1 exhibits a coal-shale unit of more than 900 m thickness (Jain et al., 2004). Kommugudem Formation is overlain by Mandapeta sandstone acting as a reservoir for the K-M-R-system while, Red Bed and tight layers within Mandapeta sandstone act as an effective seal (DGH, 2012; Gupta, 2006; Rao, 2001).

AGE	FORMATION	LITHOLOGY	THICKNESS (m)	LITHOLOGICAL DESCRIPTION	
LOWER GONDWANA	TRIASSIC	RED BED	20-110	Reddish brown claystone	
		MANDAPETA FORMATION	UNIT V	45-120	Sand-shale intercalation
			UNIT IV	30-175	Shale with thin sand intercalation
			UNIT III	65-370	Sand-shale intercalation
			UNIT II	110-195	Shale with thin sand intercalation
			UNIT I	70-325	Sandstone with thin shale intercalation
	PERMIAN	KOMMUGUDEM FORMATION	950	Shale-sand-coal intercalation	
		DRAKSHARAMA SHALE	240	Greenish black shale	
	ARCHEAN BASEMENT			Garnet Gneiss	

Fig. 2.2 Generalized litho-stratigraphy of Kommugudem Formation.

CHAPTER 3: MATERIALS AND METHODS

3.1 Chapter overview

A multiproxy approach based on petrophysical and geochemical signatures was adopted for meaningful characterization of Permian shales of the KG Basin. The procedures of sample collection, sample preparation and analytical characterization techniques for different experiments are described in this chapter. Table 3.1 summarizes experimental procedures and associated results attained.

3.2 Study area and core samples

Conventional cores of six boreholes (Fig. 3.1), ranging in depth from 2700 to 4300 m, from Oil and Natural Gas Corporation (ONGC) Limited, Rajahmundry were considered for the present study (Fig. 3.1). In a wider perspective, Wells A, B, C, D, E and F are located in the Mandapeta graben of the East Godavari sub-basin (Fig. 2.1). Mandapeta structure was formed during the Early Palaeozoic rift phase. The sedimentary fill in the East Godavari sub-basin ranges from 2900 meters above the pre-existing bedrock horsts to more than 5000 meters in the southeast deep basin region. Exploratory drilling has indicated the presence of Paleozoic sediments comprising the shale-coal-sandstone sequence of the Gondwana age, envisaging the subsurface extension of Pranhita-Godavari graben into this area (Jain et al., 2004). The East Godavari basin's Kommugudem and Mandapeta troughs are located on each side of the Tanuku horst (Fig. 2.1). Gondwana sediments have been encountered at depth in both Kommugudem and Draksharama structures (Jain et al., 2004). Fifty-three litho-units of the Kommugudem Formation, comprising primarily of carbonaceous shales and a few sandy, silty and coaly shales were identified for detailed investigations. Air-dried samples were manually screened for visible contaminants and cleaned with hot distilled water to eliminate residues of

drilling fluid additives. The cuttings and powdered fractions of samples were prepared and preserved in airtight bags.

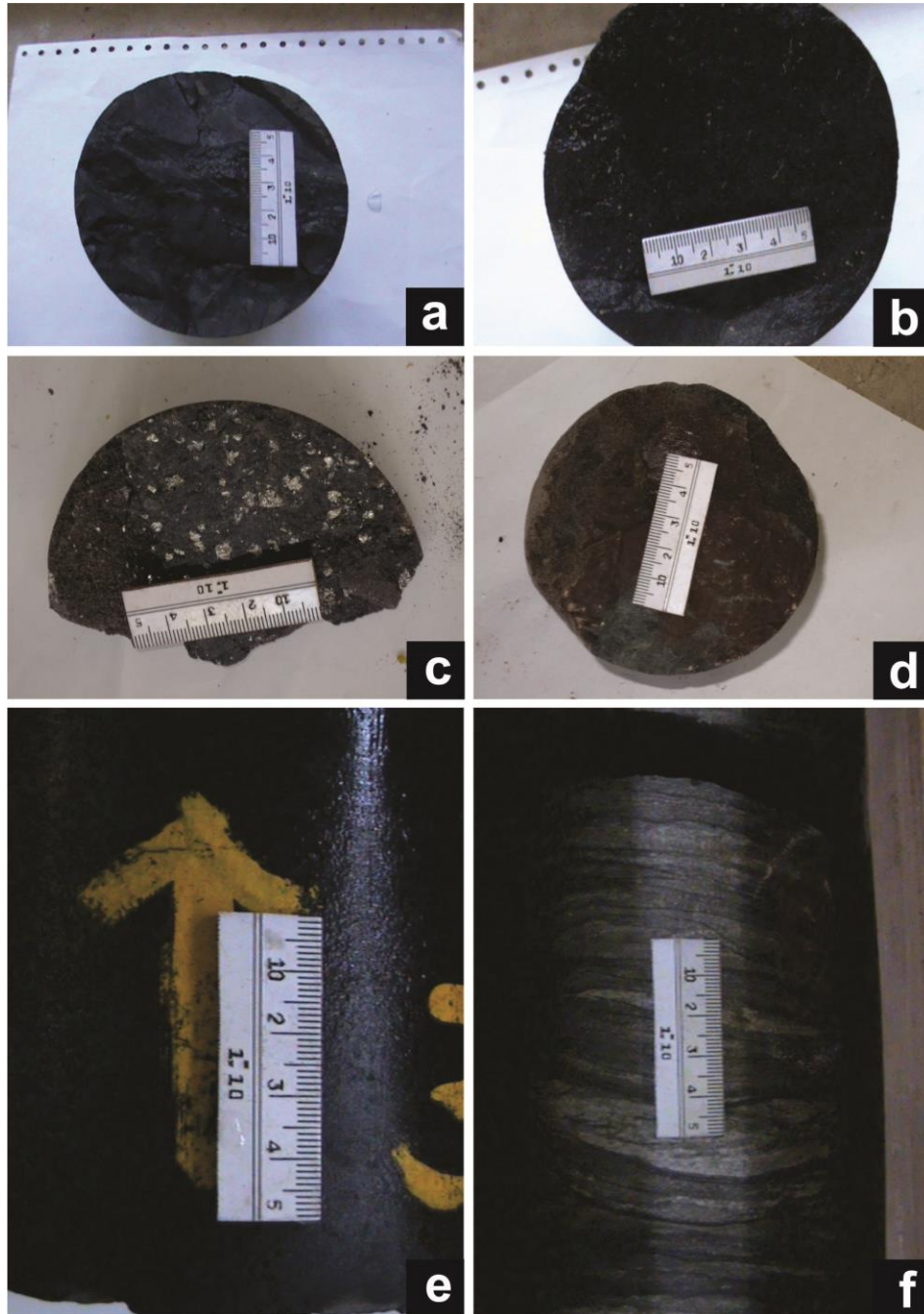


Fig. 3.1 Photomicrographs indicating core samples in cross-section: a) Carbonaceous shale; b) & c) Mica-rich carbonaceous shale; d) Fe-rich shale; Longitudinal view of e) Carbonaceous shale, f) Sandy-shaly intercalation.

3.3 Megascopic study

A general study on surface exposures and subsurface core samples was done to categorize the major features such as lithology, colour, bedding thickness, nature of bed contacts, sedimentary structures, texture, fossils, porosity and fracture.

3.4 Thin section analysis

Standard petrographic techniques were employed to study the thin sections of 53 samples using Olympus polarizing Microscope BX5. The samples were air-dried followed by epoxy vacuum impregnation and later polished using progressively finer alumina suspension (11 m, 0.31 m and 0.051 m) with a maximum section thickness of 20-30 microns. The mineral assemblage and texture were observed in plane-polarized and cross-polarized light

3.5 X-Ray Diffraction (XRD) analysis

The semiquantitative mineralogical investigation of 53 selected samples was carried out by Bruker D8 Advance Eco X-Ray Diffractometer. Petrographically by thin section analysis clay identification is difficult in shales. Thus, the non-destructive XRD technique for the detection and quantification of minerals is significant in shale-associated studies. The powdered samples of 60 mesh sizes were scanned from 5° to 60° 2 θ with Cu K α radiation (Ni-filtered). The mineral phase identification was carried out by comparing data with ICDD cards.

3.6 Field Emission Scanning Electron Microscope (FE-SEM) analysis

The mineralogical and morphological studies were analyzed by photomicrographs of the 53 samples using JEOL JSM-7610F FE-SEM. The selected shale samples were attached to an aluminium stub using double-side metallic tape and coated with gold. Secondary electron (SE) and back scattered electron (BSE) images were generated for the samples by operating FE-SEM at 30 KV and beam currents ranging from 0.3 to 5 nA.

3.7 X-Ray Fluorescence (XRF) analysis

The Axios mAX, PANalytical sequential wavelength dispersive X-Ray fluorescence spectrometer assessed major oxides for twenty samples. Dried sample powder was ignited in an alumina crucible at 950°C for about one hour and the percentage of weight loss (LOI) ranging 5.13-16.35% was obtained. Approximately 2 gm powdered sample and Boric acid were inserted in collapsible aluminium cups and hydraulically pressed to create a 40 mm diameter pellet. SARM-41 was used as reference material for the calibration.

3.8 Inductively Coupled Plasma Mass Spectrometry (ICP-MS) analysis

Trace and rare earth elements in the selected ten shale samples were analyzed using ICP-MS, SCIEX ELAN DRC-E, PerkinElmer. 0.1 gm of powdered sample was treated with concentrated nitric (HNO₃) and hydrofluoric (HF) acids in the ratio of 1:2 at 160°C for a few hours in Teflon crucibles. The sample solution was then treated with 5 ml of perchloric acid (HClO₄). The completely digested samples were collected with 20% HNO₃ and then diluted to 100 ml using ultra-pure water. SCO-1 (shale) was used as reference material for the calibration.

3.9 RockEval Pyrolysis

The 53 selected shale samples were homogenized to 60 mesh sizes before the analysis in the RockEval-VI instrument (Turbo Version, Vinci technologies). 50 mg of powdered samples were examined in analysis mode using the basic/bulk rock method. Pyrolysis was conducted in a nitrogen-inert environment at a flow rate of 100 ml/min (Behar et al., 2001). In the pyrolysis oven, the samples were subjected to an initial isothermal temperature of 300 °C (maintained for 3 minutes) and then the temperature was elevated to 650 °C at a rate of 25 °C/min. Further, selected samples were oxidized to 850 °C under high air purity. The programmed pyrolysis and oxidation ovens of the pyrolyzer provide bulk organic matter parameters to infer the richness, kerogen type, thermal maturity and hydrocarbon potential in the rock samples (Espitalié, 1986; Peters, 1986; Tissot & Welte, 1984).

3.10 Vitrinite reflectance analysis

The Fluorescence Microscope with Image Analysis System (Automated Microscope Leica Model DM6000M with MSP 200 Photometer, DFC 500 Digital Camera) was used for the maceral identification and vitrinite reflectance analysis of selected 9 samples. The sample pellets were made in the plastic moulds with cold setting epoxy resin and the surface of the mounted sample was ground on grade 100 and grade 320 waterproof silicon carbide paper, using water as a lubricant. The samples were then polished first on a billiards cloth and then on a Selvyt cloth-covered rotary lap using 1.0, 0.3 and 0.05 μ (micron) alumina powder successively. The system was calibrated with a glass standard of known reflectance in an oil medium for vitrinite reflectance measurements. The reflectance of vitrinite macerals was assessed with a 50X objective immersed in oil. More than twenty readings were considered for vitrinite reflectance for each sample.

3.11 Biomarker extraction and analysis

Sedimentary organic matter was extracted from fifteen shale samples selected based on the TOC content. Dichloromethane: methanol (DCM: MeOH) mixture (9:1) was used to agitate the oven-dried powdered samples by ultrasonication for 30 minutes. Asphaltene and sulfur were removed using excess hexane and activated copper turnings, respectively. Filtered samples were dried at room temperature in an inert atmosphere of nitrogen. Silica gel chromatography separation was carried out using *n*-hexane and DCM: hexane mixture (1:4) for the separation of saturate and aromatic compounds, respectively. The solvents were evaporated to about 1 ml under a gentle stream of N₂. Agilent 7890A Gas Chromatograph (GC) interfaced to Agilent 5975C Mass Spectrometer (MS) was used to analyze the biomarker extracts. The GC was equipped with an HP-5MS fused silica capillary column (30 m \times 0.25 mm i.d., 0.25 μ m film thickness) and Helium (He) as the carrier gas at a flow rate of 1 ml/min. The GC oven temperature was maintained at 40 $^{\circ}$ C for 5 minutes before ramping to 310 $^{\circ}$ C at 4 $^{\circ}$ C/min for 5.5 minutes. The mass spectrometer was set in EI mode at 70 eV in full scan mode, with a mass range

(m/z) of 50-600 amu. To detect saturates and aromatic presence in the samples, data were processed using Chemstation software. Peak assignments were made using GC retention time and mass spectral data, compared to the MS library and published mass spectra.

3.12 Kerogen isolation and bulk carbon isotope ($\delta^{13}\text{C}_{\text{org}}$) analysis

Kerogen was isolated from the selected fifteen shale rocks by treating ~1 gm of the powdered sample with 20% HCl while stirring at 50°C for 6 hours. Further, it was soaked in 20% HCl and 48% HF (1:4) acid mixture overnight. The acid-treated samples were thoroughly washed with MilliQ water and then dried at 50°C. ~0.5 to 2 mg decarbonated sample was loaded in a tin capsule and introduced into the pre-filled and conditioned reactor of Elemental Analyzer (Flash EA 2000) through an autosampler. The sample was flash combusted at ~1020°C in an oxygenated environment to convert the sample carbon into carbon dioxide. The sample CO₂ gas after purification was introduced into the Delta-V plus Continuous Flow Isotope Ratio Mass Spectrometer (CFIRMS) coupled with the ConFlow IV interface. Corresponding signals of 44, 45 and 46 masses were detected for reference gas and samples to calculate isotopic composition. Through the reference open split, three pulses of reference CO₂ were let into CFIRMS, followed by a single pulse of sample CO₂. The bulk carbon isotope values calculated corroborate with paleoclimate and paleoproductivity assessment.

3.13 Fourier-transform infrared spectroscopy (FTIR) analysis

The FTIR spectroscopy was assessed in absorbance mode from 4400 cm⁻¹ to 400 cm⁻¹ wavelengths for selected 10 shale samples utilizing Perkin Elmer Frontier FT-IR for analysis. The crushed shale samples (1 mg; 75 mm size) were pressed into pellets in an evacuated die post combining with 100 mg KBr. FTIR spectroscopy provides details on inorganic and organic functional groups in the selected shale samples.

3.14 Low-pressure N₂ adsorption analysis (LPNA)

LPNA study investigation for pore characteristics of 5 samples was performed at 77 K with the relative pressure range (P/P_o) of 0 – 0.99 using Micrometrics ASAP 2020. Before the experiment, to eliminate volatiles and moisture from pores, samples (crushed and powdered <250 mm) were pre-treated for 12 hours at 120°C (in vacuum). The LPNA analysis determines pore volume, specific surface area and pore size distribution in the selected samples. The plotted sorbed gas volume versus pressure depicts adsorption isotherm. The adsorption isotherm shape represents pore types and the adsorption process for the adsorbent.

The surface area calculation (BET model) is centred on multilayer adsorption theory where monolayer adsorption in pore walls is postulated to be in 0.05 to 0.35 relative pressure range (Equation 3.1; Brunauer et al., 1938):

$$\frac{1}{V \left(\left(\frac{P_o}{P} \right) - 1 \right)} = \frac{1}{V_m C} + \frac{C - 1}{V_m C} \left(\frac{P}{P_o} \right) \quad (3.1)$$

Where V is adsorbed gas volume at relative pressure P/P_o , V_m is the volume adsorbed in the monolayer and C is a BET constant (Brunauer et al., 1938).

An inflection occurs in the isotherm with increasing relative pressure indicating monolayer adsorption completion. The specific surface area calculated for monolayer capacity is as per equation 3.2.

$$SSA = \frac{V_m \times a_m \times L}{22414} \quad (3.2)$$

Where SSA is specific surface area (m^2/g), V_m is the monolayer volume (cm^3 (STP)/g), a_m (nm^2) is nitrogen molecule's cross-sectional area and L is the Avogadro number.

Theoretically, in pore volume assessment, all pores are supposed to be filled when $P/P_0 = 0.99$ and hence the total pore volume equals the volume of N_2 adsorbed at $P/P_0 = 0.99$. The micropore volume is estimated using the t-plot method, where the t curve of Harkins and Jura was utilized, calculated with equation 3.3 (Webb & Orr, 1997).

$$t = \left(\frac{13.990}{0.034 - \log(P/P_0)} \right)^{0.5} \quad (3.3)$$

The t-plot method plots adsorbed volume and t i.e. the statistical thickness of an adsorbed layer at a relative pressure (estimated from equation 3.3). The curve displays a straight line at high values of t and concaves down at lower values of t in the presence of micropores. The straight line extrapolated to the y-axis gives an intercept value using which micropore volume can be estimated.

Pore size distribution had been estimated using the BJH method assuming non-connected, cylindrical pore geometry in shale samples. The Kelvin equation (3.4) relating pore diameter and relative pressure (P/P_0) is as follows:

$$RT \ln \frac{P}{P_0} = \frac{-2 \times V_L \times \gamma}{r_m} \quad (3.4)$$

Where P is the vapour pressure on curved liquid meniscus surface with an effective radius of r_m , P_0 is the saturation vapour pressure, V_L is the molar volume of the liquid absorptive, γ is the liquid surface tension, R is the universal gas constant and T is the temperature.

The fractal dimensions were estimated based on Frenkel-Halsey-Hill (FHH) method (Equation 3.5). Although there are other methods like the thermodynamic method, BET – method and Langmuir method, FHH has proven to be the best

applicable method (Jiang et al., 2016; Turlapati et al., 2020; F. Yang et al., 2014; Yao et al., 2008, 2009).

$$\ln V = \text{constant} + K \ln \left[\ln \left(\frac{P_0}{P} \right) \right] \quad (3.5)$$

Where P_0 is the saturation vapour pressure, V is the volume adsorbed at pressure P and K is a constant using which fractal dimension is estimated by equation 3.6.

$$K = (D - 3) \quad (3.6)$$

Fractal dimension (D ; equation 3.6) is a coefficient that describes the surface roughness of the sample and it ranges 2 – 3. The values closer to 2 are for smooth surfaces and values tending towards 3 represent highly rough surfaces.

CHAPTER 4: MINERALOGICAL AND ELEMENTAL ANALYSIS

4.1 Chapter overview

Petrographical, mineralogical and elemental analysis based on thin-section XRD, FE-SEM, XRF and ICPMS are investigated in this chapter. Comprehensive megascopic characterization of cores is essential to demarcate zones of interest. Mineralogical setup and fabric of shales are deciphered based on thin-section analysis. The results are further validated by XRD and FE-SEM results. The mineralogical-based brittleness index and morphological inferences are further derived based on XRD and FE-SEM analysis respectively. The XRF and ICPMS results elucidate the elemental setup of Kommugudem shales. The major oxides, trace elements and REEs elucidate the depositional setting, paleoredox, paleoclimate, paleosalinity and paleoproductivity during the Permian age in the KG Basin.

4.2 Megascopic characterization

Most of the samples indicate grey to black coloured, shale containing organic matter and silt-, clay-sized mineral grain accumulations with variable amounts of disseminated finely crystalline mica, calcite, dolomite and pyrite (Fig. 3.1). The samples show sub-vitreous to vitreous lustre, mainly carbonaceous with sandy intercalations, laminated to blocky, fissile, soft, brittle and flaky nature. Formation tends to be tight and porosity is rarely visible with the presence of laminated veins filling and uneven fractures. The plant debris and leafy impressions were observed in silty shale samples. The upper sequences are shaly and the lower sequences have intercalation of sand and shale. Thick sequences of carbonaceous and siliceous

shale are dominantly observed. Fine to medium-grained micaceous sandstone is present in the lower part of the formation (Fig. 3.1).

4.3 Petrographic analysis of mineral matter

The petrographic analysis of the shale samples shows silt and clay-sized quartz, feldspars and mica in the carbonaceous and argillaceous matrix (Fig. 4.1). The main facies are carbonaceous shale, carbonaceous silty shale, silty shale and fine-grained micaceous sandstone (Fig. 4.1). Mono and polycrystalline quartz is dominantly observed with silt-clay intercalation and organic matter flakes as the matrix. Detrital quartz (Fig. 4.1a & d) is most dominantly noted with the presence of intergranular and intragranular microquartz cement and overgrowths (Fig. 4.1b & c). Mainly K-rich feldspar with sparse plagioclase feldspar is observed. Feldspars have undergone chemical alteration to clay minerals along cleavage planes and grain boundaries. Muscovite laths predominate among the micaceous grains, with scant biotite grains. Oriented micaceous grains were observed with elongated morphology indicating post-depositional compaction. The parallel alignment at places is interrupted by coarser quartz grains (Fig. 4.1d). Based on grain analysis, the compaction effect is inferred by point, straight, convex-concave contact indicating a reduction in porosity. Fine to medium-grained quartz with floating grains indicates the possibility of intergranular porosity, filled by organic matter. Thin coal seam intercalations are associated with carbonaceous shale. Carbonaceous shale (Fig. 4.1a & b) dominantly constitutes organic matter with quartz, feldspar, mica and clay minerals. Fine-grained quartz and secondary minerals with mainly floating contact, sub-rounded to sub-angular and poorly sorted grains, associate with carbonaceous (dominantly) and argillaceous matrix. The preferred, parallel alignment of micaceous and clay mineral grains characterises fissile plane morphology. The parallel alignment at places is interrupted by coarser quartz grains. Carbonaceous silty shale (Fig. 4.1b) is an intermediate form of carbonaceous shale and silty shale. They constitute coarser mineral grains than carbonaceous shale and have higher organic matter in the

matrix than silty shale. Quartz, feldspar and micas are associated with the carbonaceous and argillaceous matrix, with poor to medium sorting. Parallel lamination of quartz and mica grains with organic matter as matrix is also observed. Silty shale (Fig. 4.1c) constitutes dominantly silica-rich silt-sized minerals like quartz and feldspar floating in a varying proportion of carbonaceous and argillaceous matrix. Mineral matter exhibits sub-rounded to angular grains with poor sorting. Clay minerals were mainly observed in a matrix with feldspar and mica. Micaceous sandstone (Fig. 4.1d) constitutes quartz, feldspars, mica and organic matter with a dominantly argillaceous matrix. Many minerals retain growth forms with fine to medium grain, poor sorting and subrounded to angular grains caused by low abrasion. The substantial argillaceous matrix effectively binds the grains, resulting in relatively hard rock. Thin section analysis indicates the presence of quartz (mono- and polycrystalline) showing undulose extinction and stretching along the C-axis, which may represent metamorphic provenance. The presence of mica, majorly muscovite and biotite suggests the granitic or schistose origin of the source rock.

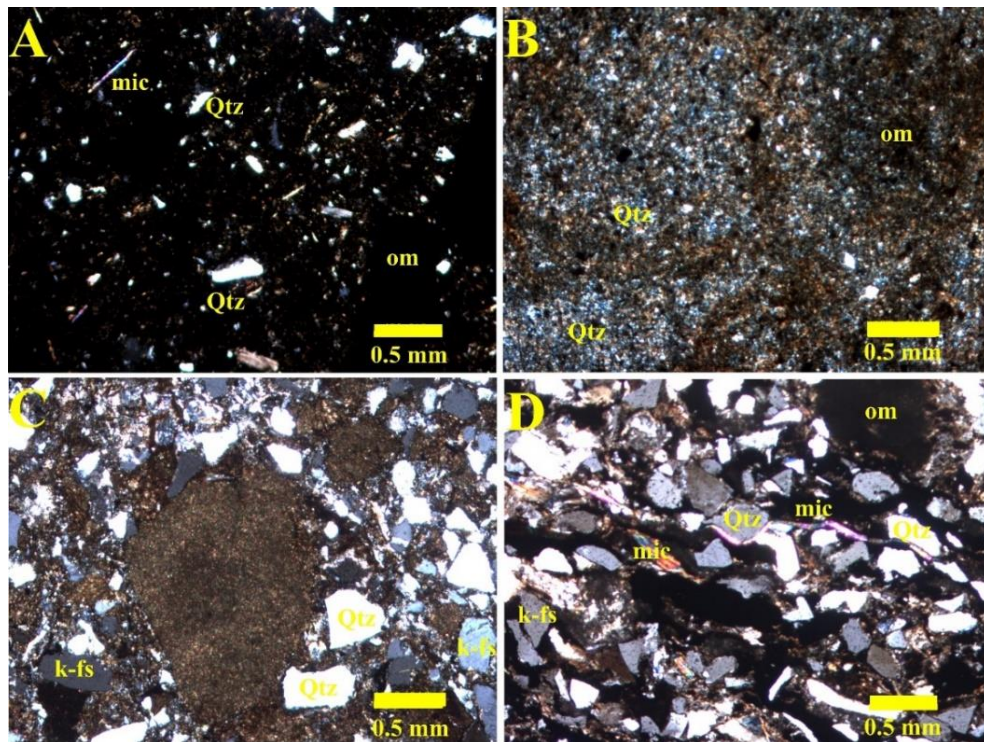


Fig. 4.1 Photomicrographs in the cross-polarized light show a) poorly sorted quartz and mica grain floating in a matrix of organic matter; b) clay-sized microquartz in association with carbonaceous and argillaceous matrix; c) silt-sized and clay-sized quartz (subangular-subrounded), feldspars and mica with argillaceous matrix; d) silt-sized quartz associated with mica grains displaying parallel lamination with carbonaceous and argillaceous matrix.

4.4 Mineralogical composition and associated brittleness index

The Semi-quantitative evaluation of minerals recognized and associated brittleness in selected shale samples from XRD is reflected in Table 4.1. XRD spectrograph as shown in Fig. 4.2a represents identified mineral phase positions. Kommugudem shale has the highest concentration of silicates with quartz, clay and feldspars (Potassium and plagioclase feldspars) as major minerals. Accessory minerals such as siderite, pyrite, muscovite and dolomite are present in certain samples. Quartz and feldspar with an average of 73.34% and 11.61% respectively are brittle and may have a major contribution to fracability in Kommugudem Formation. Clays (3.63-31.94%) are the main ductile constituent manifested as chlorite, illite and kaolinite with an average of 6.54%, 3.26% and 2.16% respectively. Siderite (average= 3.39%) and pyrite (average= 0.49%) also contribute to brittleness in Kommugudem Formation.

The sCore classification for organic mudstone is based on the weighted percentage of quartz, feldspar and mica (QFM), kaolinite, chlorite and illite summed as clays and dolomite and siderite as carbonates (Fig. 4.2b). The ternary diagram reflects that Kommugudem Formation is dominantly siliceous with relatively lower clay and carbonates as shown in Fig. 4.2b. Organic mudstone classification suggests formation is dominantly silica-dominated lithotype and clay-rich siliceous mudstone with minor presence of mixed siliceous mudstone, carbonate-rich carbonate mudstone and carbonate/siliceous mudstone.

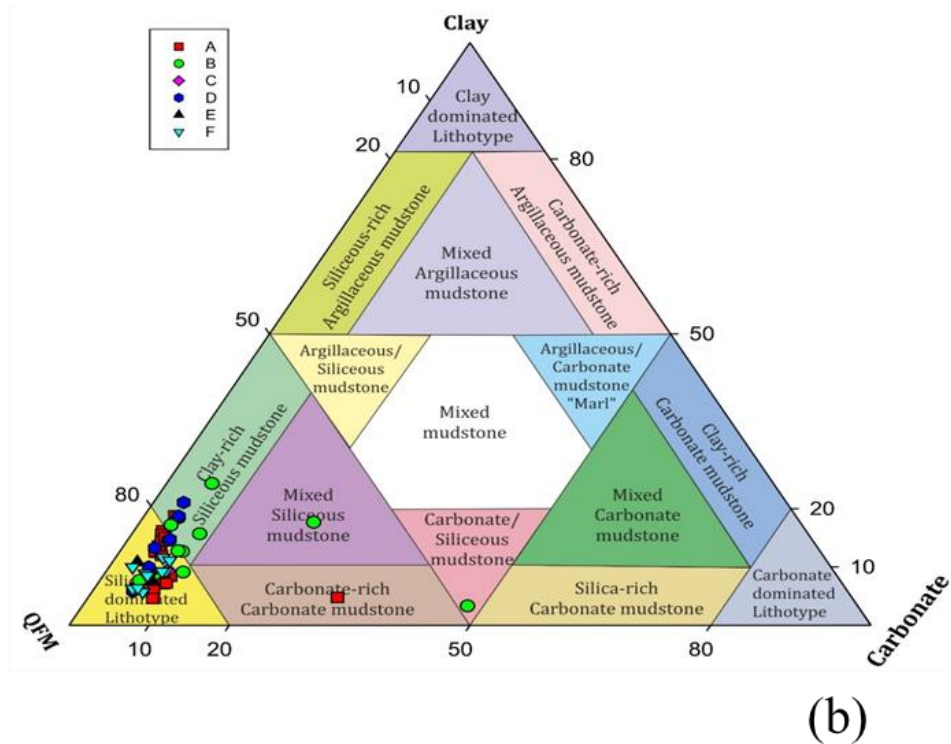
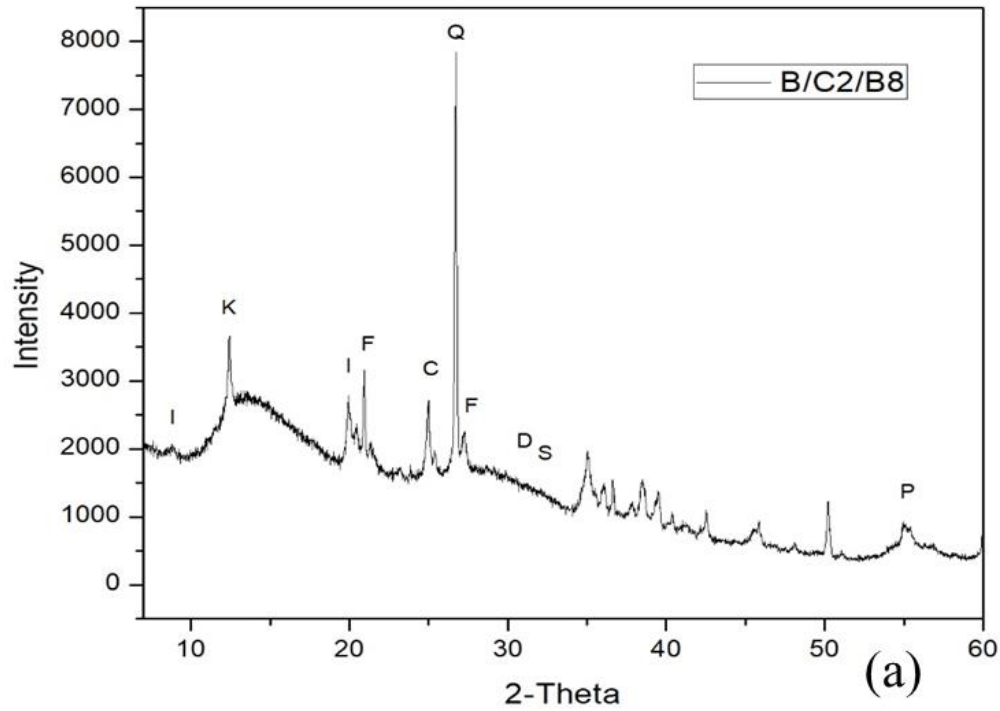


Fig. 4.2 (a) XRD crystallograph (B/C2/B8 sample) representing distinct mineral phases. Abbreviations: I: Illite; K: Kaolinite; F: Feldspar; C: Chlorite; Q: quartz;

D: Dolomite; S: Siderite and P: Pyrite; (b) Ternary diagram of sCore lithotype classification with superimposition of mineralogical composition for the selected Kommugudem shale samples (modified after Gamero Diaz et al., 2013).

Abbreviations: QFM= sum of the weight percentage of quartz, feldspars and mica.

Effective fracturing in shale is difficult in high clay/ductile zones (Kumar et al., 2018). Brittle shale is relatively prone to natural fracturing and thus may have more efficient hydraulic fracturing conditions (Rickman et al., 2008). The presence of high organic matter aids the generation, retention and storage of hydrocarbons, but gas flow can be limited if micro-reservoir zones are not connected by well stimulation (Jarvie et al., 2007). Thus, understanding the mineral composition of shale which is chemically complex and exhibits lateral and vertical heterogeneity is essential. The shale brittleness index measures the rock's ability of failure under applied stress in a brittle manner depending on petrophysical, elastic and strength properties (Altindag, 2003; Kumar et al., 2018; Rickman et al., 2008). The brittleness index based on mineralogy has stronger practicability since mineral composition data is easily accessed through XRD (C. Zhang et al., 2017). Mineralogical variation and their influence on shale brittleness and consequently fracability is a function of physicochemical properties, reservoir temperature, thermal maturity, effective stress, lithology and texture, rock strength, diagenesis, fluid type and content, clay type and abundance, TOC and porosity (Abouelresh et al., 2016; Kumar et al., 2018; F. P. Wang & Gale, 2009; Z. Yang et al., 2018). Plane of weakness such as natural fractures may also alter mechanical behaviour (Gale et al., 2007).

Mineral brittleness index (MBI) is the ratio of brittle minerals to total minerals present in a rock (Kumar et al., 2018). Broadly, quartz is the most dominant brittle matter and clay is the main ductile matter of shale (Hu et al., 2015). Thus, quartz and clay are focally emphasized in mineralogical brittleness index calculations. Progressively, TOC and minerals like calcite, dolomite, feldspar, mica and pyrite are incorporated in mineralogical brittleness index determination (Alzahabi et al.,

2015; Gamero Diaz et al., 2013; F. P. Wang & Gale, 2009). In equation 4.1 of the Brittleness index (BI-I), quartz and dolomite are considered as main brittle components, while clay and TOC are ductile components (Table 4.1; Wang and Gale, 2009). Equation 4.2 for brittleness index (BI-II) incorporates the weight percentage of quartz-feldspars-mica (W_{QFM}), total clay minerals (W_{CLAY}), carbonates minerals (W_{CAR}) and TOC (Table 4.1) (Gamero Diaz et al., 2013). Certain samples have considerable pyrite thus, Equation 4.4 is incorporated indicating a brittleness index, BI-III (Table 4.1; Alzahabi et al., 2015). The Brittleness index evaluation from equations 4.1, 4.2 and 4.3 have average values of 83.56%, 85.54% and 87.73% respectively. Most samples indicate a Brittleness index of 60-80% suggesting “Good rock” for hydraulic fracturing (Alzahabi et al., 2015).

$$BI\ I = \frac{V_{qtz} + V_{dolomite}}{V_{qtz} + V_{clay} + V_{calcite} + V_{dolomite} + V_{TOC}} \quad (4.1)$$

$$BI\ II = \frac{W_{QFM} + W_{CAR}}{W_{QFM} + W_{CAR} + W_{CLAY} + TOC} \quad (4.2)$$

$$BI\ III = \frac{Quartz + Feldspar + Pyrite}{Quartz + Feldspar + Calcite + Clay + Pyrite} \quad (4.3)$$

Based on mineralogical evidence, the Kommugudem Formation exhibits comparable composition to the brittle zones of the Barnett Shale Formation, Fort Worth Basin (Fig. 4.3a & b). The Barnett Shale consists of 20.0% to 80.0% quartz with a wide range of mineralogical variation resulting in seven different lithofacies, while Kommugudem Formation has quartz ranging 40.97% to 91.19% (Loucks & Ruppel, 2007; Mitra et al., 2010). A further similarity is

explored based on the form of minerals, which is governed by post-depositional alterations.

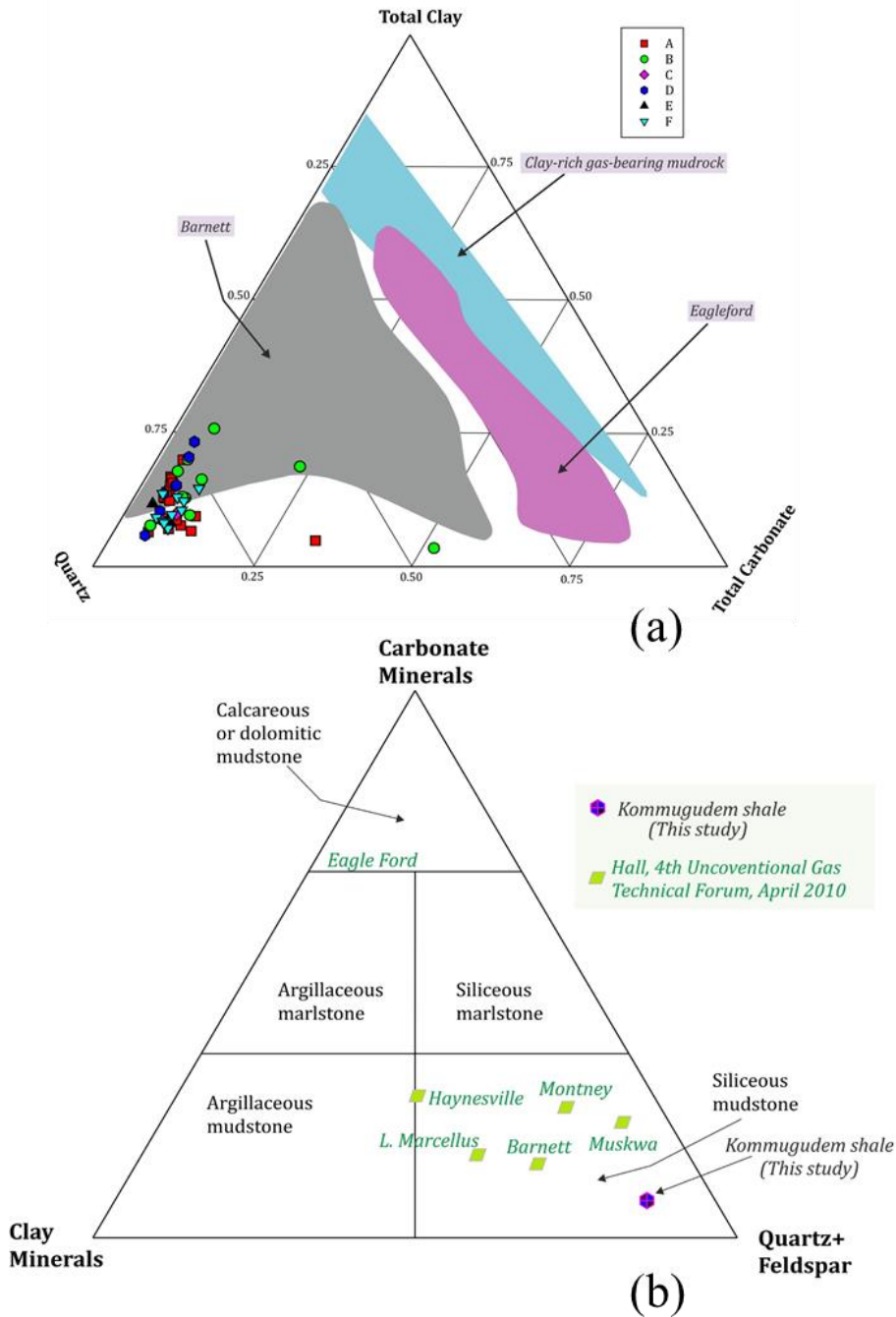


Fig. 4.3 (a) Ternary plot showing the range of composition from Kommugudem shale samples, Barnett, Eagle Ford and a clay-rich mudrock (modified from Passey et al., 2010); (b) Ternary plot with classification for organic mudstones

(modified after Allix et al., 2010) displaying average composition of the main shale plays from North America and Kommugudem shale.

4.5 FE-SEM associated morphological and mineralogical characteristics

FE-SEM high-resolution images of shale samples visually indicate mineral and organic matter and their associated pore structures. The FE-SEM assessment of selected shale samples supports the mineralogical results derived from XRD and a few representative photomicrographs are described in Fig. 4.4. The analysis reveals that Kommugudem shale is predominantly composed of silica-rich minerals with the presence of different minerals i.e.: quartz, feldspar (orthoclase, microcline and plagioclase), clays (chlorite, kaolinite and illite) and pyrite (Fig. 4.4). Organic matters are seen as flakes and as pore-filling materials (Fig. 4.4b). FE-SEM analysis revealed vast diversity in surface morphologies with variable pores size and shapes. FE-SEM analysis of samples exhibits variation in surface morphologies with diverse pores size (5 nanometres to few micrometres) and shapes (macropores to nanopores; irregular, circular, elliptical, elongated and triangular) in the mineral and organic matter. The mineral matter has a relatively higher density of microcracks and microfractures than the organic matter which may induce the flow of hydrocarbons (Hazra et al., 2016). The intercrystalline and intracrystalline pores have been identified in mineral and organic matter, which may operate as hydrocarbon storage sites (Fig. 4.4).

The micro and mesopore surfaces are mainly rough and irregular in most mineral matter exhibiting both slit and cylindrical pores (Fig. 4.4). Dominantly quartz and feldspar laths with a diagenetic clay coating and associated intercrystalline and intracrystalline pores were observed (Fig. 4.4a). The organopores are exhibited in organic mass as intracrystalline pores forming a sponge-like network of varying sizes. The organopores are ellipsoidal shaped with most pores exhibiting major axis oriented perpendicular to the grain margin (Fig. 4.4b). Intergranular pores are most dominantly observed with clays and pyrite. Clay is examined with the presence of chlorite, kaolinite and illite clay (Fig. 4.4c & d). Iron manifested as pyrite was

detected as framboidal, octahedral and nodules form in FE-SEM images (Fig. 4.4e & f). The siliceous shale also exhibits silica occurring as over-growth grains or recrystallized silica also exhibiting dissolution pores (Fig. 4.4g). Natural microfractures are also detected in the mineral matter (Fig. 4.4h).

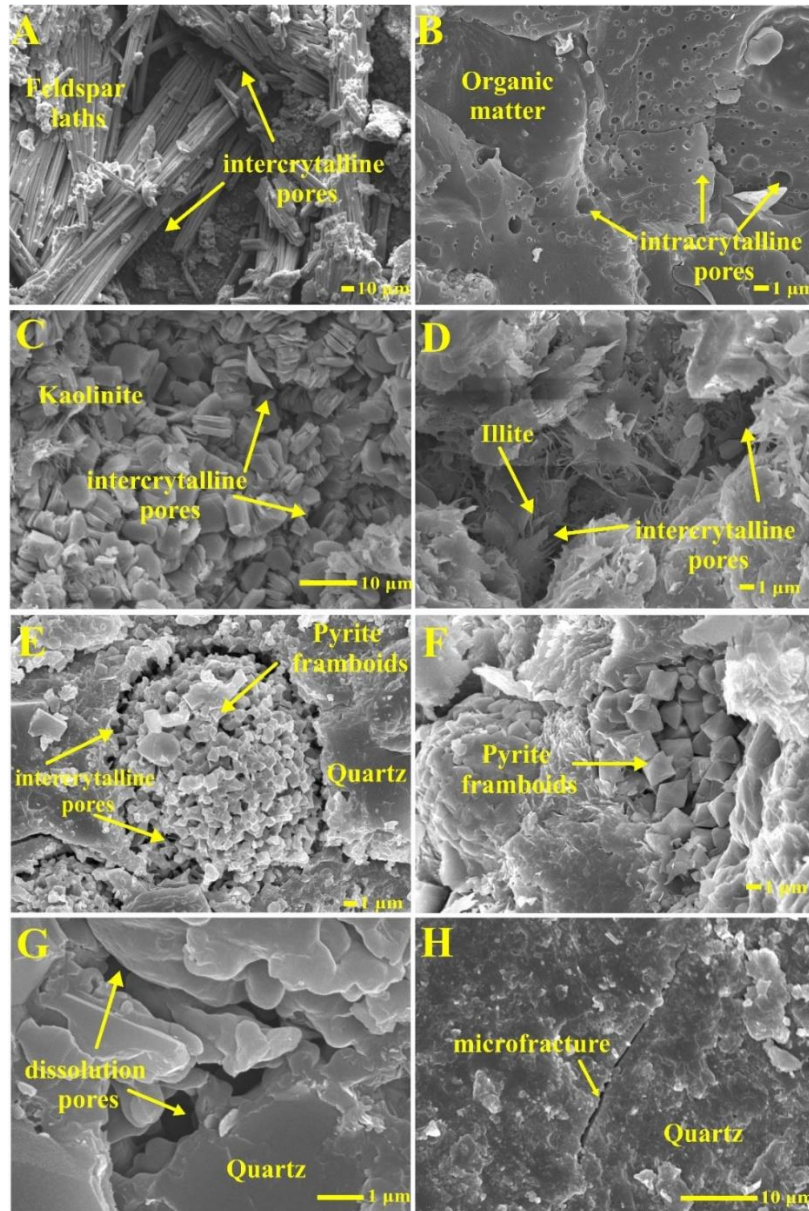


Fig. 4.4 SEM photomicrograph representing (a) Feldspar laths in the argillaceous matrix with intergranular pores; (b) Spongy network of organic matter with intragranular pores; (c) and (d) Kaolinite and illite clay with intergranular pores

respectively; (e) and (f) Pyrite framboids; (g) Silica occurring as over-growth grains or recrystallized silica exhibiting dissolution pores; (h) Natural microfracture developed in quartz grain.

4.6 Major oxides

The shales show high silica content similar to average shale (AS). The values range widely between 39.03 - 72.23 % with an average of 58.39% (Table 4.2). Higher Al_2O_3 values (15.00 - 24.74% with an average of 19.86%) indicate clay influx in the depositional basin. Fe_2O_3 is abundant with values ranging between 0.24 - 12.02% and an average of 4.13% and is a higher concentration than AS. TiO_2 values vary between 0.46–1.76%, leading to a high ratio of $\text{Al}_2\text{O}_3/\text{TiO}_2$. CaO content is low (0.12-2.34%), whereas high values of Na_2O (0.10 – 2.70) and K_2O (1.31-5.45) are observed. Important major oxide ratios and weathering indices are given in Table 4.3. The lithological classification based on the chemical composition of $\text{SiO}_2/\text{Al}_2\text{O}_3$ versus $\text{Fe}_2\text{O}_3/\text{K}_2\text{O}$ (Herron, 1988) indicates that the samples lie in the shale zone, except one in Fe-shale (Fig. 4.5).

The original composition of ancient mudrocks is indicated by $\text{K}_2\text{O}/\text{Al}_2\text{O}_3$ ratios for clay minerals (0.0 to 0.3) being markedly different from those for feldspars (0.3 to 0.9) (Cox et al., 1995). In the present study, $\text{K}_2\text{O}/\text{Al}_2\text{O}_3$ ratios (0.09 and 0.22) represent clay minerals, particularly kaolinite and illite. The ternary plot of the major oxide indicates SiO_2 enrichment relative to Al_2O_3 and CaO in Kommugudem shales (Fig. 4.6a). The chemical maturity index (CMI; $\text{SiO}_2/\text{Al}_2\text{O}_3$) represents the compositional maturity trend as a function of climate and ranges 2.34-4.35 (average= 3.04) (Suttner and Dutta, 1986).

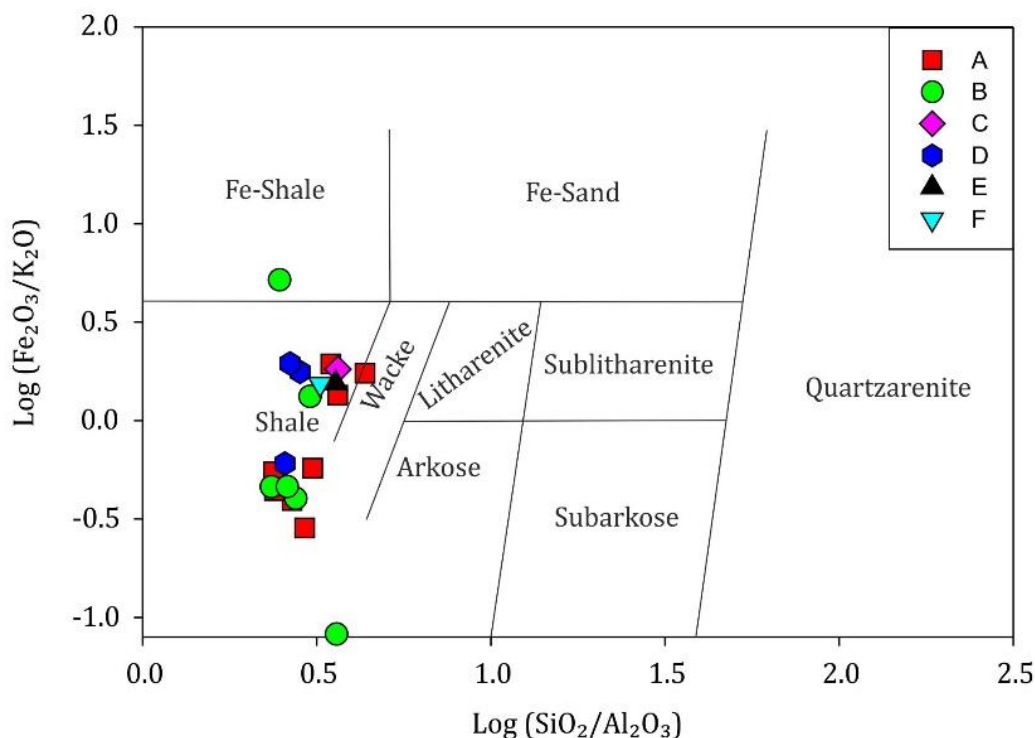


Fig. 4.5 Lithological classification of Komugudem shales based on the chemical composition of $\text{SiO}_2/\text{Al}_2\text{O}_3$ versus $\text{Fe}_2\text{O}_3/\text{K}_2\text{O}$ (modified after Herron, 1988).

Phosphorus has no notable enrichment in the selected samples. When compared to Average Shale, most samples have low Na concentration with the dominance of K-feldspars over plagioclase. Titanium is a diagenetically stable component and constitutes an enrichment factor (EF) in the range of 0.64 - 1.87 (Table 4.3). A weak, albeit, positive correlation between TiO_2 and Al_2O_3 ($r = 0.39$) indicates Ti occurrence in clay lattices or detritus of constant source. Terrigenous component percentage ($\text{TCP} = \text{Ti}_{\text{sample}}/\text{Ti}_{\text{average shale}} \times 100\%$; Murray and Leinen, 1996) ranges 0.59-2.26 and exhibits a weak negative correlation with TOC content (Table 4.3). This also rules out any possibility of biogenic silica contribution in the sediments. $\text{Al}_2\text{O}_3/\text{TiO}_2$ ratio ranges 11.40-33.05 (Table 4.3) indicating an intermediate (dominantly) to felsic igneous rocks provenance for Permian shales. $\text{MgO}+\text{Fe}_2\text{O}_3$ content within the samples ranges from 0.69-12.67 wt%, reflecting mafic mineral input in the provenance.

The A–CN–K diagram of Kommugudem shales ($\text{Al}_2\text{O}_3\text{-CaO} + \text{Na}_2\text{O-K}_2\text{O}$) tends toward high silica and is similar to the Average shale (AS) distribution (Fig. 4.6b). The chemical index of alteration (CIA) in the Kommugudem shales ranges from 66.42-90.90, with an average of 80.75. The chemical index of weathering (CIW; $\text{Al}_2\text{O}_3/(\text{Al}_2\text{O}_3 + \text{CaO} + \text{Na}_2\text{O}) \times 100$ (molecular proportions; Harnois, 1988) ranges between 75.14 - 98.74 with an average of 93.88. The CIA and CIW indicate that weathering conditions were moderate to severe in the Upper Early Permian age during the deposition of Kommugudem shales. The rise in CIA values represents an increase in the concentration of clay minerals to feldspar, as well as a high concentration of Al_2O_3 rich clay minerals such as kaolinite. These values are relatively higher than Universal Continental Crust (60.11 and 70.89, respectively; McLennan, 2001), reflecting moderate to severe weathering. The index of compositional variability [$\text{ICV} = (\text{Fe}_2\text{O}_3 + \text{K}_2\text{O} + \text{Na}_2\text{O} + \text{CaO} + \text{MgO} + \text{MnO} + \text{TiO}) / \text{Al}_2\text{O}_3$] ranges from 0.21-1.25 and quantifies alumina concentration in relation to the other main cations (Table 4.3).

The paleoproductivity is assessed using ratios of P with Ti or Al (Algeo et al., 2011), which, eliminates the impact of terrigenous detritus and autologous elements. The P/Ti values are low in Kommugudem shales (<0.34 ; Table 4.3), suggesting that reduced primary productivity characterized the sedimentary environment (Algeo et al., 2011). However; the depositional environment favoured organic matter preservation. The correlations of P/Ti vs. TOC ($r = -0.31$) and P/Al vs. TOC ($r = -0.39$) exhibit a very weak negative relationship (Table 4.3), supporting the above observations. The tectonic setting discriminatory diagram of $\text{Log}(\text{K}_2\text{O}/\text{Na}_2\text{O})$ versus SiO_2 of samples from the Kommugudem Formation (Fig. 4.7) represents the deposition of sediments in a passive continental margin setting.

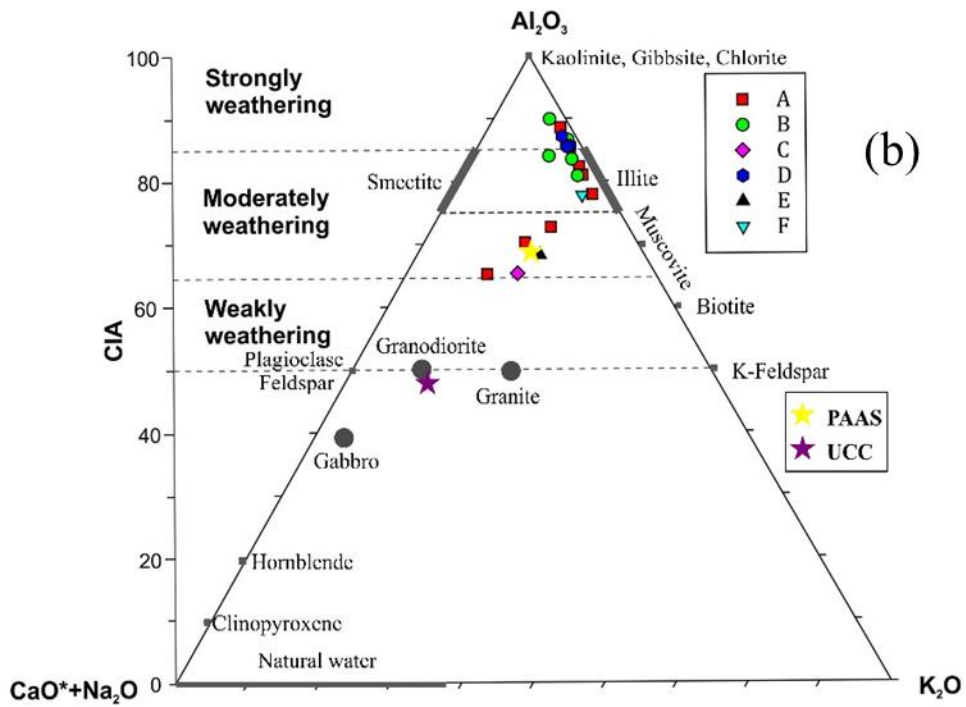
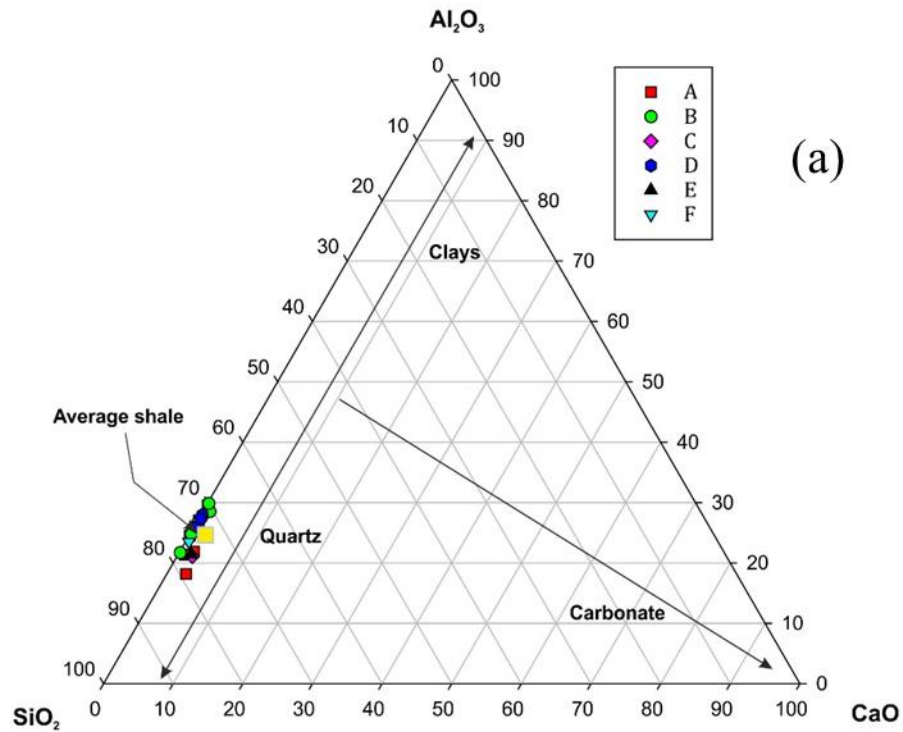


Fig. 4.6 (a) Ternary diagram showing relative proportions of quartz-clay-carbonates in Kommugudem shales; (b) Ternary diagram showing the relative proportion of Al_2O_3 -($\text{CaO}+\text{Na}_2\text{O}$)- K_2O in Kommugudem shales. UCC = upper

continental crust and PAAS = Post Archaean Australian shales (modified after Nesbitt & Young, 1984).

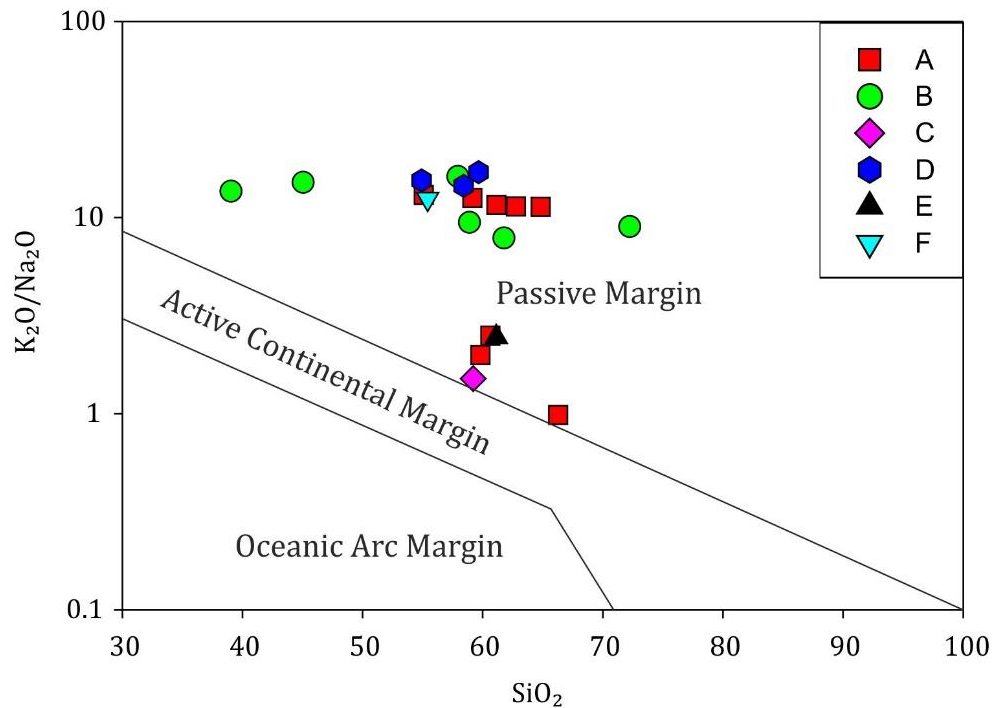


Fig. 4.7 Tectonic discriminatory diagram ($\text{Log K}_2\text{O}/\text{Na}_2\text{O}$ vs. SiO_2) for Kommugudem samples (modified after Roser & Korsch, 1986).

4.7 Trace and rare earth elements analysis

Trace element values were compared with average shale (AS) and element enrichment factors ($\text{EF}_{\text{element}}$) is calculated as $\text{EF}_{\text{element}} = (\text{element}/\text{Al})_{\text{sample}} / (\text{element}/\text{Al})_{\text{average shale}}$ (Wedepohl, 1971) (Table 4.4). If EF is higher than one, an element is considered enriched compared to AS (Tribouillard et al., 2006). The typical shales exhibit enrichment patterns as $\text{Mo} > \text{Pb} > \text{Zn} > \text{V} > \text{Ni} > \text{Cu} > \text{Cr} > \text{C}$ where Kommugudem shales exhibit the highest enrichment for Co, Cr, Mo, Zn and Pb (Rimmer, 2004).

The REEs in the selected samples ranges between 63.94 ppm and 405.83 ppm, with an average of 251.83 ppm. The LREE/HREE ranges from 4.58-12.69, with an average of 9.20 indicating slight LREE enrichment relative to HREE (Henderson, 1984; Taylor & McLennan, 1985). The REEs were normalized using the Post-

Archean Average Shale (PAAS) by the equation: $(\text{element})_N = (\text{element})_{\text{sample}} / (\text{element})_{\text{PAAS}}$. The PAAS normalized REE plot (Fig. 4.8) of the Kommugudem shales show LREE (LREE = La + Ce + Pr + Nd + Sm + Eu) enriched and flat HREE (Gd + Tb + Dy + Ho + Er + Tm + Yb + Lu) pattern, with weak positive Eu and Ce anomaly. The Trace and REEs in organic-rich Kommugudem shale samples have been used as paleoenvironmental indices by utilizing palaeoredox, paleoclimate and paleosalinity markers and ratios utilized in the study.

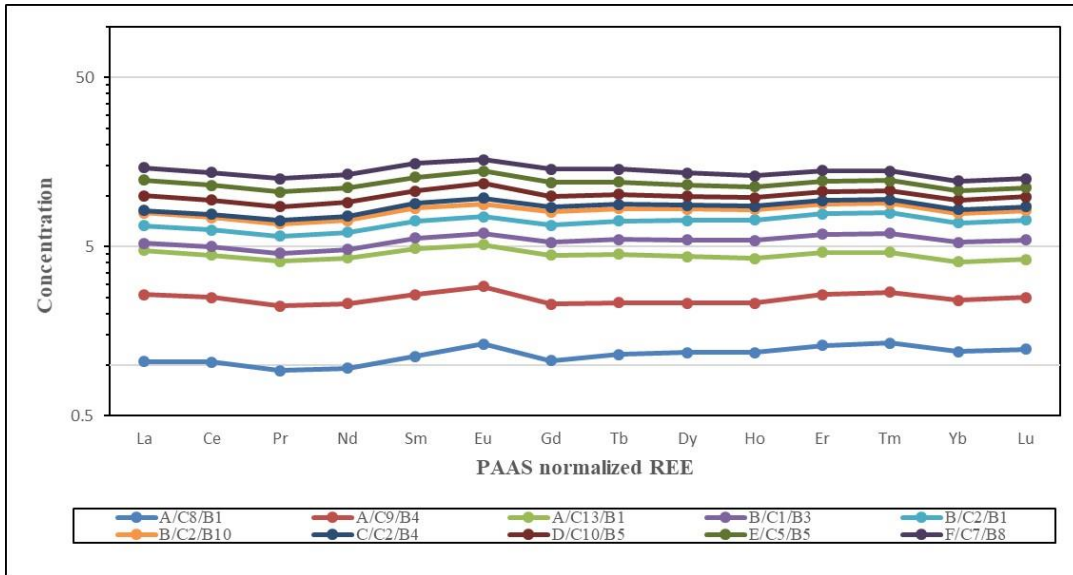


Fig. 4.8 PAAS normalized REE concentration (ppm) in Kommugudem Formation.

The deposition of minerals (mostly clay) in fine-grained sediments and/or organic matter is suggested by the REE enrichment (Mani et al., 2016). Europium and Cerium anomalies indicate a positive relationship with CIA and CIW, indicating moderately to a strongly weathered source. Intense weathering alters feldspar to clay and REEs exhibit association with fine clay mineral matter and readily accommodate in clay minerals with alumina and ferric iron enrichment. Europium anomalies investigated in the Gondwana sediments may have been inherited from the parent rock from which the clay minerals were derived. The positive anomaly indicates Europium remobilization due to diagenesis under reducing conditions

(German & Elderfield, 1990). The $(\text{Gd}/\text{Yb})_{\text{N}}$ value is reported to be less than 2 (0.69-1.69; Table 4.5) in Post-Archean strata, signifying a Post-Archean provenance of the Kommugudem Formation (Henderson, 1984). The $(\text{La}/\text{Yb})_{\text{N}}$ ratio (0.40 to 1.81; Table 4.5) indicates a high sedimentary rate during the deposition of Kommugudem shales (J. Ding et al., 2018). The high sedimentary rate causes weak REE fractionation, which is supported by PAAS normalized REE distribution trend.

4.7.1 Detrital proxy and tectonic setting

The EF value of certain LILE elements (Rb, Ba and Pb) is close to 1 (Table 4.4), suggesting sedimentation during Permo-Triassic was similar to AS. Rb association in marine sediments implies detrital presence and generally fluctuates as a result of detrital and biogenic dilution (Ross & Bustin, 2009a). The EF values of Nb and Th are greater than AS (up to 2) also implying the terrigenous influx in Kommugudem sediment (Table 4.4). Nb and Th enrichment suggest the detrital source of the quartz and probable lithogeneous source terrain due to the insoluble nature, consequent diagenetic immobility and low sea-water/continental crust distribution (Ross & Bustin, 2009a; Taylor & McLennan, 1985).

The tectonic setting by La-Th-Sc ternary plot (Fig. 4.9a) for Kommugudem Formation is indicated as a passive margin (Bhatia & Crook, 1986). The La/Sc vs Th/Co plot (Fig. 4.9b) reveals igneous felsic volcanic rocks as the probable provenance for the Kommugudem Formation (Cullers & Podkovyrov, 2000). The samples exhibit Ce anomaly ranging 0.98-1.12, where slight anomalies ($\text{Ce}/\text{Ce}^*=0.90$ to 1.30) suggest deposition in continental margin regimes (Murray et al., 1990). Thus, the proxies indicate detrital sediments dominantly sourced from felsic volcanic rocks in the passive tectonic continental margin.

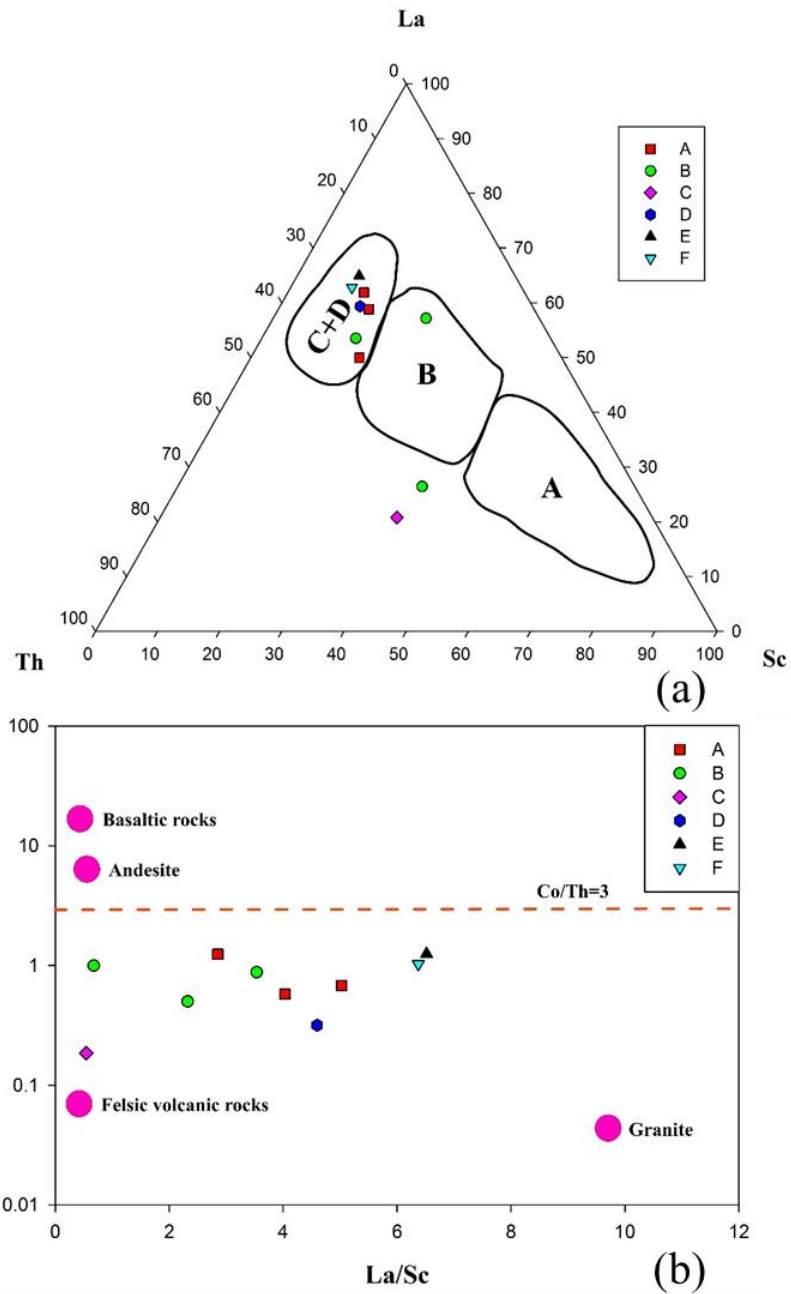


Fig. 4.9 (a) La-Th-Sc ternary plot visualizing tectonic setting for Kommugudem Formation where, A, B, C and D represent oceanic island arc, active continental margin, continental arc and passive margin respectively (modified after Bhatia & Crook, 1986) and (b) La/Sc vs Th/Co plot indicating felsic volcanic rocks as the source of origin for Kommugudem Formation (modified after Cullers and Podkovyrov, 2000).

4.7.2 Paleoredox conditions

Redox-sensitive elements with the potential to be diagenetically remobilized have been considered for interpretation (Table 4.6). Commonly used redox-sensitive trace elements include Ni, Co, Cr, V, Mo, Cu, Zn and U. The Ni/Co, U/Th, Cu/Zn, V/Cr, $V/(V + Ni)$, Mo/U, U/Al, δU and Mo/TOC ratios are utilized as paleoredox indicators and dominantly indicate dysoxic to oxic water column conditions (J. Ding et al., 2018; Hatch & Leventhal, 1992; Jones & Manning, 1994; Rimmer, 2004; Ross & Bustin, 2009a). These observations are consistent with the REEs as reflected by Europium and Cerium anomalies.

Ni, U and V diffuse more easily in sediments during reducing conditions with organic matter existence while behaving conservatively in oxic waters (Algeo & Maynard, 2004; Breit & Wanty, 1991; Bruland, 1983). Cr and Co concentrations are determined by detrital content and are hence unaltered by redox conditions (Ross & Bustin, 2006, 2009a). Contrariwise, Thorium is relatively stable under oxic conditions (Holland, 1984). Thus, the Ni/Co, U/Th and V/Cr ratios are indicative of redox conditions with Ni/Co and U/Th ratios ranging 0.44-4.10 and 0-0.28 respectively indicating oxic to dysoxic conditions (Dypvik & Harris, 2001; Jones & Manning, 1994). V/Cr ratio also reflects the paleo-oxygenation index and ranges 0.72-1.46 generally signifying oxidizing conditions, whereas values near one indicate that the O_2 - H_2S interface was prevalent in the sediments (Jones & Manning, 1994).

The $V/(V + Ni)$ ranges 0.60-0.85 and the V-Ni cross plot implies under anoxic conditions, Kommugudem shales had marine input and deposition. (Fig. 4.10a). Mo and U are indicators of paleoredox conditions and water sealing degree. During early diagenesis, Mo dissolves and enters sediments under oxic conditions and conversely less easily dissolved under the reduction conditions. (Brumsack & Gieskes, 1983). The EF_U vs EF_{MO} cross plot indicates an intermediate zone between dysoxic and oxic end of unrestricted marine trend for Kommugudem shale (Fig. 4.10b).

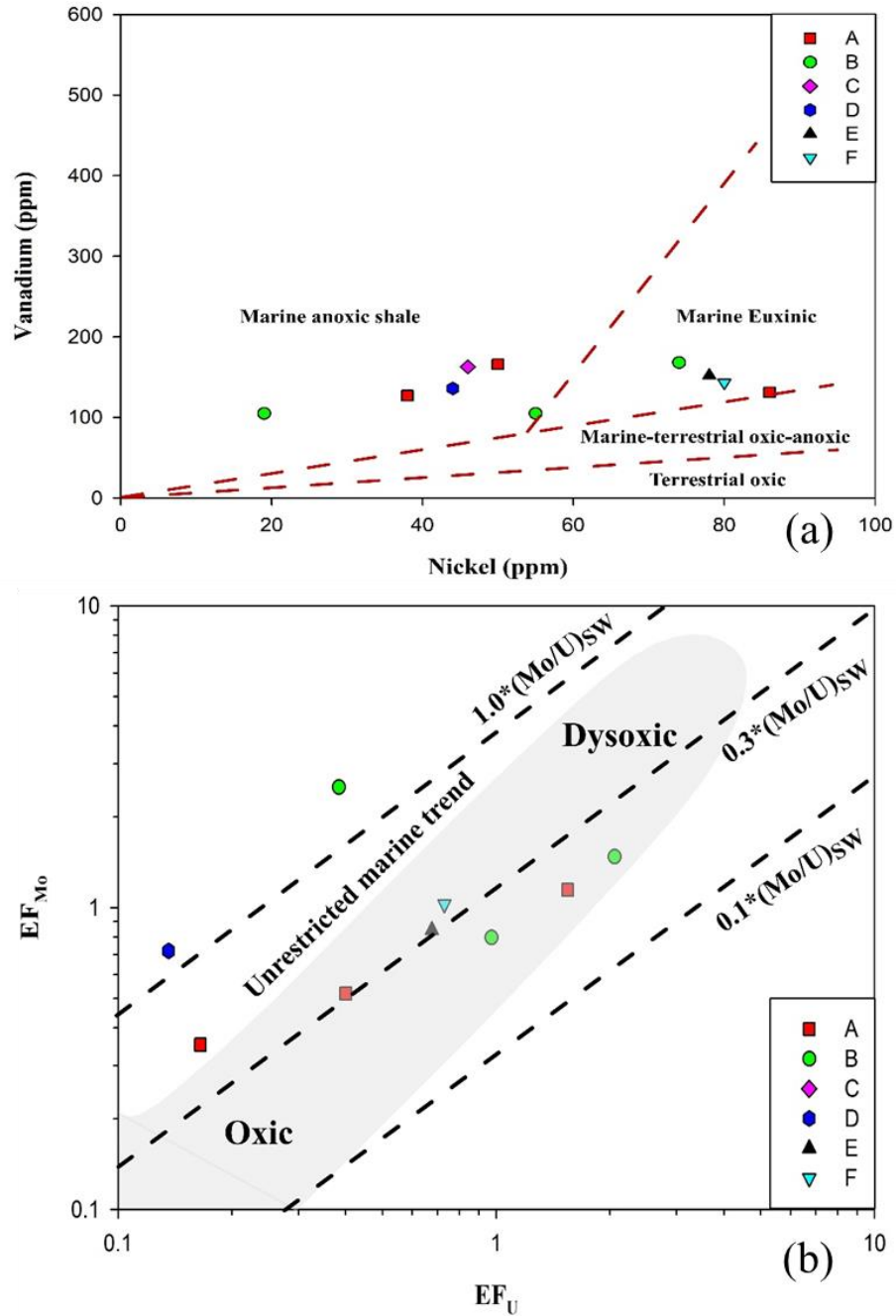


Fig. 4.10 (a) Ni vs V correlation (ppm) indicating the depositional nature of Kommugudem shales; (b) EF_U vs EF_{Mo} in Kommugudem shales reflecting the paleoredox conditions (modified after J. Ding et al., 2018).

Low Cu/Zn ratios reflect oxidizing conditions and higher values suggest reducing depositional conditions (Hallberg, 1976). Thus, Cu/Zn ratios ranging 0.19-1.24 (average= 0.54) also support dysoxic to oxic conditions in Kommugudem

Formation. Low U/Al (0-0.86) and $\delta U=(2U/(U + Th/3))<1$ infers oxic bottom water conditions during Kommugudem shale deposition (Deng & Qian, 1993; D. Li et al., 2019).

A reducing environment in a stagnant, deep-water environment leads to the formation of hydrogen sulfide causing Mo enrichment in sediment and a deficit in seawater. Low Mo/TOC ratio preservation in the sediment is a resultant of bottom water stagnant circulation leading to greater diffusion of Mo in sediment than the external supply (Algeo & Rowe, 2012; Tribovillard et al., 2012). The Mo enrichment (>1) and Mo/TOC values of the Kommugudem shale samples ranging from 0.09-8.03 with an average of 2.95 indicates probable formation in a semi-stagnant to strong environment (D. Li et al., 2019).

The Kommugudem shale indicates weak positive Europium (~ 1.14 ; 0.93-1.43) and Cerium (~ 1.03 ; 0.98-1.12) anomalies, which could be attributed to suboxic to anoxic conditions (German & Elderfield, 1990). The positive Eu anomaly indicates diagenetic remobilization under reducing conditions (German & Elderfield, 1990). Similar results are reported in highly weathered muds of Amazon deep fan of Pleistocene age, lacustrine oil shales of Nova Scotia and New Brunswick, Canada and in K/T boundary in Agost and Caravaca, SE Spain (Goodarzi, 2020; MacRae et al., 1992; Martinez-Ruiz et al., 1999). The present study and other researchers reported a positive Eu anomaly that may be induced by the diagenetic process, causing pyrite formation with high autogenetic Uranium concentrations (Goodarzi, 2020; MacRae et al., 1992; Martinez-Ruiz et al., 1999). Thus, the redox proxy is indicative of a fluvio-marine transitional environment that was preserved mainly under suboxic to oxic conditions.

4.7.3 Paleoclimate and paleosalinity

In general, shale deposit in warm and humid climates has low Sr/Cu ratios and high Ga/Rb ratios (J. Ding et al., 2018). Sr/Cu and Ga/Rb ratios range 0.91-4.09 and 0.11-0.25 respectively, also suggesting humid and warm climate (Table 4.6) (J. Ding et al., 2018; X. Li et al., 2020; Roy & Roser, 2013). Paleosaline conditions

impact organic matter preservation and contribute to the formation of the anoxic bottom of the water column (X. Li et al., 2020). The Rb/K ratio for samples ranges from 0.004 to 0.006 indicating fresh to brackish water column (Table 4.6) (Campbell & Williams, 1965; Sajid et al., 2020). Thus, the paleosaline proxy indicates an influx of freshwater in the marine environmental system.

CHAPTER 5: ORGANIC GEOCHEMICAL ANALYSIS

5.1 Chapter overview

In this chapter, geochemical analysis for estimating organic matter type and abundance, thermal maturity and hydrocarbon potential has been discussed. Source rock characteristics as discussed in the following sections were comprehensively evaluated based on RockEval, organic petrographic, biomarker and functional group assessments. High TOC and good hydrocarbon potential are observed in Wells A and B.

5.2 RockEval-based source rock characteristics

RockEval pyrolysis analysis estimates the TOC abundance, kerogen type, maturity levels and hydrocarbon generation potential for the source rock characterization (Table 5.1). The total organic carbon (TOC) varies in the range of 0.03 - 30.63 wt % (average= 3.35 wt %) with high TOC values in Wells A and B are exhibited by the coaly textured shale associated with coal seam intercalation. The Wells A (average= 3.38 wt %), B (average= 6.82 wt %) and D (average= 4.45 wt %) have relatively higher TOC than Well C (average= 0.41 wt %), E (average= 0.17 wt %) and F (average= 0.31 wt %). The HI values of samples vary from 6 to 162 mg HC/g TOC indicating type III organic matter and suggesting similar results as the stratigraphic equivalent, Raniganj shale (Varma et al., 2014). Tmax values (Table 5.1) reflect mature to post mature zone of gas generation (317°C to 607°C). GP values are varying from 0.09-45.82 HC/g rock indicating poor to excellent generation potential (Hunt, 1996). Well A and B have good GP values with 'excellent' TOC content suggesting good potential for hydrocarbon generation.

Van Krevelen cross plot (HI vs. OI) indicates the type of kerogen and hydrocarbon generated in the source rocks (Espitalié, 1986; Peters & Cassa, 1994). The HI and

OI cross-plot (Fig. 5.1a) indicate the genesis of gas-prone, type III kerogen dominantly in admixture with type II or type IV kerogen. Well A samples are type II-III and the remaining well samples are type III-IV kerogen (Hunt, 1996). HI vs. Tmax cross-plot was analyzed for kerogen type determination and as an indicator for thermal maturity and further supports the presence of type III kerogen in admixture with type II and type IV kerogen, in mature to post-mature stage (Fig. 5.1b). Well A and B samples are mostly mature to post-mature falling in oil and gas window, whereas remaining wells are in postmature and fall in dry gas window.

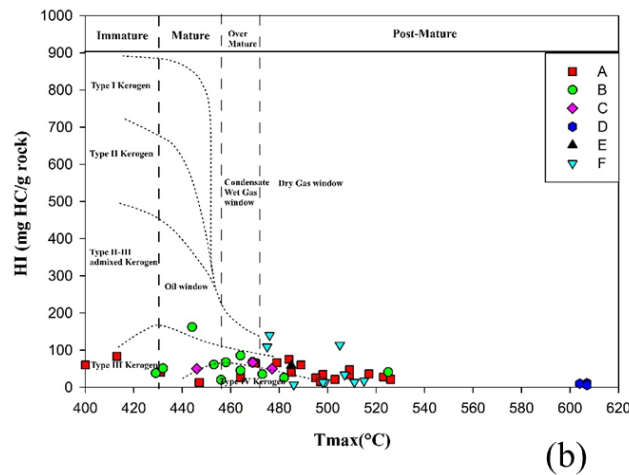
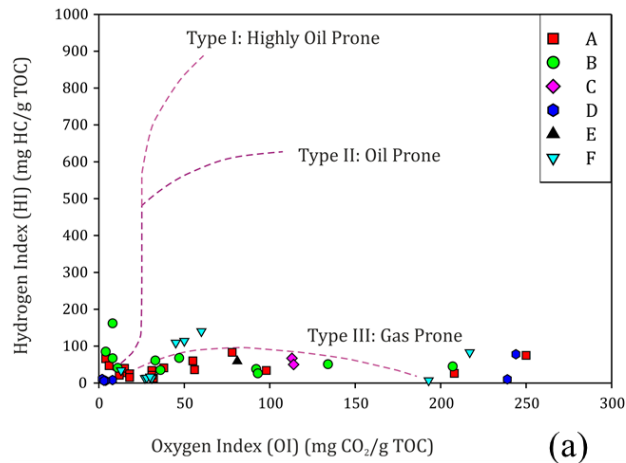


Fig. 5.1 (a) Hydrogen index-Oxygen index cross plot indicating the type of hydrocarbon generation for the Kommugudem Formation (modified after Espitalié, 1986); (b) Hydrogen index-T_{max} cross plot showing maturity range and kerogen type (modified after Espitalié, 1986).

The Production Index ($PI = S_1 / (S_1 + S_2)$) ranges 0.1–0.5 mg HC/g TOC and signifies in-situ petroleum generation (Peters, 1986). The Kommugudem shales have good hydrocarbon generation potential since shale demonstrates PI values greater than 0.1. Tmax vs Production index cross plot (Fig. 5.2) also validates mature to post mature zone of hydrocarbon generation that infers oil and gas generation potential in the sediments (Peters & Cassa, 1994). Thus, RockEval parameters (HI, OI and Tmax) infer early to post-mature stage with mainly type III kerogen in Kommugudem shale.

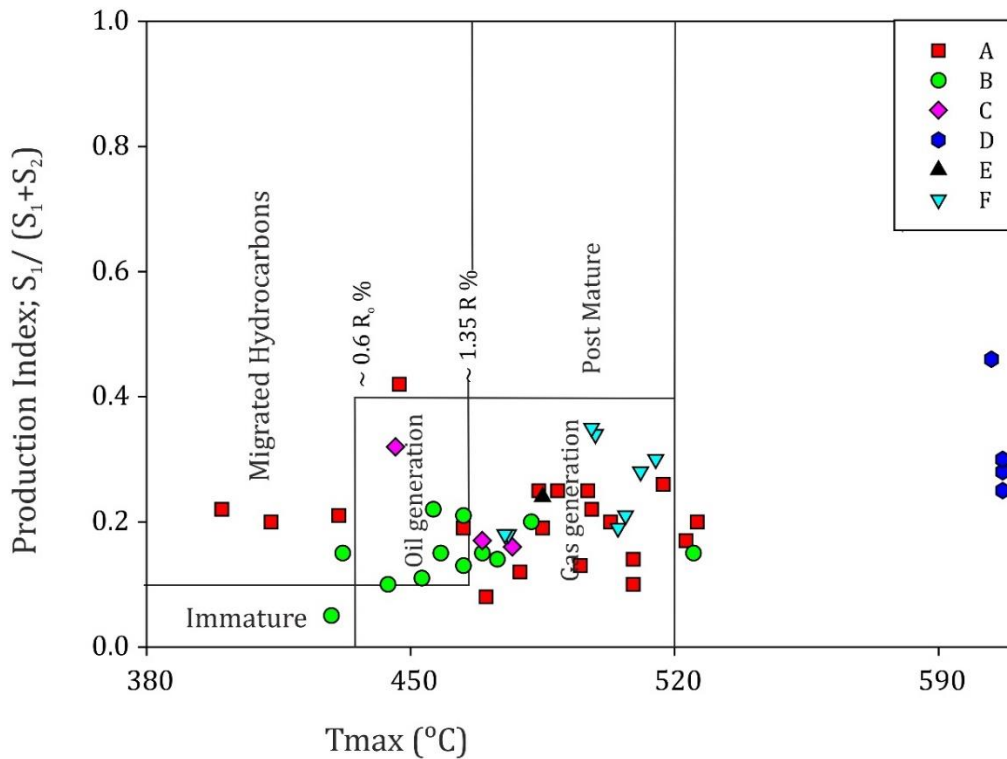


Fig. 5.2 Production Index-Tmax cross plot (modified after Peters & Cassa, 1994).

Hydrocarbon generation potential is dependent on high TOC and HI (Espitalié, 1986). Excluding the samples with very low TOC (0.5%), a fair to excellent potential for the generation of hydrocarbon is proposed based on S2 vs TOC cross plot (Fig. 5.3a). The HI vs. TOC cross-plot indicates that Wells A and B have great potential for oil and gas sources and other wells have lesser potential. (Fig. 5.3b).

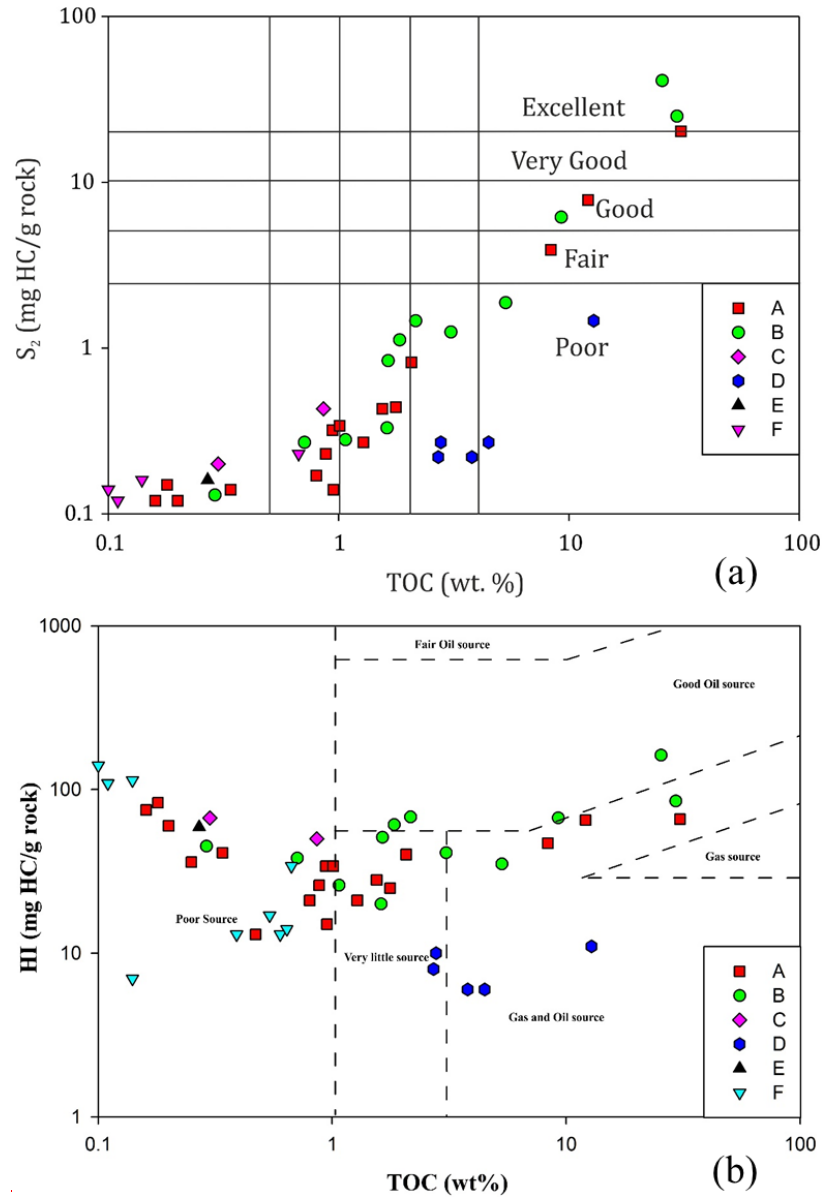


Fig. 5.3 (a) S₂-TOC cross plot (wt %) indicating hydrocarbon potential of the Kommugudem Shale (after Hunt, 1996; Peters, 1986); (b) HI-TOC cross plot indicating hydrocarbon potential of the Kommugudem shale.

The organic matter abundance, distribution and preservation are intricately linked with the depositional environment and are useful in deciphering the paleoclimate, redox, restricted or open near-shore depositional settings and paleoproductivity. Organic matter in ancient rocks is commonly altered due to post-depositional processes than its younger counterparts. Hence, it is essential to identify the

epigenetic signatures, if any in the samples, contaminating organic material. Correlation of RockEval pyrolysis parameters, S₁ vs. TOC (Fig. 5.4) suggests that the organic matter in Kommugudem shale is autochthonous in nature and lacks any contamination or existence of migrated hydrocarbon components. The wide variation in TOC content is primarily due to the vertical lithofacies change reflecting the gradational changes in the depositional environments (Rabbani & Kamali, 2005).

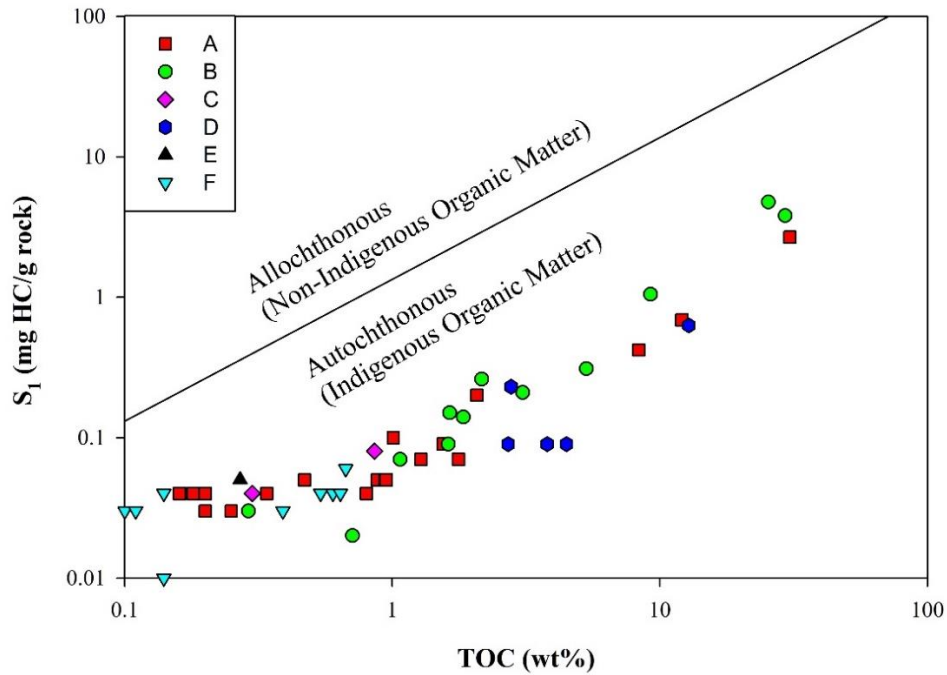


Fig. 5.4 S₁ vs. TOC correlation of organic components in Kommugudem Shales.

5.3 Maceral and vitrinite reflectance studies

RockEval-derived interpretations should be supported by maceral and vitrinite reflectance studies as recommended by many researchers (Abarghani et al., 2018, 2020; Carvajal-Ortiz & Gentzis, 2015). The macerals identified based on ICCP classification are dominantly vitrinite with the scarce and dispersed occurrence of inertinite and liptinite (Fig. 5.5). Kommugudem Formation is Lower Gondwana (Permian) shales with the major derivation of organic matter from higher plants and thus vitrinite dominates (Mani et al., 2015). Vitrinite subgroups such as collotelinite (Cot) and vitrodetrinite (Vd) are the most dominant maceral distinctly

detected in most samples (Fig. 5.5a, b & c). The vitrinite dominance is supportive of genesis by anaerobic preservation of resistant lignin and cellulose in woody tissue of terrestrial land plants (ICCP, 1998). This conforms to kerogen type III presence as observed from RockEval results.

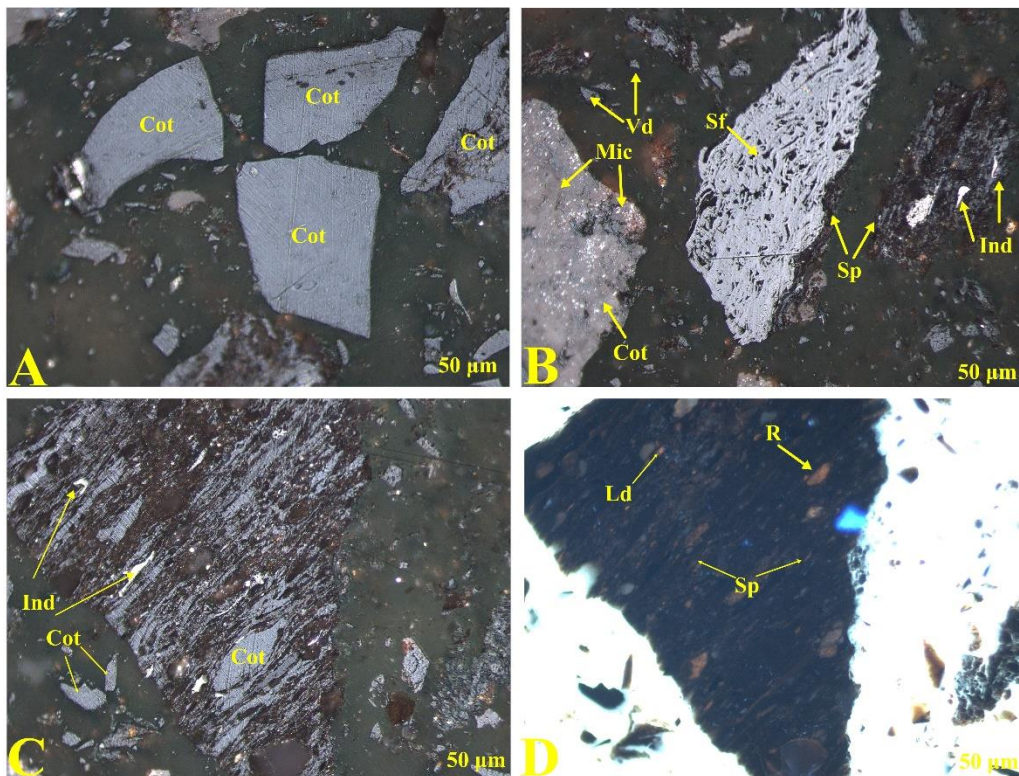
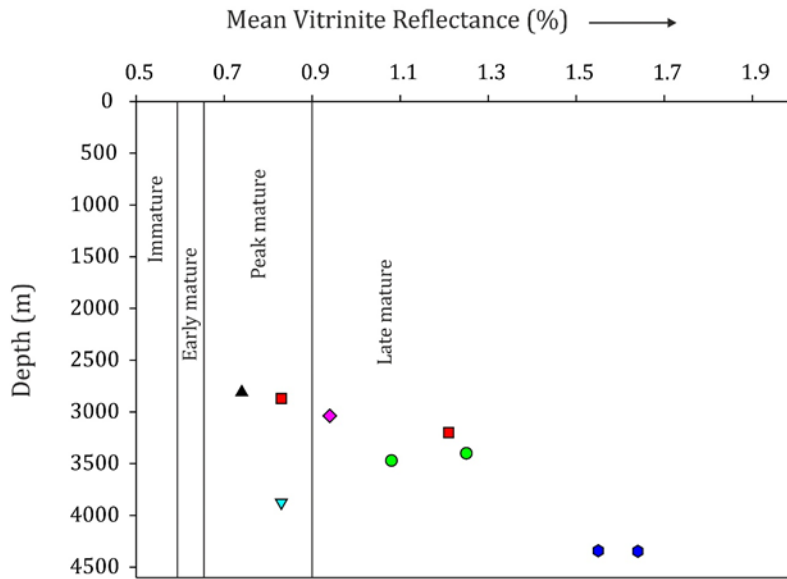


Fig. 5.5 Photomicrograph exhibiting a) dominant accumulation of collotelinite (Cot); b) collotelinite and vitrodetrinite (Vd) in association with semifusinite (Sf), micrinite (Mic) and inertodetrinite (Ind) and sporinite (Sp); c) collotelinite assemblage with vitrodetrinite and inertodetrinite; d) Sporinite, resinite (R) and liptodetrinite (Ld) accumulation.

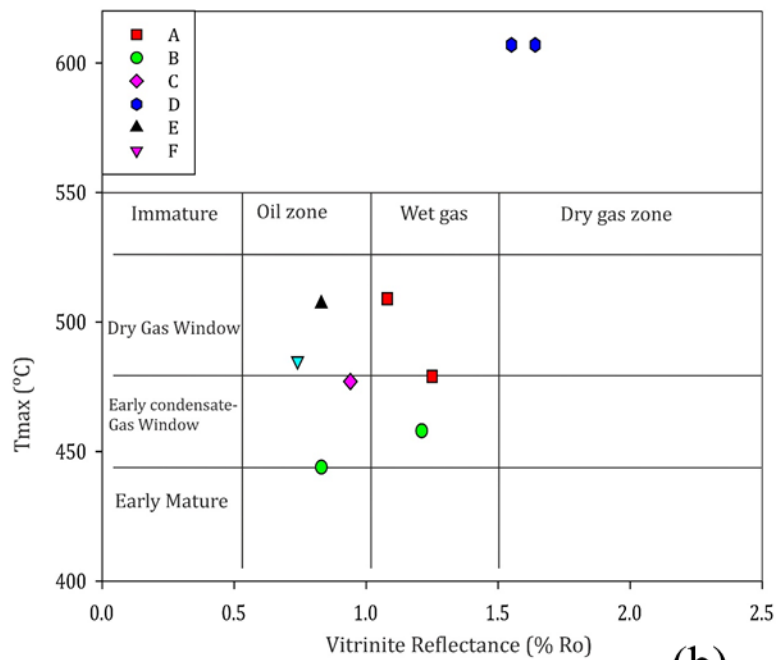
The inertinite subgroups such as semifusinite (Sf), micrinite (Mic) and inertodetrinite (Ind) are mainly observed dispersed through samples (Fig. 5.5b & c). Gondwanan samples tend to have a higher proportion of inertinite, where Permian formations are rich in inertinite macerals that constitute III/IV kerogen that may be derived from leaves and resinous woods (ICCP, 2001). Liptinite subgroups,

sporinite (Sp), resinite (R) and liptodetrinite (Ld) are hydrogen-rich and sparsely present in the selected samples (Fig. 5.5b & d). The sparsity of liptinite may be due to higher heat flow with depth on the liptinite-rich sediments causing its cracking to form hydrocarbons (Mani et al., 2015). Liptinite macerals are mainly derived from resins, waxes, spores and pollen that have undergone biogeochemical decomposition (Pickel et al., 2017).

The mean vitrinite reflectance (VRo) has been analyzed for selected shale samples ranging from 0.74 to 1.64% indicating mainly dry to wet gas generative window (Dembicki, 2009; Tissot & Welte, 1984). VRo values conform to thermal maturity data interpretation based on Tmax values ($R^2 = 0.68$). The VRo% determined from microscopic studies were correlated with estimated vitrinite reflectance ($\%ERo = 0.0180 \times Tmax - 7.16$) (Jarvie et al., 2001). The estimated and measured vitrinite reflectance demonstrates weak correlation, thus basin-specific correlation for Krishna Godavari Basin is maybe necessary. The mean and estimated vitrinite reflectance ranges between 0.83-3.76%, further supporting samples are in the peak gas generating to dry gas window zone (Tissot & Welte, 1984). Vitrinite reflectance (VRo) data (Table 5.2) shows an almost linear relationship with depth (Fig. 5.6a). Tmax and VRo cross plot (Fig. 5.6b) further supports the presence of early gas condensate to dry gas window.



(a)



(b)

Fig. 5.6 (a) Mean vitrinite reflectance-Depth cross plot for Kommugudem shale (modified after Peters and Cassa, 1994); (b) Vitrinite reflectance-Tmax cross plot for the Kommugudem shale.

5.4 Biomarker analysis

Mass spectral distribution of *n*-alkane in the total ion chromatogram (TIC) shows the presence C₁₂ to C₃₂ chain length along with acyclic isoprenoids, pristane and phytane (Fig. 5.7). The peaks show unimodal distribution with no strong odd to even predominance and thermally mature kerogen in the shales. *n*-C₁₈ is invariably the dominant alkane in all the shales. Tewari et al., (2019) using solvent extraction and thermochemolysis of *Glossopteris* leaf and stem from Permian (Lower Gondwana) Raniganj Formation from West Bengal, India reported *n*-C₁₈ to be the major component of *Glossopteris* leaf and *n*-C₁₇ and *n*-C₁₈ as major alkane biomarker from the stem. *Glossospteris* is a typical marker of lowland vegetation on the Gondwanaland during the Permian.

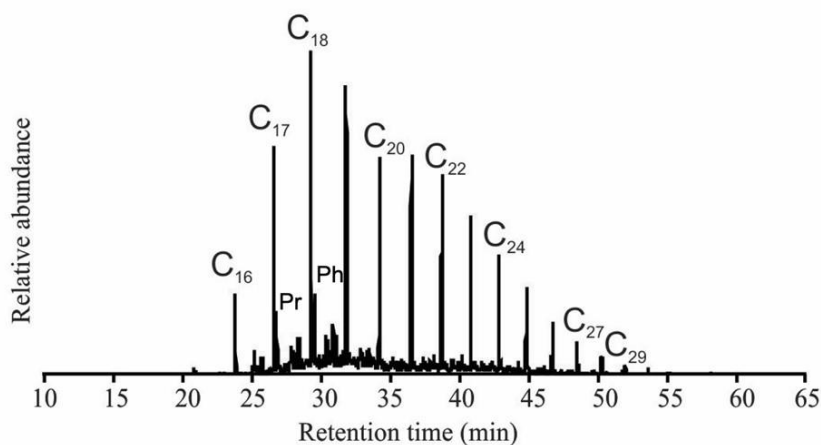


Fig. 5.7 A representative total ion chromatogram (B4/C1/B8) indicating *n*-alkane peaks in the organic extract of the Kommugudem shale.

Relative percentages of average carbon chain length for the Kommugudem shales decline from short (C₁₄–C₂₀), medium (C₂₁–C₂₆) and long-chain *n*-alkanes (C₂₇–C₃₁) by 62%, 36% and 2%, respectively. Parameters such as Carbon Preference Index (CPI) for short-chain alkane (CPI-1) and long-chain alkane (CPI-2) are used for interpreting the source of OM. The carbon preference index (CPI) is used as an indicator of odd-even preference. Here, the CPI values (0.97 to 1.49) suggest that the shales contain a mix of odd and even carbon with the predominance of odd carbon number *n*-alkanes over the even ones (Marzi et al., 1993; Table 5.3). The

odd-to-even predominance (OEP) ratio is a commonly used *n*-alkane parameter to indicate the organic matter source. The short- and long-chain *n*-alkanes groups have different odd-even predominance, which is defined by OEP1 and OEP2, respectively (Marzi et al., 1993). OEP1 values (0.89 to 1.04) are higher than the OEP2 values (0.41 to 1.10), which implies that the short-chain *n*-alkanes (C₂₁–C₂₄) have a stronger odd predominance than the long-chain *n*-alkanes (C₂₅–C₂₉). Thus, the organic matter in Kommugudem is thermally mature with a mixed source of short and medium-chain *n*-alkanes, which is generally sourced from marine/lacustrine species and micro-organisms (Peters et al., 2005). Also supported by the terrigenous versus aquatic input ratio (0 - 0.14) of Kommugudem shales, *Paq* (0.90-1.00) and the *Pwax* indices (0-0.23), respectively, which suggest the contribution by lower aquatic organisms such as algae.

An important compound class of sedimentary biomarkers, acyclic isoprenoids pristane and phytane, are used for interpreting depositional environments and palaeo-redox settings (Peters et al., 2005). The Pr/Ph ratios of Kommugudem shales range between 0.21 to 1.31 with an average of 0.76. This indicates a low to very low oxygenated, probably anoxic depositional environment for the Kommugudem shales. Further, the Pr/*n*-C₁₇ and Ph/*n*-C₁₈ ratios increase with an increased microbial decomposition of OM due to higher loss of *n*-alkanes relative to the isoprenoid alkanes during biodegradation (Peters et al., 2005). The pristane/nheptadecane (Pr/*n*-C₁₇; 0.06-0.39) and phytane/*n*-dotriacontane (Ph/*n*-C₁₈; 0.11-0.37) observed in Kommugudem shale do not indicate any biodegradation of sedimentary organic matter (Fig. 5.8a). The alkane-isoprenoid ratios suggest a mixed organic matter with marine input deposited in a transitional, reducing depositional environment.

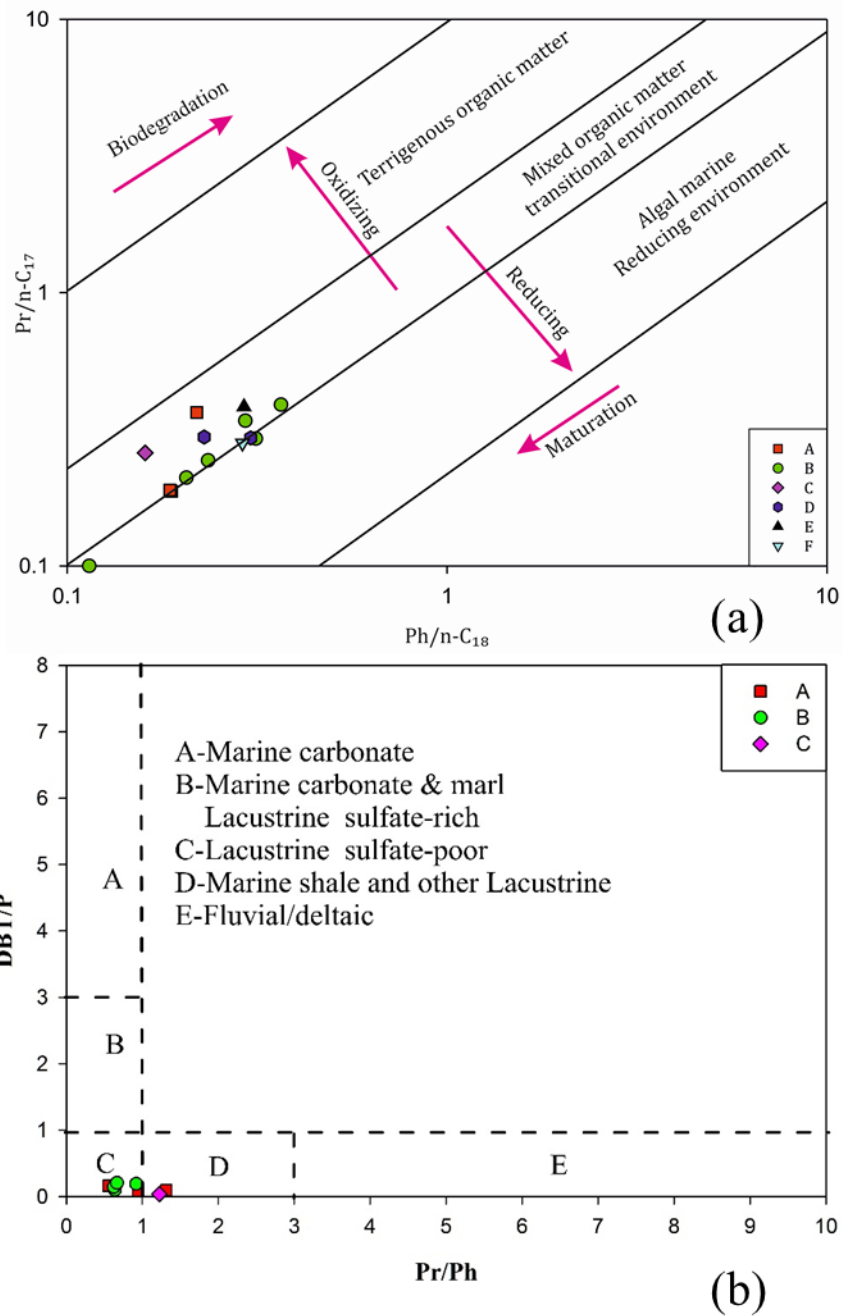


Fig. 5.8 (a) Pristane/n-C₁₇ and Phytane/n-C₁₈ cross plot signifying depositional environment of Kommugudem shales; (b) Aromatic biomarker ratios (Dibenzothiophene/Phenanthrene vs. Pristane/Phytane) indicating the depositional environment of Kommugudem shales.

The aromatic components of Kommugudem shales include naphthalenes, anthracene and phenanthrene and their alkylated derivatives and other polycyclic aromatic hydrocarbons (PAHs), such as fluoranthene and pyrene. Polycyclic aromatic hydrocarbons are generally produced as combustion/pyrolytic PAHs, higher plant-derived and diagenetically derived. In the present study, a series of 2- to 6-ringed aromatic hydrocarbons along with their alkylated homologues were identified in the samples with the following distribution:

2- and 3- ring PAHs (>50%) > 5- ring PAHs > 4- ring PAHs > 6 ring PAHs

Identified pyrolytic PAH, anthracene, phenanthrene, pyrene, fluoranthene, triphenylene and chrysene may be generated as a result of excessive heat stress on organic matter (Mani et al., 2016). Naphthalene and its alkyl homologues originate from thermal degradation of spores and sporopollenin, kerogen and cyclic sesquiterpenoids present in resinous components. Phenanthrenes and their alkyl homologues are likely to be derived from terpenoids in resin and waxes of higher plants. A thick overburden and increased temperature with burial lead to the formation of observed aromatic makers in the organic-rich sediments of Kommugudem. PAH also provides evidence on the lithology and depositional environment. The aromatic biomarker ratios (Dibenzothiophene/Phenanthrene vs. Pristane/Phytane) indicate a marine/lacustrine depositional environment for the Kommugudem shales (Fig. 5.8b).

5.5 Stable carbon isotope ratios ($\delta^{13}\text{C}_{org}$)

The average isotopic composition of plants is represented by stable carbon isotope ratios ($\delta^{13}\text{C}_{org}$) associated with terrestrial plant-derived organic matter found in rocks and sediments (Arens and Jahren, 2000). $\delta^{13}\text{C}_{org}$ integrates the relative contribution of plant species with distinct photosynthetic pathways of C3, C4 and Crassulacean acid metabolism to net primary productivity of a community. Under constant concentrations of atmospheric CO_2 , the dominance of the different photosynthetic pathways in a community is dependent on environmental and climatic factors (Arens & Jahren, 2000).

Stable carbon isotope ratios in Kommugudem shales vary in the range of -19.6 to -23.4 with an average of -21.55 ‰. From the beginning of the Permian, the average $\delta^{13}\text{C}_{\text{tom}}$ (Total organic matter) has been reported to increase and reach a mean value of -21.8‰ during the Cisuralian, before declining to values near -24‰ in the Guadalupian and Lopingian (Berner, 1990). The elevated values represent likely a time of maximum sequestration of light carbon (^{12}C) in terrestrial and shelf sediments (Berner, 1990). Consequences of these changes would include relatively higher levels of O_2 and lower levels of CO_2 (Berner, 1990) in the atmosphere.

5.6 Functional groups assessment

The analyzed functional groups and FTIR-derived absorbance spectra of selected samples from each well are given in Table 5.4 and Fig. 5.9a (Painter et al., 1981). The dominant absorbance spectra can be divided as hydroxyl structures (3000–3600 cm^{-1}), aliphatic structures (2800–3000 cm^{-1} ; 1280-1000 cm^{-1}), aromatic structures (1680-1460 cm^{-1} ; 700–900 cm^{-1}) and oxygen-containing structures (1000–1800 cm^{-1}) (He et al., 2017). Relatively stronger aliphatic, kaolinite and quartz with moderately prominent aromatic peaks are observed in most shale samples.

The medium intensity spectra near 3100-3600 cm^{-1} were allotted to the OH group occurring in most samples. The strong intensity of aliphatic C-C stretching spectra (1280-1000 cm^{-1}) and relatively less aliphatic C-H stretching spectra (2800 - 3000 cm^{-1}) were detected in the selected samples. In most samples, it was observed that the intensity of aliphatic C-H stretching bands at 2920 cm^{-1} peak was relatively more than at 2850 cm^{-1} peak. This may be indicative of long aliphatic chain presence in the organic matter of terrestrial origin (Hazra et al., 2016). Shale spectra exhibit weaker peaks of aliphatic C-H (3000–2800 cm^{-1}) and relatively stronger absorbance from inorganic components at 1500–400 cm^{-1} causing masking of aliphatic and aromatic spectra in the aforesaid range (Y. Chen et al., 2015). A relatively weaker intensity spectrum of aromatic C=C stretching is detected in the

1680-1460 cm^{-1} range. The spectra are characterized by variable aromatic CH out-of-plane bending in the 700-900 cm^{-1} range.

The Index for aliphaticity (IAL) and the Index of aromaticity (IAR) range 0.44 to 5.16 and 0.26 to 3.25 respectively (Equations 5.1 & 5.2). The higher ratios are indicative of a higher degree of presence of aliphatics and aromatics owing to higher TOC content (Misra et al., 2018).

$$\text{IAL} = \frac{2950 \text{ cm}^{-1} + 2920 \text{ cm}^{-1} + 2850 \text{ cm}^{-1}}{3030 \text{ cm}^{-1} + 2950 \text{ cm}^{-1} + 2920 \text{ cm}^{-1} + 2850 \text{ cm}^{-1} + 1600 \text{ cm}^{-1}} \quad (5.1)$$

$$\text{IAR} = \frac{3030 \text{ cm}^{-1} + 1600 \text{ cm}^{-1}}{3030 \text{ cm}^{-1} + 2950 \text{ cm}^{-1} + 2920 \text{ cm}^{-1} + 2850 \text{ cm}^{-1} + 1600 \text{ cm}^{-1}} \quad (5.2)$$

The index for hydrocarbon generation (IHG) ranges from 3.88 to 263.12 as per equation 5.3 is indicative of hydrocarbon potential (Misra et al., 2018). The higher values of IHG are indicative of organic richness and the higher potential for hydrocarbon generation.

$$\text{I}_{\text{HG}} = \text{I}_{\text{AL}} \times \text{HI} \quad (5.3)$$

The plot between genetic potential (GP) and index for hydrocarbon generation (IHG) implies poor to excellent oil and gas generation potential (Fig. 5.9b). FTIR results support RockEval findings that Wells A and B samples have fair to excellent source for gas and oil potential.

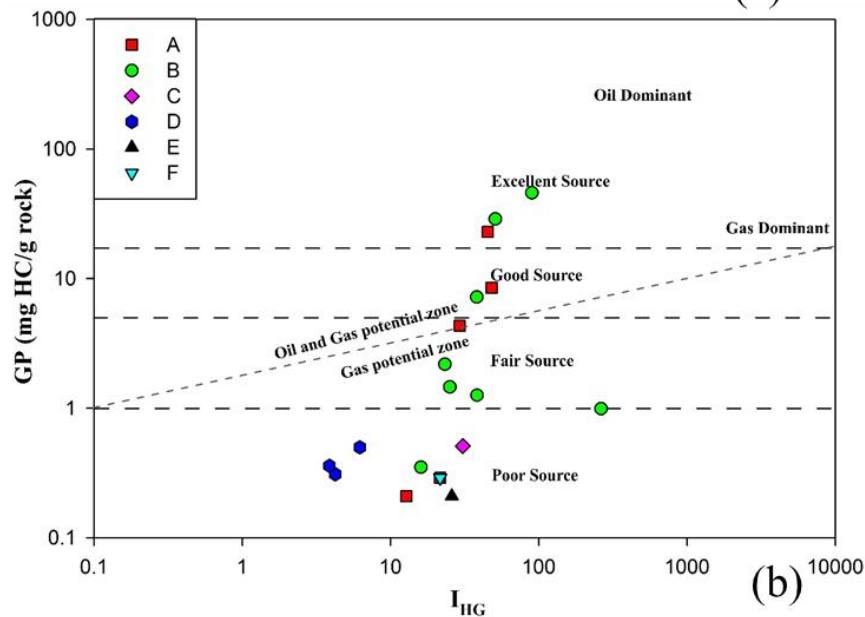
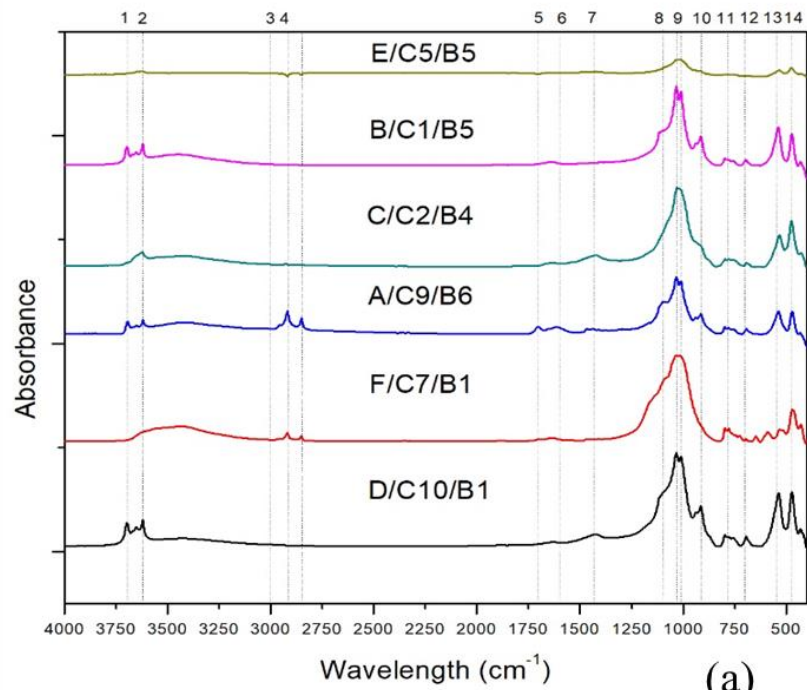


Fig. 5.9 (a) FTIR spectra of a representative sample from each well. Abbreviations: 1. Kaolinite, 2. Hydroxyl group, 3. Aromatic C-H stretching, 4. Aliphatic C-H stretching, 5. Carbonyl/Carboxyl group, 6. Aromatic C=C stretching, 7. Aliphatic CH₂ and CH₃ bending, 8. Quartz, 9. Feldspar + Quartz, 10. Kaolinite, 11. Quartz, 12-13. Kaolinite and 14. Quartz; (b) Genetic potential (GP) versus Index for hydrocarbon generation (IHG) plot of the studied shale samples (modified after Misra et al., 2018).

CHAPTER 6: PORE-ASSOCIATED ANALYSIS

6.1 Chapter overview

Pore-associated parameters based on FE-SEM and low-pressure N₂ isotherm studies have been described in this chapter. The pore characterization is essential to know storage sites and the possibility of hydrocarbon flow through them. LPNA studies coupled with fractal analysis characterise total pore volume, pore size distribution, surface area and associated roughness. FE-SEM studies also further validate the LPNA findings as discussed in the following sections.

6.2 Low-pressure N₂ adsorption

The pore structure attributes estimated from samples of Well A (sample M5 and M8), D (sample K1 and K4) and E (sample D2) and associated N₂ adsorption isotherms are as given in Table 6.1 and Fig. 6.1. The BET-specific surface area (BET – SSA) ranges between 2.47 m²/g to 24.57 m²/g, total pore volume (total PV) ranges between 0.012 cc/g to 0.78 cc/g, micropore volume ranges between 0.00051 cc/g to 0.0044 cc/g and average pore diameter ranges between 36.08 nm to 26.22 nm. The adsorption is low at low relative pressures and increases steadily exhibiting characteristics of a Type IV curve of IUPAC classification (Sing, 1985). The adsorption-desorption hysteresis loop indicates the abundance of micropores and mesopores with the presence of complex slit and cylindrical pores also supported by FE-SEM results (Labani et al., 2013).

The pore size distributions supported by the average pore diameter indicate the presence of micro and mesopores (Table 6.1 & Fig. 6.2). The micropore volumes of the samples are almost 10 percent of the total PV. The BET-SSA of the sample D2 from Well E is very high compared to other samples and high adsorption is observed in the final sections of the P/P₀ range (Fig. 6.2). The meso and macropore

dominance can also be seen in the PSD curve of D2 (Fig. 6.2). Samples M5 and M8 from Well A exhibit relatively less total pore and micropore volume compared to other samples (Table 6.1). The PSD exhibits a peak in the micropore range and also shows the dominance of the mesopore range (<10 nm), indicating the presence of both micro and mesopores. The average pore diameters for the selected shales were more in the mesoporous range (2-50 nm). The pore size distributions also show a peak in the micropore range. Pore characterization reveals that mesopores dominate in the Kommugudem shales, with a significant influence on BET-SSA, which is similar to prior investigations of other Indian shales (Hazra et al., 2018).

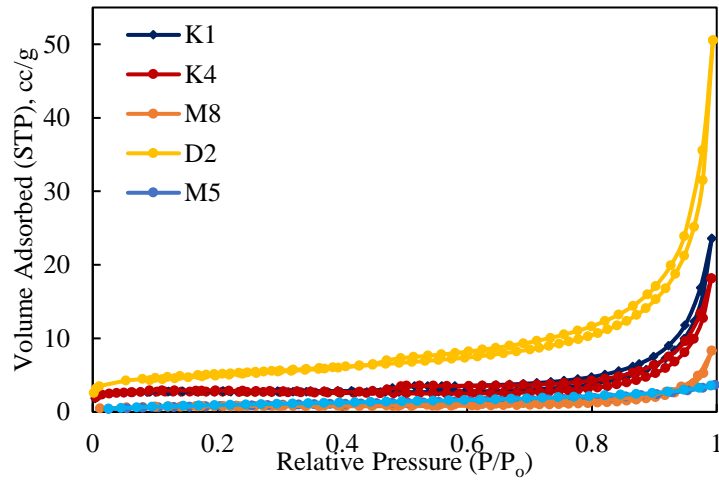


Fig. 6.1 Low-pressure N₂ adsorption/desorption isotherms of Kommugudem shale samples.

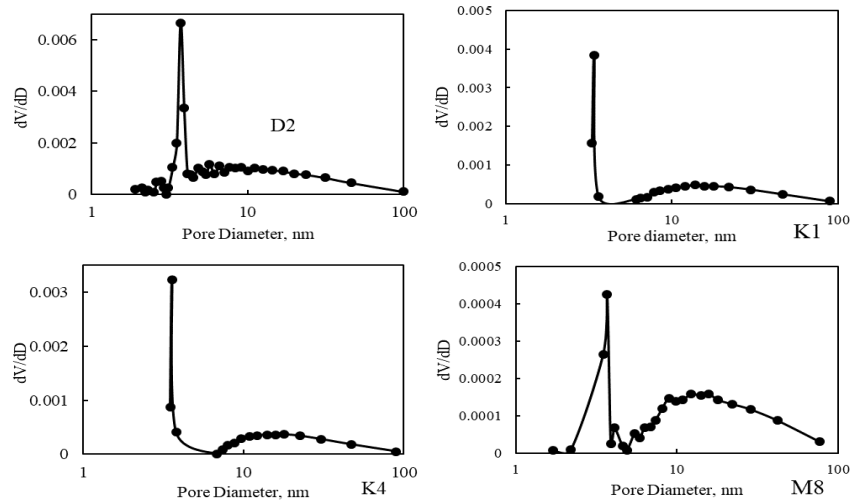


Fig. 6.2 Pore size distributions estimated from desorption data using BJH model of all samples.

6.3 Fractal analysis

The fractal analysis quantifies the irregularity and surface roughness of porous media and depends on the heterogeneity of pore structures that play a pivotal role in understanding sorption and diffusion processes (M. E. Curtis et al., 2012; Javadpour, 2009; Loucks et al., 2009; Schluter et al., 1997; Shao et al., 2017; Yao et al., 2008, 2009). Fractal dimensions estimated using the FHH method are correlated with pore structure parameters and mineralogy to determine the pore characteristics.

Fractal dimensions estimated using equation 3.3 of all the samples vary between 2 and 3 with an average value of 2.65, suggesting that the samples are rough and exhibit complex and heterogeneous pore structures. The fractal dimensions exhibit a positive relationship with quartz and clay matter ($R^2= 0.34$ & 0.60 respectively) indicating their impact on pore surface roughness and are also supported by previous studies (Hazra et al., 2018; Jiang et al., 2016). Clay and TOC are positively correlated with micropore volume and exhibit a weak positive relationship with BET-SSA. These observations indicate that clay and organic matter are microporous in nature and micropores may contribute to the surface area. Further,

it was observed that fractal dimension does not correlate with BET-SSA, indicating that surface area may not influence pore surface roughness. When shale is microporous it may constitute higher clay and TOC which increases associated surface area (Chalmers, Bustin, et al., 2012; Chalmers & Bustin, 2007). Therefore, theoretically, the fractal dimension should have a positive correlation with BET – SSA because surface roughness is proportional to surface area and micropore volume. Further, TOC and micropore volume also exhibit a positive relationship with fractal dimension ($R^2= 0.70$ & 0.42 respectively). Such relationships between fractal dimension and BET-SSA were also reported by other researchers (Hazra et al., 2018; Liu et al., 2017, 2018).

6.4 Pore morphology

The presence of microfractures and micropores was observed as (1) intragranular pores occurring in organic matter assemblages generally in sponge-like form (Fig. 4.4b), (2) intergranular and intragranular pores occurring dominantly in clay and pyrite framboids (Fig. 4.4c-f), (3) dissolution pores (Fig. 4.4g) and (4) microfractures (Fig. 4.4h). The intragranular pores are associated with organic matter and are known to be the result of thermal evolution during hydrocarbon generation (Chalmers, Bustin, et al., 2012). The FE-SEM photomicrographs of the Kommugudem shale sample show dispersed organopores with relatively low connectivity. Intragranular organic pores were of spheroidal, ellipsoid or irregular shape with sizes ranging 0.01 - 1.0 μm and formed mainly spongy network (Fig. 4.4b). The organic pores tend to be lipophilic with a high surface area and thus making them an ideal site for gas accumulation and adsorption. The organic-matter pores are especially integral as they can adsorb and store free gases ranging from 5 to 800 nm. The Kommugudem samples with a higher organic pore concentration exhibit higher vitrinite reflectance signifying the role of thermal maturation variations in organic matter-associated pore development (Loucks et al., 2009). The clay intergranular pores were detected in chlorite, kaolinite and illite floccules (Fig. 4.4c & d) These clay-associated pores may provide fluid storage and pathway and generally tend to be larger in width than methane molecules (>0.38 nm) (F. Chen

et al., 2018). Intergranular pores in pyrite framboids are dispersed through the shale matrix with poor connectivity having polygonal form with straight margins. These pores are majorly influenced by mechanical compaction, diagenetic alterations and/or dissolution of crystalline minerals (Bernard et al., 2013; F. Chen et al., 2018; T. Guo et al., 2014; Milliken & Reed, 2010). Dissolution pores in the mineral matter are resultant of dissolution due to the effects of underground water, air, or de-carbonic acid radical action during the course of pyrolysis of kerogen as seen in Fig. 4.4g (T. Guo et al., 2014). The dissolution pore genesis can be influenced by chemical diagenesis that can modify the stability of aluminosilicate minerals due to organic acid production by the thermal evolution of the shale (Loucks et al., 2012). These pores are dominantly dispersed in the matrix and exhibit low connectivity in the shale matrix. Natural fractures in shale formations are a function of mineral and organic matter, diagenesis, rock mechanics, abnormally high pressure and regional tectonic stress (W. Ding et al., 2012; Slatt & Abousleiman, 2011). Previous studies indicate organic matter shows a positive correlation with fracture density in the high maturity region as also observed in Kommugudem shale samples (Zeng et al., 2013). Natural microfractures (Fig. 4.4h) are detected in Kommugudem Formation which can augment hydraulic fracturing efficiency by providing migration pathway for gases (T. Guo et al., 2014).

CHAPTER 7: DISCUSSIONS

7.1 Chapter overview

In this chapter, the geochemical and petrophysical findings were integrated and correlated with key geological factors. The link between organic-inorganic matter, depositional environment and pore characteristics is not well known. Comprehensive microscale characterization of organic-inorganic pores may lead to a better comprehension of sorption, gas entrapment and flow behaviour. Such analyses are required if a basin is to be considered for gas production, improved shale gas recovery and/or carbon capture and storage. There are no standard shale composition classifications as each shale play is unique with wide lateral variations. Thus, prospective shale formations must be extensively examined.

The stated investigations indicate complex mechanisms with possibly significant influence of the sedimentary environment, climate, redox and salinity conditions on pore characteristics. Though further investigations are required with more extensive data to demonstrate better insight into paleoenvironmental influence.

7.2 Paleoclimate and depositional environment

The last glaciation event of Gondwana was a widespread event during Pennsylvanian to Early Permian (Isbell et al., 2003; López-Gamundí, 1997; Veevers, 1994). The transition from glacial to post-glacial deposits within Permian strata documents the fast retreat of ice from depositional basins across Gondwanaland (Isbell et al., 2003). In Western Australia, India and Pakistan, the tillites of the Asselian and Early Sakmarian ages are overlain by Late Sakmarian and Artinskian strata containing cold-water faunas. This suggests that glaciation ended along the Tethyan coast of Gondwana in the late Early Permian, or near the end of the Artinskian at about 262 Ma (Isbell et al., 2003; López-Gamundí, 1997;

Veevers, 1994) compared to that on the polar side of Gondwana, where it lasted longer by about 10 Ma (Isbell et al., 2003; López-Gamundí, 1997; Veevers, 1994). Sedimentary rocks formed during this last major glacial event can be encountered in the Damodar, Son, Mahanadi and Godavari rift basins of India. The organic petrographic, elemental, organic carbon and $\delta^{13}\text{C}_{org}$ signatures of the deglacial sequences of the Lower Gondwanan Kommugudem Formation record the weathering pattern, provenance and depositional environment during the Early Permian. Anoxic preservation and enrichment of organic-rich sediments elucidate the palaeoclimatic controls on deglaciation events and the response of vegetation to changing temperature, sea level and paleoceanographic conditions.

Kommugudem shales exhibit high detrital silica, (39.03-72.23%; average= 58.39%), alumina (15.00-24.74%, ~19.86%) and iron oxide (0.24-12.02%; ~4.13%) content. SiO_2 enrichment relative to Al_2O_3 and CaO (Fig. 4.7) may likely be due to diagenetic alterations of these Lower Gondwana sediments with the formation of chlorite, quartz, kaolinite and other replacement reactions like forming of iron oxide, carbonates and illite. The secondary quartz generation occurs indicating drift of the Gondwanaland toward lower sub-equatorial latitudes from higher Southern latitudes (Dutta and Suttner, 1986).

The Al_2O_3 –($\text{CaO}+\text{Na}_2\text{O}$)– K_2O ternary diagram and $\text{Al}_2\text{O}_3/\text{TiO}_2$ ratio support the provenance of granites, gneisses, granodiorites and metasediments derived from the basement for the Kommugudem Formation. This concurs with the source rocks of its stratigraphic equivalent, the Barakar mudstones of the Damodar Valley Basin of Eastern Gondwana (Ghosh et al., 2019). The low chemical maturity index (CMI = 2.34 - 4.35) of Kommugudem shale samples suggests an abundance of detrital minerals near provenance without substantial recycling during sedimentation (Kala, Devaraju, Tiwari, et al., 2021). Nb and Th enrichment observed in Kommugudem samples also supports the probable detrital source of the quartz due to the insoluble nature, consequent diagenetic immobility and low seawater/continental crust distribution (Kala et al., 2021). The Barnett Shale Formation brittle zones majorly constitute biosiliceous allochems (a recrystallized

form of clay-sized micro quartz cement). This matrix dispersed clay-sized quartz cement significantly increased the brittleness of the Barnett Formation. Clay-sized microquartz cement identified in a few samples (Fig. 4.1b & c) may bind silt-size detrital quartz and increase brittleness by also enhancing intergranular pores preservation for cement precipitation (Peng et al., 2020). Illitization of smectite clay also leads to the development of recrystallized microquartz cement as confirmed by XRD semiquantitative results indicating the presence of illite and absence of smectite (Hall, 2019). The mineralogical-based brittleness index does not consider the form of minerals or the type of clay mineral associated (De et al., 2020; Hall, 2019). Thus, such calculations need to be utilized carefully.

Kommugudem samples have relatively high K_2O content due to illite-rich clay mineralogy. Lower K/Al and Mg/Al ratios (Table 4.3) in a few samples suggest the occurrence of kaolinite with minor concentrations of Mg and K (Ross & Bustin, 2009a). A similar trend is reported for the Barakar mudstones of the Raniganj Basin, which have relatively low K_2O/Al_2O_3 and ICV values and high CIA values (Ghosh et al., 2019). The presence of clays like illite and kaolinite are distinct geochemical parameters of the Kommugudem implying a transition in paleoclimate from cold, dry to warmer conditions (Suttner and Dutta, 1986). A semi-arid, hot climate (Fig. 7.1a) and post-glacial warming during the deposition of the Kommugudem Formation are demonstrated by the SiO_2 wt% versus $(Al_2O_3 + K_2O + Na_2O)$ wt% variations. The elemental “c” ratio $(Fe + Mn + Cr + V + Ni + Co)/(Ca + Mg + K + Na + Sr + Ba)$ indexes the paleoclimatic conditions where, higher ratio is for wetter climate and as the ratio decreases, the climate becomes more arid (X. Li et al., 2020). The average “c” of terrestrial mudstones in the Paleozoic is 1.02 with “c” ratio (0.30-1.26) of the Kommugudem Formation also validates a relatively warmer and humid climate (Miao et al., 2005). The Sr/Cu ratio ranges 0.91-4.09, where the ratio range of 1.3–5.0 indicate a humid and warm climate (J. Ding et al., 2018). Ga is predominately abundant in clay minerals, suggesting a humid and warm climate, whereas Rb is associated with illite, indicating a cold and dry climate (J. Ding et al., 2018). Generally, shales exhibit low Sr/Cu ratios and

high Ga/Rb ratios in humid and warm climate settings (J. Ding et al., 2018). Ga/Rb vs Sr/Cu plot indicates mainly humid-arid to humid-warm climatic conditions (Fig. 7.1b).

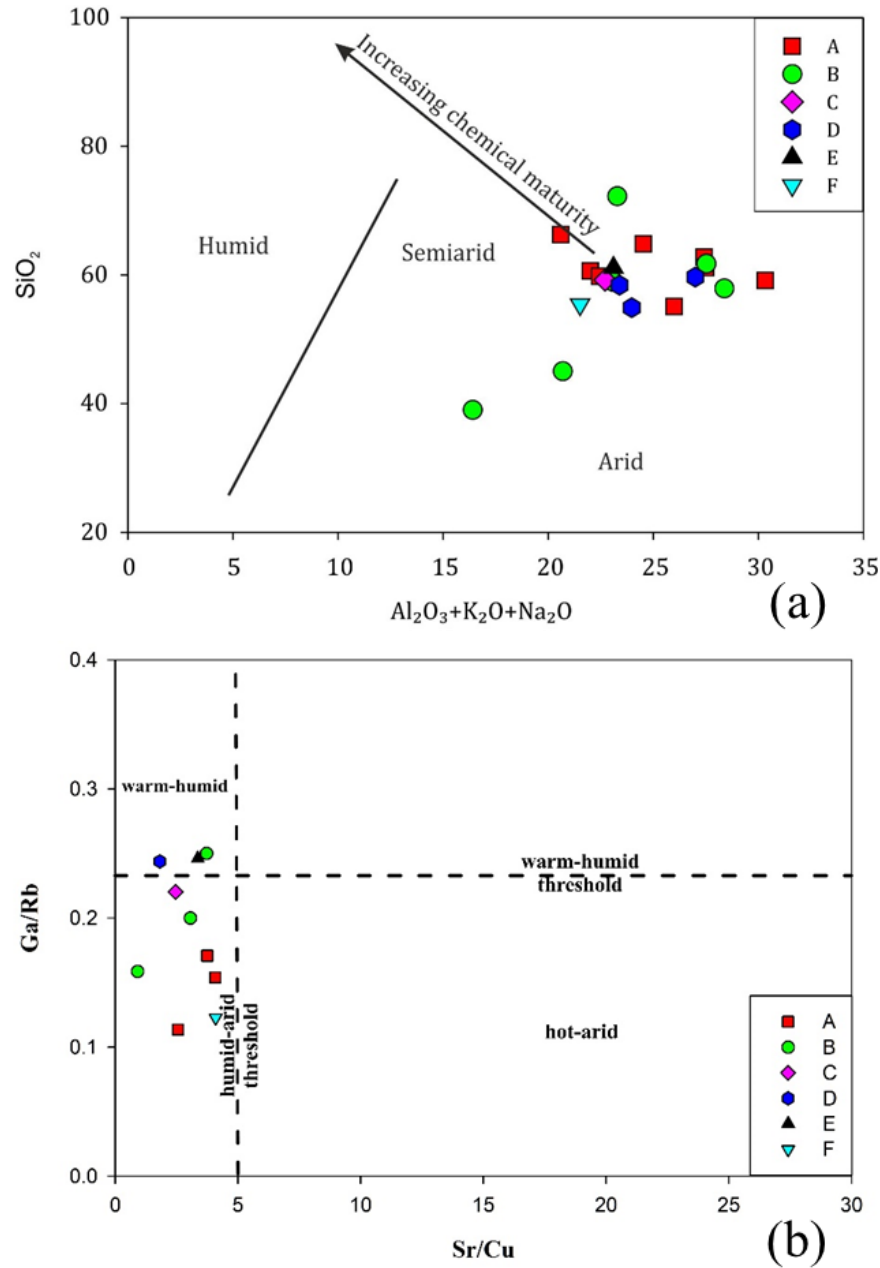


Fig. 7.1 (a) SiO₂ vs. Al₂O₃+K₂O+Na₂O plot of samples from Kommugudem Formation depicting paleoclimate conditions; (b) Sr/Cu vs. Ga/Rb cross plot depicting the paleoclimate conditions during the deposition of Kommugudem Formation (modified after J. Ding et al., 2018).

Aside from the signature of some marine ingressions in the bottom section, the whole Gondwana sequence is thought to be of fluvial origin (Veevers & Tewari, 1995). Barakar Formation got deposited post-Sakmarian marine transgression with the initiation of the fluvial environment in the margins of the basins, while the near-shore environment dominated interior zones of the Gondwana basins (Mukhopadhyay et al., 2010). Recent investigations have shown evidence of tidal and wave impacts on channel fill sediments in the upper portion of the Barakar succession, implying an open sea close to the peninsular Gondwanaland during the Barakar sedimentation (Bhattacharjee et al., 2018). A discriminatory diagram using K_2O/Al_2O_3 vs. MgO/Al_2O_3 ratios for Kommugudem shales suggests its marine nature (Fig. 7.2) and deposition in the passive continental margin (Fig. 4.7 & 4.9a). This is also corroborated by the redox-sensitive trace and rare earth elements, sedimentary biomarkers and stable carbon isotope compositions.

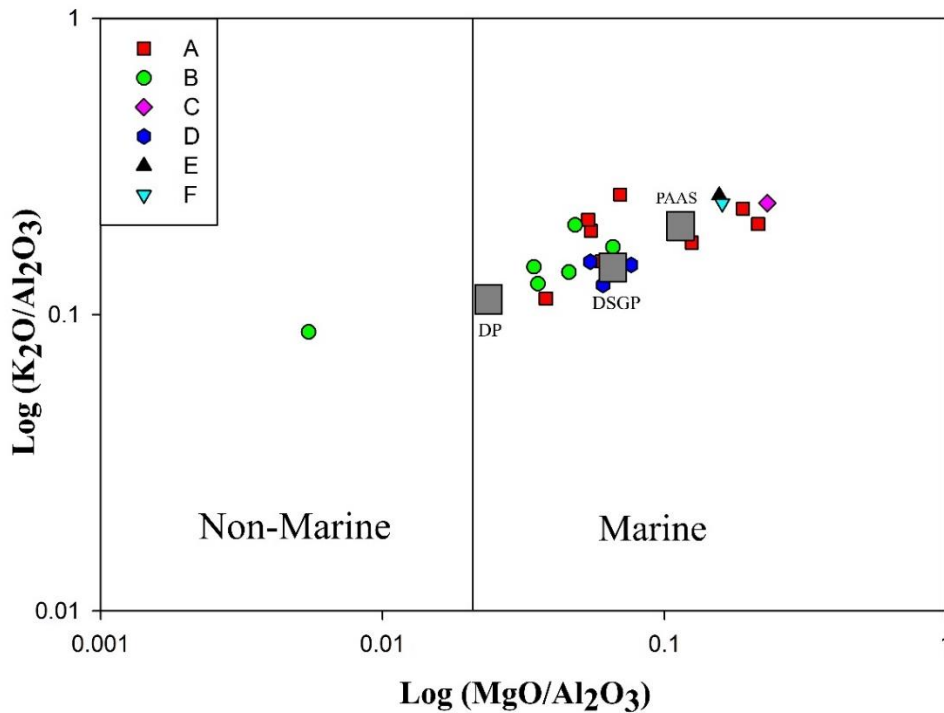


Fig. 7.2 Depositional setting of Kommugudem shales based on $\log(MgO/Al_2O_3)$ and $\log(K_2O/Al_2O_3)$ ratios. DP= Devonian marine pelites, DSGP= Devonian marine subgreywacke pelites and PAAS = Post Archaean Australian shales (modified after Roaldest, 1978).

The compositional and isotopic ratios of kerogen and biomarkers in Kommugudem record the paleo-depositional and preservational processes. The predominance of alkanes with n-C₁₆ to n-C₁₈ in the saturate fractions of lipid extract of Kommugudem shales (Fig. 5.7), suggests that these organic markers are derived from algal biomass, which contrasts sharply with terrestrial plant-lipids that maximize around n-C₂₉ in their n-alkane distribution. The abundance of aquatic algae and cyanobacteria is indicated by contributions from relatively high amounts of short and mid-chain alkanes, TAR, *Paq* and *Pwax* ratios (Table 5.3). Aromatic biomarkers provide vital information on organic matter input, thermal maturity and depositional environment. A distinct assemblage of biomarkers, DBT/P vs. Pr/Ph (Fig. 5.8b) in Kommugudem shales interprets a marine-lacustrine depositional environment, based on the environmental limitations on the organism from which these biomarkers originate.

7.3 Paleocyanography and organic productivity

The Gondwana sequence represents varied climatic settings and multiple sea level fluctuations during the sedimentation impact the redox conditions and transport of terrigenous components. Organic matter compositional and isotopic changes contribute to determining paleoclimate, paleosalinity, redox conditions, restricted or basin margin-near shore depositional settings and paleoproductivity. Thus, the elemental and organic enrichment is intricately linked to the depositional environment.

Organic matter enrichment is correlated with paleoproductivity using phosphorus content (X. Li et al., 2020). Kommugudem shales show high TOC with low P/Ti (0.01-0.33) and correspond to low paleoproductivity (Table 4.3; Algeo et al., 2011). P/Ti and P/Al show a weak negative correlation with TOC, indicating paleoproductivity in the ancient ocean was lower.

Biomarkers of Kommugudem shales elucidate the paleocyanographic conditions responsible for the deposition and preservation of organic-rich sediments. Phytane is dominantly present with the Pr/Ph ratios being less than unity for all the shales

except two samples of Well A and C ($\text{Pr/Ph} > 1$), suggesting anoxia in the basin (Table 5.3). The abundance of organic sulfur in the sediments (Table 4.2) suggests the possibility of the development of euxinic conditions. The last glacial advance and subsequent deglaciation in the late Early Permian, in various parts of eastern and southern African (Karoo) basins, resulted in the emergence of enormous euxinic lakes with a high organic matter concentration (López-Gamundí & Buatois, 2010; Montañez & Poulsen, 2013). Elemental sulfur content from major oxide data (Table 4.2) ranges between 0.05 to 0.95 wt % for the Kommugudem shales. The presence of high organic sulfur has also been reported in the Lower Gondwana formations of Wardha valley (Pophare et al., 2017), which is a part of the Pranhita-Godavari Basin. The pyritic and organic sulfur contribution assessed by elemental and mineralogical proxies of Kommugudem shales supports the organic matter deposition and enhanced preservation dominantly in an anoxic (or probably euxinic) setting.

Excess Si concentrations, as witnessed in Kommugudem shales, can be utilised as a proxy for paleoproductivity in reducing sediments. Certain paleoceanographic conditions are unfavourable for organic matter, which obstruct the nutrient input, causing low ancient productivity (Algeo et al., 2011). The high organic content of Kommugudem shales and the abundances of redox-sensitive trace elements support a favourable preservational environment, leading to the deposition of organic-rich source rocks. A reducing marine environment of deposition can be envisaged during the Early Permian, where shallow seaways penetrated farther into the continental interior and narrow deep seas were present as tectonic plates were still converging (Nairn & Smithwick, 1976).

The presence of Leiosphaerids in the Palar Basin of Mysore, as well as the southeastern part of the Athgarh and Pranhita-Godavari basins, suggests a possible marine incursion between Antarctica and India from the northern (Tethyan) margin via marine equivalents in the western Australian basins (Veevers & Tewari, 1995). Sastri et al., (1981) observed the presence of marine Permian sediments on the eastern coast of India and postulated a thick marine Paleozoic sequence in offshore,

which fits with the regional palaeogeography of northwest Australia. During Kommugudem sedimentation, possible marine inundation resulted in floods and the formation of a fluvial–marine depositional system (Fig. 7.3a).

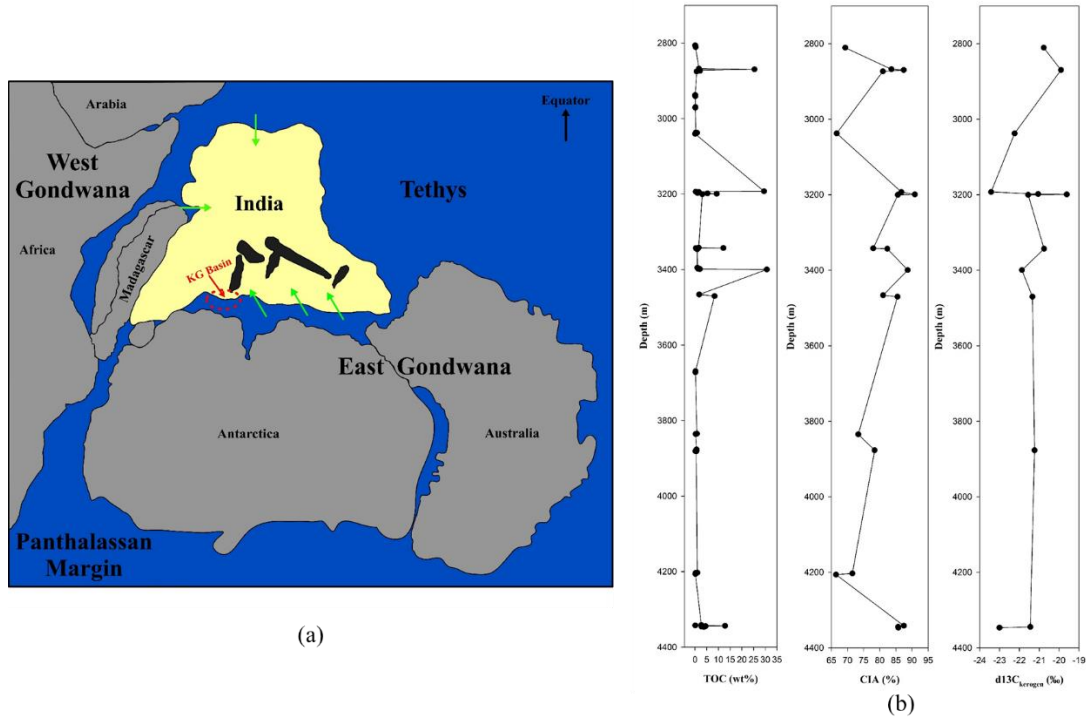


Fig. 7.3 (a) Gondwana continental assemblage during Early Permian showing possible marine incursion pathways (indicated by green arrows) in KG Basin; (b) Variation of TOC, CIA and $\delta^{13}C_{org}$ in Kommugudem shales of KG Basin.

Organic matter originating primarily from marine production contains the $\delta^{13}C$ signature of atmospheric CO_2 , revealing the variations in glacial and interglacial pCO_2 values (Jasper & Hayes, 1990). The full glacial environment is marked by more negative $\delta^{13}C_{org}$ values, whereas less negative $\delta^{13}C_{org}$ values categorise interstadial phases (Jasper & Hayes, 1990). The $\delta^{13}C_{org}$ values for Kommugudem shales range between -19.62 to -23.43‰ with an average of -21.55‰. The variation of $\delta^{13}C_{org}$, TOC and CIA is shown in Fig. 7.3b. An increase in atmospheric pCO_2 from Early Permian to Late Permian is supported by increased continental temperatures and aridity. Factors such as primary productivity, organic burial on land and in the oceans and silicate weathering-consumption of CO_2 are intricately

linked with observed shifts in the ^{13}C ratios. The negative shift from the enriched values of $\delta^{13}\text{C}_{\text{Org}}$ in Kommugudem shales represents relatively strong weathering conditions with the reduced marine organic matter input. In this scenario, the ocean water would no longer be depleted in ^{12}C and the organic matter burial would thus lead to a more negative ^{13}C . This is also supported by the P/Al ratios, clay minerals and weathering indices indicating increased terrestrial contribution, with relatively depleted ^{13}C observed in coaly textured shales. Carbon and sulfur linkages during the Permian were controlled by the redox conditions and high pyritic sulfur with less negative $\delta^{13}\text{C}_{\text{Org}}$ has been reported (Zhou et al., 2017). Early Permian marine isotope records from the Karoo Basin, South Africa show the low $\delta^{13}\text{C}$ values representing glacial conditions, whereas higher $\delta^{13}\text{C}$ values (-25‰ to -22‰) suggest deglaciation (Scheffler et al., 2003). The Eccia Group deposited during the earliest Asselian, has reported the most elevated $\delta^{13}\text{C}_{\text{Org}}$ values (average $\delta^{13}\text{C}$ of -22.25‰) indicating the atmospheric $p\text{CO}_2$ variations (Scheffler et al., 2003).

The sedimentary Ti/Al molar ratios have been used as a proxy to understand sea-level changes, specifically from a semi-closed basin off a marginal sea. Ti/Al molar ratios are higher for glacial periods and lower for interglacial periods (Waelbroeck et al., 2002). Ti/Al ratios are low for the Kommugudem shales and correspond to changes in sea level of interglacial periods. Biostratigraphy and facies correlation of Early Permian within the Gondwanan basins suggest that deglaciation took place in the late Asselian or early Sakmarian (Crowell, 1995; Eyles, 1993; Eyles et al., 2002; Isbell et al., 2003; Stephenson & Osterloff, 2002). Ice sheets were possibly existent in Gondwana during the last Glacial event (Stephanian to Sakmarian) (Stephenson et al., 2005; Veevers & Powell, 1987) with the waxing and waning of the massive ice sheets and the subsequent sea-level fluctuations (Wopfner, 1999; Wopfner & Kreuser, 1986) producing the base level changes noted by Artinskian Kommugudem cyclothems.

7.4 Mineral assemblage and their influence on pore structure parameters

Substantially more than 50% of the gas in place is stored in matrix porosity. The Shale matrix also impacts well productivity by influencing the mobility of gas (Bowker, 2007; Chalmers, Ross, et al., 2012). Therefore, it is essential to determine inorganic/organic matter and associated pores in the matrix that controls the sorbed gas. Shale reservoirs have complex pore structures and multiscale fabric that can be linked to the microstructure of mineral and organic matter (Kuila & Prasad, 2013). Diagenetic processes cause a major loss in primary porosity (inter-and intracrystalline pores) and further reduction occurs due to infilling by ductile secondary organic matter (Loucks et al., 2012; Milliken et al., 2012). Mineral matter is the main host for primary pores while organic matter constitutes primary pores only in trace amounts (Loucks et al., 2012; Milliken et al., 2012). The preservation of primary pores largely relies on rigid grains that shelter pores from compaction (Loucks et al., 2012; Milliken et al., 2012; Song & Carr, 2020). Mechanically competent grains (quartz, feldspar, dolomite, pyrite, etc.) may form compaction-resistant pressure shadows, aiding the preservation of pore space between clays (Schieber, 2013). As maturity increases, organic matter fills these primary pores in the mineral framework, thus decreasing porosity unless organic matter starts hydrocarbon generation. These filled primary porosity and the nano-porous secondary organic matter may be inter-connected (Loucks et al., 2012; Milliken et al., 2012). As per the XRD results, Kommugudem shales have considerably higher quartz content (40.77 – 82.92%). However, it has been observed that the possibility of primary pores in quartz is limited as it exhibits weak positive correlations with pore volume and BET-SSA.

Pyrite framboids can host isolated intracrystalline pores, or be loosely clustered to form porosity connected to the whole pore-system, as can be observed in FE-SEM images (Fig. 4.4e & f). Intracrystalline pyrite pores are either primary or diagenetic in origin (Loucks et al., 2009, 2012; Milliken et al., 2012). The organic matter filling intracrystalline pores is favourable for hydrocarbon migration. Heavier hydrocarbon remains in the pores causing pore space loss during the migration

process and residuals from migration can also generate micropores (Shao et al., 2017; R. Yang et al., 2016).

The clay pore structures are a function of the degree of chemical maturity and diagenesis of the shale rock (Ross & Bustin, 2009b). Clay minerals possess catalytic cracking potential and influence kerogen to form lighter hydrocarbons (Tannenbaum et al., 1986). As per XRD and FE-SEM results, Kommugudem samples possess Kaolinite, chlorite and illite clays ranging between 3.28 - 23.57% (Table 4.1; Fig. 4.4). It was observed that there is a positive relationship between micropore volume and clay content ($R^2= 0.79$) which indicates a higher contribution of clay content toward micropores.

Pore volume and BET - SSA indicates the storage capacity of free gas and adsorbed gas respectively (Song & Carr, 2020). BET-SSA and total PV show a strong positive correlation ($R^2= 0.98$) as shales with a smaller average pore size tend to have a larger pore volume and specific surface area (Shao et al., 2017). Similar correlations are observed from North American prolific shale reservoirs of Barnett, Marcellus, Haynesville, Woodford and Doig Phosphate shales (Chalmers, Bustin, et al., 2012).

7.5 Source rock characterization and its influence on pore structure parameters

Pore-size distribution and tortuosity of the pore system are functions of mineral content, organic matter, degree of anisotropy and texture of shale reservoirs (Chalmers, Bustin, et al., 2012; Chalmers, Ross, et al., 2012). It is essential to comprehend the relationship of TOC and Tmax with micropore volume and BET-SSA, as microporosity associated with the organic matter controls methane sorption (Chalmers & Bustin, 2007; Ross & Bustin, 2009b). The shale samples exhibit a positive correlation between micropore volume and Tmax ($R^2= 0.94$), which is supported by previous studies (M. E. Curtis et al., 2012; Ross & Bustin, 2009b). TOC and micropore volume, of the selected shales, show a positive correlation ($R^2= 0.62$), which may be due to more contribution of clay micropore and associated

organic matter. The ratio of methane adsorption capacity to TOC is higher for mature shales, thus inferring that the micropore volume increases during maturation due to organic matter breakdown, which increases available sorption sites. (Chalmers & Bustin, 2007; Jarvie et al., 2007; Ross & Bustin, 2009b; Zou & Rezaee, 2019). Organic matter constitutes relatively higher volumes of micropores than the mineral component of the shale reservoir (Loucks et al., 2009). Micropores in the organic matter increase with thermal maturity and organic matter density decrease when hydrocarbons are generated (Jarvie et al., 2007; Modica & Lapiere, 2012; F. P. Wang & Gale, 2009). Therefore, thermally mature, TOC-rich Kommugudem shale may have larger micropore volumes and SSA resulting in higher adsorption capacities (Ji et al., 2012; Kim et al., 2017). Prior investigations based on FE-SEM infer that conventional and shale reservoirs are distinctly different due to the presence of intracrystalline organic matter pores (Fig. 4.4b) in shale reservoirs as also observed in Kommugudem samples (Loucks et al., 2009, 2012; Milliken et al., 2012). The organic matter porosity is a complex function of mineral matter, origin and abundance of organic matter, depositional setting, thermal history and compaction history (Schieber, 2013). Organopores generated are either relatively large discrete pores in a single kerogen piece or a sponge-like network of organic matter-hosted pores (Song & Carr, 2020). Kommugudem Formation mainly exhibits intracrystalline organic matter pores with a sponge-like network formed during hydrocarbon generation on multiple sites in kerogen (Fig. 4.4b).

7.6 Thermal maturity effect on trace element enrichment

Thermal maturation could support trace elemental enrichment by causing organic matter conversion to hydrocarbons and generating more ordered macromolecules by increasing organic matter aromaticity (Hackley & Lewan, 2018; Khatibi et al., 2018). But thermal maturation (based on Tmax and VRo) exhibits no to very low effect upon the redox-sensitive elements distributed in the present study. Molybdenum (Mo) exhibits a slight positive correlation with Tmax ($R^2= 0.24$). Mo

enrichment in sediment was also observed where, reducing environment in a stagnant, deep-water environment can lead to the formation of hydrogen sulfide. Pyrite concentration is observed in a few samples, supported by XRD and FE-SEM results and may take Mo from solution at the sediment-water interface or water column (Abarghani et al., 2020; Algeo & Maynard, 2004; Worden et al., 1995). Higher thermal maturity aids the concentration of thermogenic H₂S, resulting in higher sulfur release from organic matter and Mo enrichment (Abarghani et al., 2020).

The redox-sensitive elements may get introduced in sediment with organic matter association under anoxic water-column conditions (Ross & Bustin, 2009a). Pb, Zn and U exhibit a positive correlation ($R^2 = 0.57, 0.46$ and 0.41 respectively), while other redox-sensitive elements show low or no relationship with TOC. The organic-rich sediments are considered the largest sink for Uranium dissolved in marine water where U diffuses into reducing sediments readily by acting conservatively in oxic waters (Breit & Wanty, 1991; Bruland, 1983). Zn could be released from organic matter through sulfate-reducing bacterial activity. Similar to Mo, Pb can also be in solid solution by authigenic pyrite formation in the water column (Algeo & Maynard, 2004). Thermal maturity can aid Zn and Pb enrichment by the formation of more authigenic Fe-sulfides, but no correlation is observed. The poor correlation of trace elements with T_{max} and TOC may be resultant of a statistically low number of samples (Abarghani et al., 2020).

7.7 Paleoenvironmental indices and their influence on pore parameters

The marine environment induces the genesis of brittle minerals like biogenic quartz, carbonate minerals and pyrite, while the continental environment forms more ductile clay minerals (Yu et al., 2020). Kommugudem Formation exhibits a fluvio-marine transitional environment with a major presence of silicates indicating the dominant role of the marine environment with the minor terrigenous influx. The REEs exhibit negligible mobility and resist fractionation due to weathering processes in the surficial environments, thus providing useful insight into the paleoenvironment (Henderson, 1984). The REE exhibit a positive albeit weak

relationship with quartz suggesting accumulation of detrital sourced quartz due to terrigenous influx (Henderson, 1984). The REEs are positively correlated with SSA and micropore volume indicating the possible role of REEs in the pore genesis of silicate minerals ($R^2= 0.55$ & 0.65 respectively). Cr concentrations are also a function of detrital content and correlate positively with SSA and total PV ($R^2= 0.56$ & 0.67 respectively). Thus, REEs coupled with Cr indicate their probable role in the pore genesis of detrital quartz. Ni, V, U, Cu and Zn are sequestered by organic matter in reducing sediments with U and Zn exhibiting a positive correlation with TOC and micropore volume ($R^2= 0.53$ & 0.65 respectively) (Algeo & Maynard, 2004; Breit & Wanty, 1991). Ni, V and Cu also demonstrate positive correlation with micropore ($R^2= 0.25, 0.36$ & 0.57 respectively) and total pore volume ($R^2= 0.81, 0.40$ & 0.51 respectively). Such correlations are suggestive of the influence of redox-sensitive elements on pore genesis in organic matter.

The redox proxies for Kommugudem Formation are indicative of a transitional environment that was preserved under suboxic to oxic conditions. Redox proxy U/Th indicates suboxic to oxic conditions and exhibits a strong positive correlation with TOC and total PV ($R^2= 0.75$ & 0.61 respectively). Similarly Ni/Co redox proxy exhibits a positive correlation with SSA and micropore volume ($R^2= 0.91$ & 0.94 respectively). Mo/TOC redox proxy also indicates a positive correlation with SSA and total PV ($R^2= 0.77$ & 0.84 respectively). The possibility of the development of organopores is supported by stated correlations and FE-SEM imagery.

The paleoclimate and paleosalinity proxy do not exhibit significant relationships with pore parameters. Sr/ Cu is a paleoclimate proxy indicating a warm and humid climate with clay enrichment and a moderately strong positive correlation with total PV ($R^2= 0.40$). The Rb/K ratio is a paleosalinity indicator indicating fresh to brackish water column and exhibits a very weak positive correlation with micropore volume ($R^2= 0.05$). Stated inferences indicate the possible impact of paleoenvironmental indices on mineral and organic matter associated with pore

genesis. But further studies are required to substantiate the stated results with more extensive data over a wider range of geologic formations.

CHAPTER 8: CONCLUSIONS

8.1 Conclusions

The multiproxy petrographic and geochemical analysis with the correlation of pore characteristics of samples from the Kommugudem Formation led to the following major inferences.

- Macroscopic and petrographic examinations indicate an overall silica-rich lithology with carbonaceous shale, silty carbonaceous shale, silty shale and fine-grained micaceous sandstone facies.
- XRD analyses showed that the formation is predominantly siliceous, with a silica-dominated lithotype and clay-rich siliceous mudstone. Variable techniques determined a high mineralogical brittleness index in the Kommugudem Formation, demonstrating favourable conditions for hydraulic fracturing.
- FE-SEM examinations revealed the presence of microfractures and micropores in the form of inter and intragranular pore sites in mineral and organic matter, which might serve as hydrocarbon storage sites. The existence of natural microfractures in Kommugudem may improve hydraulic fracturing performance by providing a hydrocarbon migration channel.
- As per the elemental analysis, detrital sediments are mostly derived from felsic volcanic rocks along the passive tectonic continental margin. The redox and paleosaline proxies point to a fluvio-marine transitional environment preserved under suboxic to oxic conditions.
- The variation of $\delta^{13}\text{C}_{\text{Org}}$, TOC and CIA values support a climatic change from cold, dry to warming post-glacial conditions during the Upper Early Permian.
- The RockEval pyrolysis assessment confirmed the existence of primarily Type III kerogen in admixture with Type II-III and Type IV with high TOC and

T_{max}, implying the presence of substantial organic matter in the dry and wet gas windows. The vitrinite reflectance measurements also indicated that mature to post-mature Kommugudem shale is predominant in the gas generation window.

- The RockEval parametric and FTIR findings indicate that Wells A and B have excellent hydrocarbon generation potential for oil and gas, however, Wells C, D, E and F have lesser potential and may yield poor sources for gas and oil.
- The adsorption-desorption hysteresis loop indicates the presence of complex slit and cylindrical pores. Fractal dimensions vary between 2 and 3 suggesting that the samples exhibit complex and heterogeneous pore structures. Pore morphology as observed by FE-SEM imagery supports these findings.
- The contribution of clay micropores and related organic matter is substantial, with quartz playing a minor role. The poor correlation of trace elements with T_{max} and TOC was detected, which might be attributed to the statistically small number of samples.
- The REEs and Cr are likely to have a role in the pore genesis of silicate minerals, emphasizing the need of understanding sedimentary environmental processes. The redox proxies are strongly correlated with TOC and total PV, indicating the potential formation of organopores, which is corroborated by FE-SEM images.
- Multiproxy investigations revealed Wells A and B have good hydrocarbon potential, abundant brittle minerals with micropore and microfracture occurrence in carbonaceous and silty shales. Thus, Kommugudem Formation can be promising for gas shale exploration as well as future carbon storage sites.

8.2 Future scope

The present study focuses primarily on the shale composition (organic and inorganic), paleoenvironment indices and their complex mechanisms with their possible influence on pore characteristics. However, further studies are required as mentioned below. The following issues are identified as future scope of research:

1. Identification of microquartz and their diagenetic control using SEM-CL for greater understanding of the role of quartz on shale brittleness.
2. Extensive analysis is required to understand pore morphology and connectivity at the nanoscale by varying techniques like NMR, micro-CT, etc.
3. Detailed adsorption-permeability studies of shales are required for upscaling the gas flow mechanism.
4. Investigations are required with more extensive data to demonstrate better insight into paleoenvironmental influence on pore genesis.

REFERENCES

- Abarghani, A., Gentzis, T., Liu, B., Khatibi, S., Bubach, B., & Ostadhassan, M. (2020). Preliminary investigation of the effects of thermal maturity on redox-sensitive trace metal concentration in the Bakken source rock, North Dakota, USA. *ACS Omega*, 5(13), 7135–7148.
- Abarghani, A., Ostadhassan, M., Gentzis, T., Carvajal-Ortiz, H., & Bubach, B. (2018). Organofacies study of the Bakken source rock in North Dakota, USA, based on organic petrology and geochemistry. *International Journal of Coal Geology*, 188, 79–93.
- Abouelresh, M., Babalola, L., Al-Ghamdi, T., Al-Abdullatif, A., & El Hajj, H. (2016). Sequential Mineralogy Characterization of Organic-Rich Shale: Example from the Hanadir Shale, Northwest Saudi Arabia. *SPE Kingdom of Saudi Arabia Annual Technical Symposium and Exhibition, Dammam, Saudi Arabia*.
- Algeo, T. J., Kuwahara, K., Sano, H., Bates, S., Lyons, T., Elswick, E., Hinnov, L., Ellwood, B., Moser, J., & Maynard, J. B. (2011). Spatial variation in sediment fluxes, redox conditions, and productivity in the Permian–Triassic Panthalassic Ocean. *Palaeogeography, Palaeoclimatology, Palaeoecology*, 308(1–2), 65–83.
- Algeo, T. J., & Maynard, J. B. (2004). Trace-element behavior and redox facies in core shales of Upper Pennsylvanian Kansas-type cyclothems. *Chemical Geology*, 206(3–4), 289–318.
- Algeo, T. J., & Rowe, H. (2012). Paleooceanographic applications of trace-metal concentration data. *Chemical Geology*, 324, 6–18.
- Allix, P., Bumham, A., Fowler, T., Herron, M., Kleinberg, R., & Symington, B. (2010). Coaxing oil from shale. *Oilfield Review*, 22(4), 4–15.
- Altindag, R. (2003). Correlation of specific energy with rock brittleness concepts on rock cutting. *Journal of The South African Institute of Mining and Metallurgy*, 103(3), 163–171.
- Alzahabi, A., Al Qahtani, G., Soliman, M. Y., Bateman, R. M., Asquith, G., & Vadapalli, R. (2015). Fracturability index is a mineralogical index: A new approach for fracturing decision. *Society of Petroleum Engineers - SPE Saudi Arabia Section Annual Technical Symposium and Exhibition*, 1–32. <https://doi.org/10.2118/178033-ms>

- Arens, N. C., & Jahren, A. H. (2000). Carbon isotope excursion in atmospheric CO₂ at the Cretaceous-Tertiary boundary: evidence from terrestrial sediments. *Palaios*, *15*(4), 314–322.
- Bakshi, T., Prusty, B. K., Pathak, K., Nayak, B. R., Mani, D., & Pal, S. K. (2017). Source rock characteristics and pore characterization of Indian shale. *Journal of Natural Gas Science and Engineering*, *45*, 761–770.
<https://doi.org/10.1016/j.jngse.2017.06.010>
- Bakshi, T., Prusty, B. K., Pathak, K., & Pal, S. K. (2018). Pore characteristics of Damodar valley shale and their effect on gas storage potential. *Journal of Petroleum Science and Engineering*, *725–735*.
<https://doi.org/10.1016/j.petrol.2017.10.091>
- Bakshi, T., Vishal, V., Prusty, B. K., & Pathak, K. (2020). Carbon dioxide and methane sorption characteristics of Damodar Valley and Upper Assam shale, India. *Energy and Climate Change*, *1*, 100002.
<https://doi.org/https://doi.org/10.1016/j.egycc.2020.100002>
- Behar, F., Beaumont, V., & Penteado, H. L. D. B. (2001). Rock-Eval 6 technology: performances and developments. *Oil & Gas Science and Technology*, *56*(2), 111–134.
- Behar, F., Kressmann, S., Rudkiewicz, J. L., & Vandenbroucke, M. (1992). Experimental simulation in a confined system and kinetic modelling of kerogen and oil cracking. *Organic Geochemistry*, *19*(1–3), 173–189.
- Behar, F., & Vandenbroucke, M. (1987). Chemical modelling of kerogens. *Organic Geochemistry*, *11*(1), 15–24.
[https://doi.org/https://doi.org/10.1016/0146-6380\(87\)90047-7](https://doi.org/https://doi.org/10.1016/0146-6380(87)90047-7)
- Bernard, S., Wirth, R., Schreiber, A., Bowen, L., Aplin, A. C., Mathia, E. J., Schulz, H.-M., Horsfield, B., Aplin, A., & Mathia, E. (2013). FIB-SEM and TEM investigations of an organic-rich shale maturation series from the lower Toarcian Posidonia Shale, Germany: Nanoscale pore system and fluid-rock interactions. *Electron Microscopy of Shale Hydrocarbon Reservoirs: AAPG Memoir*, *102*, 53–66.
- Berner, R. A. (1990). Atmospheric carbon dioxide levels over Phanerozoic time. *Science*, *249*(4975), 1382–1386.
- Bhatia, M. R., & Crook, K. A. W. (1986). Trace element characteristics of graywackes and tectonic setting discrimination of sedimentary basins. *Contributions to Mineralogy and Petrology*, *92*(2), 181–193.
<https://doi.org/10.1007/BF00375292>
- Bhattacharjee, J., Ghosh, K. K., & Bhattacharya, B. (2018). Petrography and geochemistry of sandstone–mudstone from Barakar formation (early Permian), Raniganj Basin, India: Implications for provenance, weathering and marine depositional conditions during lower Gondwana sedimentation.

- Geological Journal*, 53(3), 1102–1122.
<https://doi.org/https://doi.org/10.1002/gj.2946>
- Bihani, A., Daigle, H., Santos, J. E., Landry, C., Prodanović, M., & Milliken, K. (2022). MudrockNet: Semantic segmentation of mudrock SEM images through deep learning. *Computers & Geosciences*, 158, 104952.
<https://doi.org/https://doi.org/10.1016/j.cageo.2021.104952>
- Biswas, S., Varma, A. K., Kumar, M., Mani, D., Saxena, V. K., & Mishra, V. (2020). Influence of geochemical, organo-petrographical and palynofacies assemblages on hydrocarbon generation: A study from upper Oligocene coal and shale of the Makum Coal Basin, Assam, India. *Marine and Petroleum Geology*, 114, 104206.
<https://doi.org/https://doi.org/10.1016/j.marpetgeo.2019.104206>
- Boggs, S. (2001). Sedimentary structures. In *Principles of sedimentology and stratigraphy* (3rd ed., pp. 88–130). Pearson.
- Bowker, K. A. (2007). Barnett Shale gas production, Fort Worth Basin: Issues and discussion. *American Association of Petroleum Geologists Bulletin*, 91(4), 523–533. <https://doi.org/10.1306/06190606018>
- Breit, G. N., & Wanty, R. B. (1991). Vanadium accumulation in carbonaceous rocks: a review of geochemical controls during deposition and diagenesis. *Chemical Geology*, 91(2), 83–97.
- Britt, L. K., Schoeffler, J., & Rock, B. (2009). SPE 125525 The Geomechanics Of A Shale Play: What Makes A Shale Prospective! *SPE Eastern Regional Meeting*, 23–25.
- Bruland, K. W. (1983). Trace elements in seawater. In J. P. Riley & R. Chester (Eds.), *Chemical Oceanography* (pp. 157–220). Academic Press.
- Brumsack, H. J., & Gieskes, J. M. (1983). Interstitial water trace-metal chemistry of laminated sediments from the Gulf of California, Mexico. *Marine Chemistry*, 14(1), 89–106.
- Brunauer, S., Emmett, P. H., & Teller, E. (1938). Adsorption of gases in multimolecular layers. *Journal of the American Chemical Society*, 60(2), 309–319.
- Campbell, F. A., & Williams, G. D. (1965). Chemical composition of shales of Mannville group (lower Cretaceous) of central Alberta, Canada. *AAPG Bulletin*, 49(1), 81–87.
- Carvajal-Ortiz, H., & Gentzis, T. (2015). Critical considerations when assessing hydrocarbon plays using Rock-Eval pyrolysis and organic petrology data: Data quality revisited. *International Journal of Coal Geology*, 152, 113–122.
- Casshyap, S. M., Tewari, R. C., Chandra, R., & Sri, T. (1988). Depositional

- model and tectonic evolution of Gondwana basins. *Palaeobotanist*, 36(December), 59–66.
- Chalmers, G. R., & Bustin, R. M. (2007). *The organic matter distribution and methane capacity of the Lower Cretaceous strata of Northeastern British Columbia, Canada*. 70, 223–239. <https://doi.org/10.1016/j.coal.2006.05.001>
- Chalmers, G. R., Bustin, R. M., & Power, I. M. (2012). Characterization of gas shale pore systems by porosimetry, pycnometry, surface area, and field emission scanning electron microscopy/transmission electron microscopy image analyses: Examples from the Barnett, Woodford, Haynesville, Marcellus, and Doig uni. *AAPG Bulletin*, 96(6), 1099–1119.
- Chalmers, G. R., Ross, D. J. K., & Bustin, R. M. (2012). Geological controls on matrix permeability of Devonian Gas Shales in the Horn River and Liard basins, northeastern British Columbia, Canada. *International Journal of Coal Geology*, 103, 120–131. <https://doi.org/10.1016/j.coal.2012.05.006>
- Chandra, D., & Vishal, V. (2021). A critical review on pore to continuum scale imaging techniques for enhanced shale gas recovery. *Earth-Science Reviews*, 217, 103638.
- Chandra, D., Vishal, V., Bahadur, J., Agrawal, A. K., Das, A., Hazra, B., & Sen, D. (2022). Nano-scale physicochemical attributes and their impact on pore heterogeneity in shale. *Fuel*, 314, 123070. <https://doi.org/https://doi.org/10.1016/j.fuel.2021.123070>
- Chen, F., Shuangfang, L. U., & Ding, X. (2018). Pore Types and Quantitative Evaluation of Pore Volumes in the Longmaxi Formation Shale of Southeast Chongqing, China. *Acta Geologica Sinica*, 92(1), 342–353. <https://doi.org/10.1111/1755-6724.13509>
- Chen, Y., Zou, C., Mastalerz, M., Hu, S., Gasaway, C., & Tao, X. (2015). Applications of micro-fourier transform infrared spectroscopy (FTIR) in the geological sciences—A Review. *International Journal of Molecular Sciences*, 16(12), 30223–30250. <https://doi.org/10.3390/ijms161226227>
- Clarkson, C. R., & Haghshenas, B. (2013). Modeling of supercritical fluid adsorption on organic-rich shales and coal. *SPE Unconventional Resources Conference-USA*.
- Cox, R., Lowe, D. R., & Cullers, R. L. (1995). The influence of sediment recycling and basement composition on evolution of mudrock chemistry in the southwestern United States. *Geochimica et Cosmochimica Acta*, 59(14), 2919–2940.
- Crowell, J. C. (1995). The ending of the late Paleozoic ice age during the Permian Period. In *The Permian of Northern Pangea* (pp. 62–74). Springer.
- Cui, X., Bustin, A. M. M., & Bustin, R. M. (2009). *Measurements of gas*

- permeability and diffusivity of tight reservoir rocks : different approaches and their applications*. 208–223. <https://doi.org/10.1111/j.1468-8123.2009.00244.x>
- Cullers, R. L., & Podkovyrov, V. N. (2000). Geochemistry of the Mesoproterozoic Lakhanda shales in southeastern Yakutia, Russia: implications for mineralogical and provenance control, and recycling. *Precambrian Research*, 104(1–2), 77–93.
- Curtis, J. B. (2002). Fractured Shale-Gas Systems. *AAPG Bulletin*, 86(11), 1921–1938. <https://doi.org/10.1306/61EEDDBE-173E-11D7-8645000102C1865D>
- Curtis, M. E. (2010). Structural characterization of gas shales on the micro-and nano-scales. *Canadian Unconventional Resources and International Petroleum Conference*.
- Curtis, M. E., Cardott, B. J., Sondergeld, C. H., & Rai, C. S. (2012). Development of organic porosity in the Woodford Shale with increasing thermal maturity. *International Journal of Coal Geology*, 103, 26–31. <https://doi.org/10.1016/j.coal.2012.08.004>
- Curtis, M. E., Sondergeld, C. H., Rai, C. S., & Engineering, G. (2013). Relationship Between Organic Shale Microstructure and Hydrocarbon Generation. *Spe 164540*, 1–7. <https://doi.org/10.2118/164540-MS>
- Davletshin, A., Ko, L. T., Milliken, K., Periwai, P., Wang, C. C., & Song, W. (2020). Object Detection in SEM Images Using Convolutional Neural Networks: Application on Pyrite Framboid Size-Distribution in Fine-Grained Sediments. *AGU Fall Meeting Abstracts, 2020*, IN028-07. <https://ui.adsabs.harvard.edu/abs/2020AGUFMIN028..07D>
- Dayal, A. M., Mani, D., Madhavi, T., Kavitha, S., Kalpana, M. S., Patil, D. J., & Sharma, M. (2014). Organic geochemistry of the Vindhyan sediments: implications for hydrocarbons. *Journal of Asian Earth Sciences*, 91, 329–338.
- De, S., Aastha, & Sengupta, D. (2020). Depositional environment and geomechanical properties of Cambay Shale: potential reservoir for shale oil and gas in India. *Arabian Journal of Geosciences*, 13(12), 455. <https://doi.org/10.1007/s12517-020-05462-z>
- Dembicki, H. (2009). Three common source rock evaluation errors made by geologists during prospect or play appraisals. *AAPG Bulletin*, 93(3), 341–356.
- Deng, H. W., & Qian, K. (1993). Sedimentary geochemistry and environmental analysis. *Gansu Science and Technology Press, Lanzhou*, 18–31.
- DGH. (2012). Directorate General of Hydrocarbons. *Retrieved from Wwww. Dghindia.Org*.

- Ding, J., Zhang, J., Tang, X., Huo, Z., Han, S., Lang, Y., Zheng, Y., Li, X., & Liu, T. (2018). Elemental geochemical evidence for depositional conditions and organic matter enrichment of black rock series strata in an inter-platform basin: The lower carboniferous datang formation, Southern Guizhou, Southwest China. *Minerals*, 8(11), 509. <https://doi.org/10.3390/min8110509>
- Ding, W., Li, C., Li, C., Xu, C., Jiu, K., & Zeng, W. (2012). Fracture development in shale and its relationship to gas accumulation. *Geoscience Frontiers*, 3(1), 97–105. <https://doi.org/10.1016/j.gsf.2011.10.001>
- Dutta, P. K., & Suttner, L. J. (1986). Alluvial sandstone composition and paleoclimate; II, Authigenic mineralogy. *Journal of Sedimentary Research*, 56(3), 346–358.
- Dypvik, H., & Harris, N. B. (2001). Geochemical facies analysis of fine-grained siliciclastics using Th/U, Zr/Rb and (Zr+ Rb)/Sr ratios. *Chemical Geology*, 181(1–4), 131–146.
- Economic Times. (2016). ONGC to drill 17 exploratory wells for shale gas. <https://EconomicTimes.Indiatimes.Com/Industry/Energy/Oil-Gas/Ongc-to-Drill-17-Exploratory-Wells-for-Shale-Gas/Articleshow/51965836.Cms>. <https://economictimes.indiatimes.com/industry/energy/oil-gas/ongc-to-drill-17-exploratory-wells-for-shale-gas/articleshow/51965836.cms>
- EIA. (2011). World shale gas resources: An initial assessment of 14 regions outside the United States. *U.S. Energy Information Administration, April*, 365. <http://cdm16064.contentdm.oclc.org/cdm/ref/collection/p266901coll4/id/3447>
- EIA. (2013). *EIA/ARI World Shale Gas and Shale Oil Resource Assessment. June*, 707. http://www.eia.gov/analysis/studies/worldshalegas/pdf/chaptersxx_xxvi.pdf
- Espitalié, J. (1986). Use of Tmax as a maturation index for different types of organic matter: comparison with vitrinite reflectance. *Collection Colloques et Séminaires, Institut Français Du Pétrole, Paris, 44*, 475–496.
- Eyles, N. (1993). Earth's glacial record and its tectonic setting. *Earth-Science Reviews*, 35(1–2), 1–248.
- Eyles, N., Mory, A. J., & Backhouse, J. (2002). Carboniferous–Permian palynostratigraphy of west Australian marine rift basins: resolving tectonic and eustatic controls during Gondwanan glaciations. *Palaeogeography, Palaeoclimatology, Palaeoecology*, 184(3–4), 305–319.
- Gale, J. F. W., Reed, R. M., & Holder, J. (2007). Natural fractures in the Barnett Shale and their importance for hydraulic fracture treatments. *AAPG Bulletin*, 91(4), 603–622.

- Gamero Diaz, H., Miller, C. K., Lewis, R. E., & Contreras Fuentes, C. (2013). Evaluating the impact of mineralogy on reservoir quality and completion quality of organic shale plays. *Search and Discovery*, 41221(41221), 5pp.
- German, C. R., & Elderfield, H. (1990). Application of the Ce anomaly as a paleoredox indicator: the ground rules. *Paleoceanography*, 5(5), 823–833.
- Ghosh, S., Mukhopadhyay, J., & Chakraborty, A. (2019). Clay Mineral and Geochemical Proxies for Intense Climate Change in the Permian Gondwana Rock Record from Eastern India. *Research*, 2019, 8974075.
- Goodarzi, F. (2020). Comparison of the geochemistry of lacustrine oil shales of Mississippian age from Nova Scotia and New Brunswick, Canada. *International Journal of Coal Geology*, 220, 103398. <https://doi.org/10.1016/j.coal.2020.103398>
- Guo, T., Zhang, S., Qu, Z., Zhou, T., Xiao, Y., & Gao, J. (2014). Experimental study of hydraulic fracturing for shale by stimulated reservoir volume. *Fuel*, 128, 373–380.
- Guo, Z., Chapman, M., & Li, X. (2012). A shale rock physics model and its application in the prediction of brittleness index, mineralogy, and porosity of the Barnett Shale. *Society of Exploration Geophysicists International Exposition and 82nd Annual Meeting 2012, SEG 2012*, 2406–2410. <https://doi.org/10.1190/segam2012-0777.1>
- Gupta, S. K. (2006). Basin architecture and petroleum system of Krishna Godavari Basin, east coast of India. *Leading Edge (Tulsa, OK)*, 25(7), 830–837. <https://doi.org/10.1190/1.2221360>
- Hackley, P. C., & Lewan, M. (2018). Understanding and distinguishing reflectance measurements of solid bitumen and vitrinite using hydrous pyrolysis: implications to petroleum assessment. *AAPG Bulletin*, 102(6), 1119–1140.
- Hall, C. D. (2019). Compositional and Diagenetic Controls on Brittleness in Organic Siliceous Mudrocks. In W. Camp, K. Milliken, K. Taylor, N. Fishman, P. Hackley, & J. Macquaker (Eds.), *Mudstone diagenesis: Research perspectives for shale hydrocarbon reservoirs, seals, and source rocks* (pp. 103–120). AAPG Memoir 120. <https://doi.org/https://doi.org/10.1306/13672213M1213823>
- Hallberg, R. O. (1976). A geochemical method for investigation of palaeoredox conditions in sediments. *Ambio Special Report*, 4, 139–147.
- Harnois, L. (1988). The CIW index: a new chemical index of weathering. *SedG*, 55(3), 319–322.
- Hatch, J. R., & Leventhal, J. S. (1992). Relationship between inferred redox potential of the depositional environment and geochemistry of the Upper

- Pennsylvanian (Missourian) Stark Shale Member of the Dennis Limestone, Wabaunsee County, Kansas, USA. *Chemical Geology*, 99(1–3), 65–82.
- Hazen, R. M., Papineau, D., Bleeker, W., Downs, R. T., Ferry, J. M., McCoy, T. J., Sverjensky, D. A., & Yang, H. (2008). Mineral evolution. *American Mineralogist*, 93(11–12), 1693–1720.
- Hazra, B., Varma, A. K., Bandopadhyay, A. K., Chakravarty, S., Buragohain, J., Samad, S. K., & Prasad, A. K. (2016). FTIR, XRF, XRD and SEM characteristics of Permian shales, India. *Journal of Natural Gas Science and Engineering*, 32, 239–255. <https://doi.org/10.1016/j.jngse.2016.03.098>
- Hazra, B., Wood, D. A., Vishal, V., Varma, A. K., Sakha, D., & Singh, A. K. (2018). Porosity controls and fractal disposition of organic-rich Permian shales using low-pressure adsorption techniques. *Fuel*, 220(October 2017), 837–848. <https://doi.org/10.1016/j.fuel.2018.02.023>
- He, X., Liu, X., Nie, B., & Song, D. (2017). FTIR and Raman spectroscopy characterization of functional groups in various rank coals. *Fuel*, 206, 555–563. <https://doi.org/10.1016/j.fuel.2017.05.101>
- Henderson, P. (1984). *Rare earth element geochemistry*. Elsevier.
- Herron, M. M. (1988). Geochemical classification of terrigenous sands and shales from core or log data. *Journal of Sedimentary Research*, 58(5), 820–829.
- Holland, H. D. (1984). *Chemical Evolution of the Atmosphere and Oceans*. Princeton Univ Press, Princeton.
- Hu, Y., Wu, K., & Gonzalez Perdomo, M. E. (2015). *SPE-177010-MS New Models of Brittleness Index for Shale Gas Reservoirs: Weights of Brittle Minerals and Rock Mechanics Parameters A fully-coupled semi-analytical model for effective gas View project Multi-phase flow mechanisms through unconventional gas/o. April 2016*. <https://doi.org/10.13140/RG.2.1.3199.4001>
- Hunt, J. M. (1996). *Petroleum Geochemistry and Geology*. WH Freeman and Company. *New York*, 1–58.
- ICCP. (1998). The new vitrinite classification (ICCP System 1994). *Fuel*, 77(5), 349–358.
- ICCP. (2001). New inertinite classification (ICCP System 1994). *Fuel*, 80(4), 459–471. [https://doi.org/10.1016/S0016-2361\(00\)00102-2](https://doi.org/10.1016/S0016-2361(00)00102-2)
- Isbell, J. L., Miller, M. F., Wolfe, K. L., & Lenaker, P. A. (2003). Timing of late Paleozoic glaciation in Gondwana: was glaciation responsible for the development of northern hemisphere cyclothem? In M. A. Chan & A. . Archer (Eds.), *Extreme depositional environments: Mega end members in geologic time*. Boulder, USA: Geological Society of America Special Paper

- 370 (pp. 5–24). Geological Society of America.
- Jain, V. K., Cherukupalli, P. K., Rao, R., Bohra, A. S., & Tewari, P. K. (2004). Reservoir Characterization–Geocellular Model for Mandapeta sand of Mandapeta Field, KG Basin–A holistic Approach. *Proceedings of the 8th Conference on Petroleum Geophysics, Hyderabad, India*, 704–709.
- Jarvie, D. M., Claxton, B. L., Henk, F., & Breyer, J. T. (2001). Oil and shale gas from the Barnett Shale, Ft Worth Basin, Texas. *AAPG National Convention*, 85, A100.
- Jarvie, D. M., Hill, R. J., Ruble, T. E., & Pollastro, R. M. (2007). Unconventional shale-gas systems: The Mississippian Barnett Shale of north-central Texas as one model for thermogenic shale-gas assessment. *American Association of Petroleum Geologists Bulletin*, 91(4), 475–499. <https://doi.org/10.1306/12190606068>
- Jasper, J. P., & Hayes, J. M. (1990). A carbon isotope record of CO₂ levels during the late Quaternary. *Nature*, 347(6292), 462–464.
- Javadpour, F. (2009). Nanopores and apparent permeability of gas flow in mudrocks (shales and siltstone). *Journal of Canadian Petroleum Technology*, 48(8), 16–21. <https://doi.org/10.2118/09-08-16-DA>
- Ji, L., Zhang, T., Milliken, K. L., Qu, J., & Zhang, X. (2012). Experimental investigation of main controls to methane adsorption in clay-rich rocks. *Applied Geochemistry*, 27(12), 2533–2545. <https://doi.org/10.1016/j.apgeochem.2012.08.027>
- Jiang, F., Chen, D., Chen, J., Li, Q., Liu, Y., Shao, X., Hu, T., & Dai, J. (2016). Fractal analysis of shale pore structure of continental gas shale reservoir in the Ordos Basin, NW China. *Energy & Fuels*, 30(6), 4676–4689.
- Jones, B., & Manning, D. A. C. (1994). Comparison of geochemical indices used for the interpretation of palaeoredox conditions in ancient mudstones. *Chemical Geology*, 111(1–4), 111–129.
- Josh, M., Esteban, L., Piane, C. D., Sarout, J., Dewhurst, D. N., & Clennell, M. B. (2012). Journal of Petroleum Science and Engineering Laboratory characterisation of shale properties. *Journal of Petroleum Science and Engineering*, 88–89, 107–124. <https://doi.org/10.1016/j.petrol.2012.01.023>
- Kala, S., Devaraju, J., De, S., & Rasheed, M. A. (2021). Multiproxy geochemical characterization of Kommugudem Formation, Krishna Godavari Basin, India: Implication on hydrocarbon potential and shale brittleness. *Geological Journal*, 1–18. <https://doi.org/https://doi.org/10.1002/gj.4346>
- Kala, S., Devaraju, J., Tiwari, D. M., Rasheed, M. A., & Lakhan, N. (2021). Organic petrology and geochemistry of Early Permian shales from the Krishna-Godavari Basin, India: Implications for Gondwana

- palaeoenvironment and climate. *Geological Journal*, 56(11), 5621– 5641.
<https://doi.org/https://doi.org/10.1002/gj.4262>
- Kala, S., Turlapati, V. Y., Devaraju, J., Rasheed, M. A., Sivaranjane, N., & Ravi, A. (2021). Impact of sedimentary environment on pore parameters of thermally mature Permian shale: A study from Kommugudem Formation of Krishna Godavari Basin, India. *Marine and Petroleum Geology*, 132, 105236. <https://doi.org/https://doi.org/10.1016/j.marpetgeo.2021.105236>
- Khan, M. S. R., Sharma, A. K., Sahota, S. K., & Mathur, M. (2000). Generation and hydrocarbon entrapment within gondwanan sediments of the mandapeta area, krishna-godavari basin, india. *Organic Geochemistry*, 31(12), 1495–1507. [https://doi.org/10.1016/S0146-6380\(00\)00132-7](https://doi.org/10.1016/S0146-6380(00)00132-7)
- Khatibi, S., Ostadhassan, M., Tuschel, D., Gentzis, T., & Carvajal-Ortiz, H. (2018). Evaluating molecular evolution of kerogen by raman spectroscopy: correlation with optical microscopy and rock-eval pyrolysis. *Energies*, 11(6), 1406.
- Kim, J., Kim, D., Lee, W., Lee, Y., & Kim, H. (2017). Impact of total organic carbon and specific surface area on the adsorption capacity in Horn River shale. *Journal of Petroleum Science and Engineering*, 149, 331–339. <https://doi.org/10.1016/j.petrol.2016.10.053>
- Kuila, U., & Prasad, M. (2013). Specific surface area and pore-size distribution in clays and shales. *Geophysical Prospecting*, 61(2), 341–362. <https://doi.org/10.1111/1365-2478.12028>
- Kumar, S., Das, S., Bastia, R., & Ojha, K. (2018). Mineralogical and morphological characterization of Older Cambay Shale from North Cambay Basin, India: Implication for shale oil/gas development. *Marine and Petroleum Geology*, 97, 339–354. <https://doi.org/10.1016/j.marpetgeo.2018.07.020>
- Kumar, S., & Ojha, K. (2021). Reaction kinetic, maturity, burial and thermal histories modelling of cambay shale source rocks, Cambay Basin, Western India. *Journal of Petroleum Science and Engineering*, 202, 108543. <https://doi.org/https://doi.org/10.1016/j.petrol.2021.108543>
- Kumar, S., Ojha, K., Bastia, R., Garg, K., Das, S., & Mohanty, D. (2017). Evaluation of Eocene source rock for potential shale oil and gas generation in north Cambay Basin, India. *Marine and Petroleum Geology*, 88, 141–154. <https://doi.org/https://doi.org/10.1016/j.marpetgeo.2017.08.015>
- Labani, M. M., Rezaee, R., Saeedi, A., & Al Hinai, A. (2013). Evaluation of pore size spectrum of gas shale reservoirs using low pressure nitrogen adsorption, gas expansion and mercury porosimetry: A case study from the Perth and Canning Basins, Western Australia. *Journal of Petroleum Science and Engineering*, 112, 7–16.

- Lakshminarayana, G. (2002). Evolution in Basin Fill Style during the Mesozoic Gondwana Continental Break-up in the Godavari Triple Junction, SE India. *Gondwana Research*, 5(1), 227–244. [https://doi.org/10.1016/S1342-937X\(05\)70906-0](https://doi.org/10.1016/S1342-937X(05)70906-0)
- Leahy-Dios, A., Das, M., Agarwal, A., & Kaminsky, R. D. (2011). Modeling of transport phenomena and multicomponent sorption for shale gas and coalbed methane in an unstructured grid simulator. *SPE Annual Technical Conference and Exhibition*.
- Li, D., Li, R., Tan, C., Zhao, D., Xue, T., Zhao, B., Khaled, A., Liu, F., & Xu, F. (2019). Origin of silica, paleoenvironment, and organic matter enrichment in the Lower Paleozoic Niutitang and Longmaxi formations of the northwestern Upper Yangtze Plate: Significance for hydrocarbon exploration. *Marine and Petroleum Geology*, 103(March), 404–421. <https://doi.org/10.1016/j.marpetgeo.2019.02.025>
- Li, X., Gang, W., Yao, J., Gao, G., Wang, C., Li, J., Liu, Y., Guo, Y., & Yang, S. (2020). Major and trace elements as indicators for organic matter enrichment of marine carbonate rocks: A case study of Ordovician subsalt marine formations in the central-eastern Ordos Basin, North China. *Marine and Petroleum Geology*, 111(December 2018), 461–475. <https://doi.org/10.1016/j.marpetgeo.2019.08.028>
- Liu, K., & Ostadhassan, M. (2017a). Microstructural and geomechanical analysis of Bakken shale at nanoscale. *Journal of Petroleum Science and Engineering*, 153, 133–144.
- Liu, K., & Ostadhassan, M. (2017b). Quantification of the microstructures of Bakken shale reservoirs using multi-fractal and lacunarity analysis. *Journal of Natural Gas Science and Engineering*, 39, 62–71.
- Liu, K., Ostadhassan, M., Sun, L., Zou, J., Yuan, Y., Gentzis, T., Zhang, Y., Carvajal-Ortiz, H., & Rezaee, R. (2019). A comprehensive pore structure study of the Bakken Shale with SANS, N₂ adsorption and mercury intrusion. *Fuel*, 245, 274–285.
- Liu, K., Ostadhassan, M., Zhou, J., Gentzis, T., & Rezaee, R. (2017). Nanoscale pore structure characterization of the Bakken shale in the USA. *Fuel*, 209(August), 567–578. <https://doi.org/10.1016/j.fuel.2017.08.034>
- Liu, K., Ostadhassan, M., Zou, J., Gentzis, T., Rezaee, R., Bubach, B., & Carvajal-Ortiz, H. (2018). Multifractal analysis of gas adsorption isotherms for pore structure characterization of the Bakken Shale. *Fuel*, 219, 296–311.
- López-Gamundí, O. R. (1997). Glacial-postglacial transition in the Late Paleozoic basins of southern South America. In I. P. Martini (Ed.), *Late Glacial and Postglacial Environmental Changes-Quaternary, Carboniferous-Permian, and Proterozoic*. Oxford University Press, New York.

- López-Gamundí, O. R., & Buatois, L. A. (2010). *Introduction: Late Paleozoic glacial events and postglacial transgressions in Gondwana* (Vol. 468). Geological Society of America.
[https://doi.org/https://doi.org/10.1130/2010.2468\(00\)](https://doi.org/https://doi.org/10.1130/2010.2468(00))
- Loucks, R. G., Reed, R. M., Ruppel, S. C., & Hammes, U. (2012). Spectrum of pore types and networks in mudrocks and a descriptive classification for matrix-related mudrock pores. *AAPG Bulletin*, *96*(6), 1071–1098.
- Loucks, R. G., Reed, R. M., Ruppel, S. C., & Jarvie, D. M. (2009). Morphology, genesis, and distribution of nanometer-scale pores in siliceous mudstones of the Mississippian Barnett Shale. *Journal of Sedimentary Research*, *79*(12), 848–861.
- Loucks, R. G., & Ruppel, S. C. (2007). Mississippian Barnett Shale: Lithofacies and depositional setting of a deep-water shale-gas succession in the Fort Worth Basin, Texas. *AAPG Bulletin*, *91*(4), 579–601.
<https://doi.org/10.1306/11020606059>
- Lutynski, M., & González, M. Á. G. (2016). Characteristics of carbon dioxide sorption in coal and gas shale—The effect of particle size. *Journal of Natural Gas Science and Engineering*, *28*, 558–565.
- MacRae, N. D., Nesbitt, H. W., & Kronberg, B. I. (1992). Development of a positive Eu anomaly during diagenesis. *Earth and Planetary Science Letters*, *109*(3–4), 585–591.
- Mani, D., Patil, D. J., Dayal, A. M., & Prasad, B. N. (2015). Thermal maturity, source rock potential and kinetics of hydrocarbon generation in Permian shales from the Damodar Valley basin, Eastern India. *Marine and Petroleum Geology*, *66*, 1056–1072. <https://doi.org/10.1016/j.marpetgeo.2015.08.019>
- Mani, D., Ratnam, B., Kalpana, M. S., Patil, D. J., & Dayal, A. M. (2016). Elemental and organic geochemistry of Gondwana sediments from the Krishna-Godavari Basin, India. *Chemie Der Erde*, *76*(1), 117–131.
<https://doi.org/10.1016/j.chemer.2016.01.002>
- Martinez-Ruiz, F., Ortega-Huertas, M., & Palomo, I. (1999). Positive Eu anomaly development during diagenesis of the K/T boundary ejecta layer in the Agost section (SE Spain): implications for trace-element remobilization. *Terra Nova*, *11*(6), 290–296.
- Marzi, R., Torkelson, B. E., & Olson, R. K. (1993). A revised carbon preference index. *Organic Geochemistry*, *20*(8), 1303–1306.
[https://doi.org/https://doi.org/10.1016/0146-6380\(93\)90016-5](https://doi.org/https://doi.org/10.1016/0146-6380(93)90016-5)
- McLennan, S. M. (2001). Relationships between the trace element composition of sedimentary rocks and upper continental crust. *Geochemistry, Geophysics, Geosystems*, *2*(4), 2000GC000109.
<https://doi.org/https://doi.org/10.1029/2000GC000109>

- Miao, J., Zhao, J., Li, W., Han, Z., & Ma, J. (2005). Research on the diagenetic environments about source rocks in south Ordos Basin [J]. *Journal of Northwest University (Natural Science Edition)*, 6, 771–776.
- Milliken, K. L., Esch, W. L., Reed, R. M., & Zhang, T. (2012). Grain assemblages and strong diagenetic overprinting in siliceous mudrocks, Barnett Shale (Mississippian), Fort Worth Basin, Texas. *Properties of Siliceous Mudrocks, Barnett Shale, Texas. Aapg Bulletin*, 96(8), 1553–1578.
- Milliken, K. L., & Reed, R. M. (2010). Multiple causes of diagenetic fabric anisotropy in weakly consolidated mud, Nankai accretionary prism, IODP Expedition 316. *Journal of Structural Geology*, 32(12), 1887–1898.
- Misra, S., Varma, A. K., Das, S. K., Mani, D., & Biswas, S. (2018). Thermal controls of lamprophyre sill on hydrocarbon generation outlook of shale beds in Raniganj basin, India. *Journal of Natural Gas Science and Engineering*, 56(April), 536–548. <https://doi.org/10.1016/j.jngse.2018.06.028>
- Mitra, A., Warrington, D. S., & Sommer, A. (2010). Application of lithofacies models to characterize unconventional shale gas reservoirs and identify optimal completion intervals. *SPE Western Regional Meeting*.
- Modica, C. J., & Lapiere, S. G. (2012). Estimation of kerogen porosity in source rocks as a function of thermal transformation: Example from the Mowry Shale in the Powder River Basin of Wyoming. *Estimation of Kerogen Porosity as a Function of Thermal Transformation. AAPG Bulletin*, 96(1), 87–108.
- Montañez, I. P., & Poulsen, C. J. (2013). The Late Paleozoic ice age: an evolving paradigm. *Annual Review of Earth and Planetary Sciences*, 41, 629–656.
- Mukhopadhyay, G., Mukhopadhyay, S. K., Roychowdhury, M., & Parui, P. K. (2010). Stratigraphic correlation between different Gondwana Basins of India. *Journal of the Geological Society of India*, 76(3), 251–266. <https://doi.org/10.1007/s12594-010-0097-6>
- Murray, R. W., Buchholtz ten Brink, M. R., Jones, D. L., Gerlach, D. C., & Russ III, G. P. (1990). Rare earth elements as indicators of different marine depositional environments in chert and shale. *Geology*, 18(3), 268–271.
- Murray, R. W., & Leinen, M. (1996). Scavenged excess aluminum and its relationship to bulk titanium in biogenic sediment from the central equatorial Pacific Ocean. *Geochimica et Cosmochimica Acta*, 60(20), 3869–3878.
- Nairn, A. E. M., & Smithwick, M. E. (1976). Permian paleogeography and climatology. In F. H. (Ed.), *The Continental Permian in Central, West, and South Europe. Nato Advanced Study Institutes Series (Series C - Mathematical and Physical Sciences)*, vol 22. (pp. 283–312). Springer. https://doi.org/https://doi.org/10.1007/978-94-010-1461-8_21

- Nesbitt, H. W., & Young, G. M. (1984). Prediction of some weathering trends of plutonic and volcanic rocks based on thermodynamic and kinetic considerations. *Geochimica et Cosmochimica Acta*, 48(7), 1523–1534.
- O'Brien, N. R. (1970). The fabric of shale—an electron-microscope study. *Sedimentology*, 15(3-4), 229–246.
- Padhy, P. K., Das, S. K., & Kumar, A. (2013). Krishna-Godavari Continental Rift Basin : Shale Gas and Oil Play Systems. *10th Biennial International Conference*, 1–8.
- Padhy, P. K., Kumar, A., Chandra, Y. R., Das, S. K., Jha, S. K., & Advani, D. R. (2016). Shale oil exploration from Paleocene-early Eocene sequence in Cambay rift basin, India. *Proceedings of the Indian National Science Academy*, 82(3), 945–963.
- Painter, P. C., Snyder, R. W., Starsinic, M., Coleman, M. M., Kuehn, D. W., & Davis, A. (1981). Concerning the application of FT-IR to the study of coal: a critical assessment of band assignments and the application of spectral analysis programs. *Applied Spectroscopy*, 35(5), 475–485.
- Passey, Q. R., Bohacs, K., Esch, W. L., Klimentidis, R., & Sinha, S. (2010). From oil-prone source rock to gas-producing shale reservoir-geologic and petrophysical characterization of unconventional shale gas reservoirs. *International Oil and Gas Conference and Exhibition in China*.
- Peng, J., Milliken, K. L., & Fu, Q. (2020). Quartz types in the Upper Pennsylvanian organic-rich Cline Shale (Wolfcamp D), Midland Basin, Texas: Implications for silica diagenesis, porosity evolution and rock mechanical properties. *Sedimentology*, 67(4), 2040–2064.
- Peters, K. E. (1986). Guidelines for Evaluating Petroleum Source Rock Using Programmed Pyrolysis. *AAPG Bulletin*, 70, 318–329.
<https://doi.org/10.1306/94885688-1704-11D7-8645000102C1865D>
- Peters, K. E., & Cassa, M. R. (1994). Applied source rock geochemistry: Chapter 5: Part II. Essential elements. In L. B. Magoon & W. G. Dow (Eds.), *The petroleum system from source to trap* (pp. 93–120). AAPG Memoir 60.
- Peters, K. E., Walters, C. C., & Moldowan, J. M. (2005). *The biomarker guide: Biomarkers and isotopes in the environment and human history*. Cambridge University Press.
- Pickel, W., Kus, J., Flores, D., Kalaitzidis, S., Christanis, K., Cardott, B. J., Miszkennan, M., Rodrigues, S., Hentschel, A., Hamor-Vido, M., Crosdale, P., & Wagner, N. (2017). Classification of liptinite – ICCP System 1994. *International Journal of Coal Geology*, 169, 40–61.
<https://doi.org/10.1016/j.coal.2016.11.004>
- Pophare, A., Prasad, A. L., & Katley, R. (2017). Sulphur Distribution Patterns in

- Permian Coal Seams of Kamptee Coalfield, Central India 1 2 2. *Journal of Geosciences Research*, 1, 203–209.
- Prasad, B., Pundir, B. S., & Swamy, S. N. (2000). Age, depositional environment, source potential and distribution of pay sands in Mandapeta subbasin with remarks on the biostratigraphic classification of Gondwana sediments in Krishna-Godavari basin. *Indian Journal of Petroleum Geology*, 9(1), 1–19.
- Rabbani, A. R., & Kamali, M. R. (2005). Source rock evaluation and petroleum geochemistry, offshore SW Iran. *Journal of Petroleum Geology*, 28(4), 413–428.
- Rao, G. N. (2001). Sedimentation, stratigraphy, and petroleum potential of Krishna-Godavari basin, East Coast of India. *AAPG Bulletin*, 85(9), 1623–1643.
- Rickman, R., Mullen, M., Petre, E., Grieser, B., & Kundert, D. (2008). A practical use of shale petrophysics for stimulation design optimization: All shale plays are not clones of the Barnett Shale. *Proceedings - SPE Annual Technical Conference and Exhibition*, 2(Wang), 840–850.
<https://doi.org/10.2118/115258-ms>
- Rimmer, S. M. (2004). Geochemical paleoredox indicators in Devonian–Mississippian black shales, central Appalachian Basin (USA). *Chemical Geology*, 206(3–4), 373–391.
- Roaldest, E. (1978). *Mineralogical and Chemical Changes during Weathering, Transportation and Sedimentation in Different Environments*. Ph. D. Thesis, University of Oslo, Oslo, Norway.
- Roser, B. P., & Korsch, R. J. (1986). Determination of tectonic setting of sandstone-mudstone suites using SiO₂ content and K₂O/Na₂O ratio. *The Journal of Geology*, 94(5), 635–650.
- Ross, D. J. K., & Bustin, R. M. (2006). Sediment geochemistry of the lower Jurassic Gordondale member, northeastern British Columbia. *Bulletin of Canadian Petroleum Geology*, 54(4), 337–365.
- Ross, D. J. K., & Bustin, R. M. (2007). Impact of mass balance calculations on adsorption capacities in microporous shale gas reservoirs. *Fuel*, 86(17–18), 2696–2706. <https://doi.org/10.1016/j.fuel.2007.02.036>
- Ross, D. J. K., & Bustin, R. M. (2008). Characterizing the shale gas resource potential of Devonian-Mississippian strata in the Western Canada sedimentary basin: Application of an integrated formation evaluation. *American Association of Petroleum Geologists Bulletin*, 92(1), 87–125.
<https://doi.org/10.1306/09040707048>
- Ross, D. J. K., & Bustin, R. M. (2009a). Investigating the use of sedimentary geochemical proxies for paleoenvironment interpretation of thermally mature

- organic-rich strata: examples from the Devonian–Mississippian shales, Western Canadian Sedimentary Basin. *Chemical Geology*, 260(1–2), 1–19.
- Ross, D. J. K., & Bustin, R. M. (2009b). The importance of shale composition and pore structure upon gas storage potential of shale gas reservoirs. *Marine and Petroleum Geology*, 26(6), 916–927. <https://doi.org/10.1016/j.marpetgeo.2008.06.004>
- Roy, D. K., & Roser, B. P. (2013). Climatic control on the composition of Carboniferous–Permian Gondwana sediments, Khalaspir basin, Bangladesh. *Gondwana Research*, 23(3), 1163–1171.
- Sain, K., Rai, M., & Sen, M. K. (2014). A review on shale gas prospect in Indian sedimentary basins. 2, 183–194.
- Sajid, Z., Ismail, M. S., & Hanif, T. (2020). Mineralogical and geochemical imprints to determine the provenance, depositional history and tectonic settings of Triassic turbidites in the Semanggol and Semantan Basins, Peninsular Malaysia. *Journal of Asian Earth Sciences*, 203, 104539.
- Sanei, H., Wood, J. M., Ardakani, O. H., Clarkson, C. R., & Jiang, C. (2015). Characterization of organic matter fractions in an unconventional tight gas siltstone reservoir. *International Journal of Coal Geology*, 150–151, 296–305. <https://doi.org/https://doi.org/10.1016/j.coal.2015.04.004>
- Sastri, V. V., Venkatachala, B. S., & Narayanan, V. (1981). The evolution of the east coast of India. *Palaeogeography, Palaeoclimatology, Palaeoecology*, 36(1), 23–54. [https://doi.org/https://doi.org/10.1016/0031-0182\(81\)90047-X](https://doi.org/https://doi.org/10.1016/0031-0182(81)90047-X)
- Scalan, E. S., & Smith, J. E. (1970). An improved measure of the odd-even predominance in the normal alkanes of sediment extracts and petroleum. *Geochimica et Cosmochimica Acta*, 34(5), 611–620.
- Scheffler, K., Hoernes, S., & Schwark, L. (2003). Global changes during Carboniferous-Permian glaciation of Gondwana: Linking polar and equatorial climate evolution by geochemical proxies. *Geology*, 31(7), 605–608. [https://doi.org/10.1130/0091-7613\(2003\)031<0605:GCDCGO>2.0.CO;2](https://doi.org/10.1130/0091-7613(2003)031<0605:GCDCGO>2.0.CO;2)
- Schieber, J. (2013). SEM Observations on Ion-milled Samples of Devonian Black Shales from Indiana and New York: The Petrographic Context of Multiple Pore Types. In W. Camp, E. Diaz, & B. Wawak (Eds.), *Electron Microscopy of Shale Hydrocarbon Reservoirs* (pp. 153–171). American Association of Petroleum Geologists Memoir, Vol. 102.
- Schlueter, E. M., Zimmerman, R. W., Witherspoon, P. A., & Cook, N. G. W. (1997). The fractal dimension of pores in sedimentary rocks and its influence on permeability. *Engineering Geology*, 48(3–4), 199–215.
- Shandilya, A. (2017). *Synrift & Prerift Hydrocarbon Plays of KG Basin-The*

- Enfolding Enigma*. <https://www.spgindia.org/Jaipur2017-proceedings-published/pid-349-synrift-and-prerift-hydrocarbon-plays.pdf>
- Shao, X., Pang, X., Li, Q., Wang, P., Chen, D., Shen, W., & Zhao, Z. (2017). Pore structure and fractal characteristics of organic-rich shales: A case study of the lower Silurian Longmaxi shales in the Sichuan Basin, SW China. *Marine and Petroleum Geology*, *80*, 192–202. <https://doi.org/10.1016/j.marpetgeo.2016.11.025>
- Sharma, S. S., & Kulkarni, P. K. (2010). Gas Strike in Shale Reservoir in Dholka Field in Cambay Basin. *SPE Oil and Gas India Conference and Exhibition, Mumbai, India*, SPE-129082-MS. <https://doi.org/10.2118/129082-ms>
- Sing, K. S. W. (1985). Reporting physisorption data for gas/solid systems with special reference to the determination of surface area and porosity (Recommendations 1984). *Pure and Applied Chemistry*, *57*(4), 603–619.
- Singh, A., Das, S. K., Sinha, A. D., & Singh, P. (2018). Global shale gas and oil distribution with geological age vis-à-vis Indian Synrift Shale Sequences. *ONGC Bulletin*, *53*(1), 149–162.
- Singh, A. K., & Chakraborty, P. P. (2021). Geochemistry and hydrocarbon source rock potential of shales from the Palaeo-Mesoproterozoic Vindhyan Supergroup, central India. *Energy Geoscience*. <https://doi.org/https://doi.org/10.1016/j.engeos.2021.10.007>
- Sinha, A. K., Vijayagopal, K., Das, S. K., Advani, D. R., & Chandra, Y. R. (2010). Shale exploration in Indian sedimentary basins: Lesson learnt and way forward. *ONGC Bulletin*, *53*(2), 103.
- Slatt, R. M., & Abousleiman, Y. (2011). Merging sequence stratigraphy and geomechanics for unconventional gas shales. *The Leading Edge*, *30*(3), 274–282.
- Sondergeld, C. H., Ambrose, R. J., Rai, C. S., & Moncrieff, J. (2010). Microstructural studies of gas shales. *SPE Unconventional Gas Conference 2010*, 150–166.
- Sondergeld, C. H., Newsham, K. E., Comisky, J. T., Rice, M. C., & Rai, C. S. (2010). Petrophysical considerations in evaluating and producing shale gas resources. *Society of Petroleum Engineers - Canadian Unconventional Resources and International Petroleum Conference 2010*, *1*, 1–34. <https://doi.org/10.2118/131768-ms>
- Song, L., & Carr, T. R. (2020). The pore structural evolution of the Marcellus and Mahantango shales, Appalachian Basin. *Marine and Petroleum Geology*, *114*, 104226. <https://doi.org/10.1016/j.marpetgeo.2020.104226>
- Stephenson, M. H., Leng, M. J., Vane, C. H., Osterloff, P. L., & Arrowsmith, C. (2005). Investigating the record of Permian climate change from argillaceous

- sedimentary rocks, Oman. *Journal of the Geological Society*, 162(4), 641–651.
- Stephenson, M. H., & Osterloff, P. L. (2002). *Palynology of the deglaciation sequence represented by the Lower Permian Rahab and Lower Gharif members, Oman* (Issue 40). AASP Foundation.
- Suttner, L. J., & Dutta, P. K. (1986). Alluvial sandstone composition and paleoclimate; I, Framework mineralogy. *Journal of Sedimentary Research*, 56(3), 329–345.
- Tannenbaum, E., Huizinga, B. J., & Kaplan, I. R. (1986). Role of minerals in thermal alteration of organic matter—II: A material balance. *AAPG Bulletin*, 70(9), 1156–1165.
- Taylor, S. R., & McLennan, S. M. (1985). *The continental crust: its composition and evolution*. Wiley-Blackwell Scientific Pub., Palo Alto, CA.
- Temizel, C., Canbaz, C. H., Gok, I. M., Roshankhah, S., Palabiyik, Y., Deniz-Paker, M., Hosgor, F. B., Ozyurtkan, H., Aksahan, F., & Gormez, E. (2020). A Thorough Review and Latest Advances in Shale Reservoirs: Seismic to Surveillance. *SPE Latin American and Caribbean Petroleum Engineering Conference*.
- Tewari, A., D’Rozario, A., Bhattacharya, S., Barua, A., Bera, M., Bera, S., & Dutta, S. (2019). Biomarker signatures of the iconic *Glossopteris* plant. *Palaeogeography, Palaeoclimatology, Palaeoecology*, 531. <https://doi.org/10.1016/j.palaeo.2018.08.001>
- Tissot, B. P., & Welte, D. H. (1984). *Petroleum formation and occurrence* (2nd ed.). Springer-Verlag.
- Tribouvillard, N., Algeo, T. J., Baudin, F., & Riboulleau, A. (2012). Analysis of marine environmental conditions based on molybdenum–uranium covariation—Applications to Mesozoic paleoceanography. *Chemical Geology*, 324, 46–58.
- Tribouvillard, N., Algeo, T. J., Lyons, T., & Riboulleau, A. (2006). Trace metals as paleoredox and paleoproductivity proxies: an update. *Chemical Geology*, 232(1–2), 12–32.
- Tripathy, A., Kumar, A., Srinivasan, V., Singh, K. H., & Singh, T. N. (2019). Fractal analysis and spatial disposition of porosity in major Indian gas shales using low-pressure nitrogen adsorption and advanced image segmentation. *Journal of Natural Gas Science and Engineering*, 72(June). <https://doi.org/10.1016/j.jngse.2019.103009>
- Turlapati, V. Y., Prusty, B. K., & Bakshi, T. (2020). Detailed Pore Structure Study of Damodar Valley and Upper Assam Basin Shales Using Fractal Analysis. *Energy & Fuels*, 34(11), 14001–14011.

- Tuttle, M. L. W., Fahy, J. W., Elliott, J. G., Grauch, R. I., & Stillings, L. L. (2014). Contaminants from cretaceous black shale: II. Effect of geology, weathering, climate, and land use on salinity and selenium cycling, Mancos Shale landscapes, southwestern United States. *Applied Geochemistry*, *46*, 72–84.
- Varma, A. K., Hazra, B., Samad, S. K., Panda, S., & Mendhe, V. A. (2014). Methane sorption dynamics and hydrocarbon generation of shale samples from West Bokaro and Raniganj basins, India. *Journal of Natural Gas Science and Engineering*, *21*, 1138–1147.
<https://doi.org/10.1016/j.jngse.2014.11.011>
- Veivers, J. J. (1994). Earth's paleoclimate and sedimentary environments. *Pangea: Paleoclimate, Tectonics, and Sedimentation during Accretion, Zenith, and Breakup of a Supercontinent*, *288*, 13.
- Veivers, J. J., & Powell, M. C. A. (1987). Late Paleozoic glacial episodes in Gondwanaland reflected in transgressive-regressive depositional sequences in Euramerica. *Geological Society of America Bulletin*, *98*(4), 475–487.
- Veivers, J. J., & Tewari, R. C. (1995). Gondwana master basin of Peninsular India between Tethys and the interior of the Gondwanaland province of Pangea. In *Memoir of the Geological Society of America* (Vol. 187).
<https://doi.org/10.1130/0-8137-1187-8.1>
- Vishal, V., Chandra, D., Bahadur, J., Sen, D., Hazra, B., Mahanta, B., & Mani, D. (2019). Interpreting Pore Dimensions in Gas Shales Using a Combination of SEM Imaging, Small-Angle Neutron Scattering, and Low-Pressure Gas Adsorption [Research-article]. *Energy and Fuels*, *33*(6), 4835–4848.
<https://doi.org/10.1021/acs.energyfuels.9b00442>
- Waelbroeck, C., Labeyrie, L., Michel, E., Duplessy, J. C., McManus, J. F., Lambeck, K., Balbon, E., & Labracherie, M. (2002). Sea-level and deep water temperature changes derived from benthic foraminifera isotopic records. *Quaternary Science Reviews*, *21*(1–3), 295–305.
- Wang, F. P., & Gale, J. F. W. (2009). Screening criteria for shale-gas systems. *GCAGS Transactions*, *59*, 779–793.
- Wang, H., Li, G., & Shen, Z. (2012). A Feasibility Analysis on Shale Gas Exploitation with Supercritical Carbon Dioxide. *Energy Sources, Part A: Recovery, Utilization, and Environmental Effects*, *34*(15), 1426–1435.
<https://doi.org/10.1080/15567036.2010.529570>
- Weaver, C. E. (1989). *Clays, muds, and shales*. Elsevier.
- Webb, P. A. (2003). Introduction to chemical adsorption analytical techniques and their applications to catalysis. *Micromeritics Instrument Corp. Technical Publications*, 1–12.

- Webb, P. A., & Orr, C. (1997). *Analytical methods in fine particle technology*. Micromeritics Instrument Corp.
- Wedepohl, K. H. (1971). Environmental influences on the chemical composition of shales and clays. *Physics and Chemistry of the Earth*, 8(C), 307–333. [https://doi.org/10.1016/0079-1946\(71\)90020-6](https://doi.org/10.1016/0079-1946(71)90020-6)
- Wei, Z., Wang, Y., Wang, G., Sun, Z., & Xu, L. (2018). Pore characterization of organic-rich Late Permian Da-long Formation shale in the Sichuan Basin, southwestern China. *Fuel*, 211, 507–516.
- Wopfner, H. (1999). The early Permian deglaciation event between East Africa and northwestern Australia. *Journal of African Earth Sciences*, 29(1), 77–90.
- Wopfner, H., & Kreuser, T. (1986). Evidence for Late Palaeozoic glaciation in southern Tanzania. *Palaeogeography, Palaeoclimatology, Palaeoecology*, 56(3–4), 259–275.
- Worden, R. H., Smalley, P. C., & Oxtoby, N. H. (1995). Gas souring by thermochemical sulfate reduction at 140 C. *Aapg Bulletin*, 79(6), 854–863.
- Yang, F., Ning, Z., & Liu, H. (2014). Fractal characteristics of shales from a shale gas reservoir in the Sichuan Basin, China. *Fuel*, 115, 378–384. <https://doi.org/10.1016/j.fuel.2013.07.040>
- Yang, R., He, S., Yi, J., & Hu, Q. (2016). Nano-scale pore structure and fractal dimension of organic-rich Wufeng-Longmaxi shale from Jiaoshiba area, Sichuan Basin: Investigations using FE-SEM, gas adsorption and helium pycnometry. *Marine and Petroleum Geology*, 70, 27–45. <https://doi.org/10.1016/j.marpetgeo.2015.11.019>
- Yang, Z., Wang, L., Chen, Z., Xiang, D., Hou, D., Ho, C. L., & Zhang, G. (2018). Micromechanical characterization of fluid/shale interactions by means of nanoindentation. *SPE Reservoir Evaluation & Engineering*, 21(02), 405–417.
- Yao, Y., Liu, D., Tang, D., Tang, S., & Huang, W. (2008). Fractal characterization of adsorption-pores of coals from North China: an investigation on CH₄ adsorption capacity of coals. *International Journal of Coal Geology*, 73(1), 27–42.
- Yao, Y., Liu, D., Tang, D., Tang, S., Huang, W., Liu, Z., & Che, Y. (2009). Fractal characterization of seepage-pores of coals from China: an investigation on permeability of coals. *Computers & Geosciences*, 35(6), 1159–1166.
- Yu, K., Gan, Y., Ju, Y., & Shao, C. (2020). Influence of sedimentary environment on the brittleness of coal-bearing shale: Evidence from geochemistry and micropetrology. *Journal of Petroleum Science and Engineering*, 185(October 2019). <https://doi.org/10.1016/j.petrol.2019.106603>

- Zeng, W., Zhang, J., Ding, W., Zhao, S., Zhang, Y., Liu, Z., & Jiu, K. (2013). Fracture development in Paleozoic shale of Chongqing area (South China). Part one: Fracture characteristics and comparative analysis of main controlling factors. *Journal of Asian Earth Sciences*, *75*, 251–266.
- Zhang, C., Dong, D., Wang, Y., & Guan, Q. (2017). Brittleness evaluation of the Upper Ordovician Wufeng–Lower Silurian Longmaxi shale in Southern Sichuan Basin, China. *Energy Exploration and Exploitation*, *35*(4), 430–443. <https://doi.org/10.1177/0144598716687929>
- Zhang, T., Ellis, G. S., Ruppel, S. C., Milliken, K., & Yang, R. (2012). Effect of organic-matter type and thermal maturity on methane adsorption in shale-gas systems. *Organic Geochemistry*, *47*, 120–131.
- Zheng, S., Feng, Q., Tribovillard, N., Servais, T., Zhang, Y., & Gao, B. (2020). New insight into factors controlling organic matter distribution in Lower Cambrian source rocks: a study from the Qiongzhusi Formation in South China. *Journal of Earth Science*, *31*(1), 181–194.
- Zheng, X., Schovsbo, N. H., Bian, L., Luo, Q., Zhong, N., Rudra, A., Goodarzi, F., & Sanei, H. (2021). Alteration of organic macerals by uranium irradiation in lower Paleozoic marine shales. *International Journal of Coal Geology*, *239*, 103713.
- Zhou, W., Algeo, T. J., Ruan, X., Luo, G., Chen, Z.-Q., & Xie, S. (2017). Expansion of photic-zone euxinia during the Permian–Triassic biotic crisis and its causes: Microbial biomarker records. *Palaeogeography, Palaeoclimatology, Palaeoecology*, *474*, 140–151. <https://doi.org/https://doi.org/10.1016/j.palaeo.2016.06.027>
- Zou, J., & Rezaee, R. (2019). A prediction model for methane adsorption capacity in shale gas reservoirs. *Energies*, *12*(2). <https://doi.org/10.3390/en12020280>

APPENDIX

Table 3.1 Summary of experimental procedures and associated results attained.

Study	Experiment	Result
Mineralogical study	Thin section analysis and XRD	Identification and quantification of minerals in shale samples.
Elemental analysis	XRF and ICPMS	To determine major, trace and rare earth elements (REE) to elucidate paleoredox, paleoclimate, provenance and tectonic setting.
Mineralogical and morphological analysis	SEM	To validate the mineral identified by other proxies and identify pore types in samples.
Source rock potential	RockEval pyrolysis and FTIR	To determine organic matter type and abundance, thermal maturity and hydrocarbon potential.

Maceral analysis	Organic petrography	Identification of macerals and determining VRo%.
Biomarker analysis	GC-MS	To support and validate paleoenvironmental interpretations.
Stable isotope analysis	GC-IRMS	To support and validate paleoclimate and paleoproductivity interpretations.
Adsorption isotherms and pore characteristics	Adsorption analysis by the BET method	To quantify micropore volume and understand pore size distribution.

Table 4.1 Semi-quantitative mineral assessment (%) and associated brittleness index for selected Kommugudem shale samples.

Sample	Depth (m)	Quartz	Feldspar	Muscovite	Kaolinite	Illite (\pm mica)	Chlorite (Chamosite)	Siderite	Dolomite	Pyrite	BI-I	BI-II	BI-III
A/C8/B 1	3342	81.01	4.83	0.00	1.09	6.86	6.21	0.00	0.00	0.00	83.75 %	84.52 %	85.83 %
A/C8/B 2	3342.9	78.91	5.99	0.00	2.80	6.25	6.06	0.00	0.00	0.00	74.36 %	75.73 %	84.90 %
A/C8/B 3	3343.1	81.42	4.93	0.00	0.00	6.81	6.84	0.00	0.00	0.00	85.34 %	86.06 %	86.35 %
A/C8/B 4	3344.2	79.13	5.99	0.00	0.00	0.84	5.09	1.38	0.00	7.56	92.51 %	93.10 %	93.98 %
A/C8/B 5	3345.4	63.55	5.02	0.00	0.00	0.94	4.13	25.19	0.00	1.16	91.44 %	94.03 %	93.22 %
A/C8/B 6	3346	79.50	3.73	0.00	3.97	3.30	6.38	3.11	0.00	0.00	84.48 %	85.54 %	85.90 %
A/C9/B 1	3395.2	82.53	3.94	0.00	3.21	3.99	6.33	0.00	0.00	0.00	85.02 %	85.61 %	86.47 %
A/C9/B 3	3397.5	80.15	4.40	0.00	3.28	3.71	6.29	2.17	0.00	0.00	84.63 %	85.62 %	86.43 %
A/C9/B 4	3398.5	81.47	3.74	0.00	3.29	5.00	6.50	0.00	0.00	0.00	82.85 %	83.48 %	85.21 %

A/C9/B 6	3399.5	79.51	5.41	0.00	3.52	4.85	6.70	0.00	0.00	0.00	63.50 %	65.01 %	84.92 %
A/C10/ B1	3466	72.31	5.86	0.00	3.55	8.85	6.38	0.00	0.00	3.06	77.87 %	79.18 %	81.22 %
A/C10/ B2	3470	80.13	4.68	0.00	4.43	4.47	6.28	0.00	0.00	0.00	77.29 %	78.27 %	84.81 %
A/C11/ B2	3669	89.03	1.82	0.00	1.01	0.35	7.80	0.00	0.00	0.00	90.49 %	90.66 %	90.84 %
A/C11/ B5	3672	90.82	1.45	0.00	0.39	0.00	7.34	0.00	0.00	0.00	91.98 %	92.10 %	92.27 %
A/C12/ B5	3834.5	62.13	30.36	0.00	0.00	2.18	5.33	0.00	0.00	0.00	88.20 %	91.76 %	92.49 %
A/C12/ B7	3835.5	68.15	25.36	0.00	0.00	1.21	5.28	0.00	0.00	0.00	91.00 %	93.28 %	93.51 %
A/C13/ B1	4202.8	59.87	35.13	0.00	0.00	0.00	5.00	0.00	0.00	0.00	90.96 %	94.10 %	95.00 %
A/C13/ B2	4203.4	54.70	35.65	2.39	0.00	1.36	4.36	0.00	0.00	0.41	90.24 %	94.00 %	94.07 %
A/C13/ B4	4206	58.54	31.20	0.00	0.00	0.80	5.48	0.00	3.98	0.00	90.66 %	93.57 %	93.46 %
B/C1/B 1	2867.7	73.46	6.69	0.00	4.00	3.42	5.91	6.52	0.00	0.00	83.07 %	85.27 %	85.74 %
B/C1/B 3	2869.5	55.23	6.55	0.00	9.50	4.12	4.39	20.21	0.00	0.00	55.99 %	65.38 %	77.43 %

B/C1/B 5	2871.5	77.40	4.55	0.00	5.82	3.43	6.25	0.00	0.00	0.74	81.70 %	82.54 %	84.22 %
B/C1/B 8	2873.2	88.13	2.29	0.00	0.00	1.62	7.59	0.37	0.00	0.00	88.58 %	88.87 %	90.76 %
B/C1/B 10	2875.2	88.40	2.24	0.00	0.76	0.66	6.80	1.14	0.00	0.00	90.82 %	91.13 %	91.68 %
B/C2/B 1	3192.5	68.37	7.83	0.00	5.61	7.28	8.39	2.53	0.00	0.00	57.42 %	60.83 %	78.18 %
B/C2/B 2	3193.1	82.13	2.90	0.00	4.06	2.30	6.89	1.72	0.00	0.00	85.85 %	86.50 %	86.52 %
B/C2/B 3	3193.5	40.97	7.51	0.00	0.00	0.00	3.63	47.89	0.00	0.00	88.64 %	94.83 %	93.03 %
B/C2/B 5	3196.8	80.30	3.52	0.00	4.74	2.07	6.67	2.71	0.00	0.00	84.66 %	85.60 %	86.15 %
B/C2/B 7	3198.2	73.99	4.98	0.00	4.27	4.22	5.80	6.74	0.00	0.00	79.05 %	81.38 %	84.67 %
B/C2/B 8	3199.2	60.53	6.17	0.00	9.80	8.88	13.26	0.00	0.00	1.36	59.51 %	61.82 %	68.06 %
B/C2/B 10	3200.2	76.57	4.73	0.00	3.57	5.83	8.20	0.00	0.00	1.10	78.75 %	79.73 %	82.40 %
C/C2/B 3	3037.2	87.18	3.64	0.00	0.00	2.36	6.81	0.00	0.00	0.00	90.20 %	90.55 %	90.83 %
C/C2/B 4	3037.5	79.55	6.25	0.00	0.00	3.38	6.51	4.31	0.00	0.00	88.10 %	89.34 %	89.67 %

C/C2/B 7	3040.5	86.80	2.84	0.00	0.00	1.99	7.65	0.71	0.00	0.00	89.93 %	90.28 %	90.29 %
D/C10/ B1	4341.4	78.78	3.91	0.00	4.98	3.18	5.10	4.04	0.00	0.00	83.14 %	84.45 %	86.18 %
D/C10/ B3	4342.5	91.19	2.44	0.00	0.00	0.23	6.14	0.00	0.00	0.00	93.38 %	93.54 %	93.63 %
D/C10/ B4	4343.5	63.35	7.65	0.00	7.01	9.36	10.60	0.00	0.00	2.03	61.42 %	64.08 %	73.03 %
D/C10/ B5	4344.4	80.74	4.30	0.00	3.70	5.24	6.01	0.00	0.00	0.00	80.60 %	81.40 %	85.05 %
D/C10/ B6	4345.4	81.33	3.47	0.00	2.00	1.93	6.23	5.04	0.00	0.00	86.27 %	87.41 %	89.30 %
D/C10/ B7	4346.5	67.91	6.75	0.00	7.58	7.65	8.56	0.00	0.00	1.56	71.12 %	73.03 %	76.22 %
E/C5/B 1	2806.2	71.92	19.00	0.00	0.00	0.00	7.50	0.00	1.58	0.00	90.67 %	92.44 %	92.37 %
E/C5/B 5	2810.5	74.31	11.63	3.82	0.00	0.00	6.63	0.89	2.11	0.61	91.72 %	93.08 %	92.89 %
F/C5/B 4	2937.5	76.66	10.80	0.00	0.00	6.65	5.89	0.00	0.00	0.00	85.88 %	87.41 %	87.46 %
F/C5/B 6	2939.2	85.82	2.82	0.00	0.90	3.96	6.50	0.00	0.00	0.00	88.28 %	88.61 %	88.64 %
F/C5/B 7	2940.5	60.80	32.66	0.00	0.00	2.02	4.52	0.00	0.00	0.00	90.15 %	93.36 %	93.46 %

F/C6/B 3	2969.5	78.00	10.45	0.00	0.00	3.53	6.40	1.63	0.00	0.00	88.58 %	89.95 %	89.91 %
F/C6/B 4	2970.2	85.55	5.10	0.00	0.00	2.03	7.32	0.00	0.00	0.00	90.04 %	90.54 %	90.64 %
F/C7/B 1	3876.6	56.86	33.60	0.00	0.00	3.48	6.07	0.00	0.00	0.00	84.77 %	89.85 %	90.45 %
F/C7/B 2	3877.7	65.16	29.22	0.00	0.00	0.00	5.61	0.00	0.00	0.00	91.29 %	93.82 %	94.39 %
F/C7/B 3	3878.5	62.94	30.18	0.00	0.00	1.31	5.57	0.00	0.00	0.00	89.65 %	92.76 %	93.12 %
F/C7/B 5	3879.3	55.82	34.82	0.00	0.00	2.53	6.84	0.00	0.00	0.00	84.80 %	90.06 %	90.64 %
F/C7/B 6	3880.5	65.22	28.76	1.21	0.00	0.00	4.81	0.00	0.00	0.00	92.94 %	95.05 %	95.13 %
F/C7/B 8	3881.2	57.23	31.62	0.00	0.00	3.43	7.71	0.00	0.00	0.00	83.05 %	88.38 %	88.86 %

Table 4.2 Major Oxide distribution (wt %) in the Kommugudem Formation.

Sample	SiO₂	Al₂O₃	Fe₂O₃	MnO	MgO	CaO	Na₂O	K₂O	TiO₂	P₂O₅	SO₃
A/C8/B1	62.77	21.48	1.56	0.01	1.50	0.14	0.48	5.45	1.00	0.05	0.06
A/C8/B2	61.14	22.75	1.71	0.01	1.25	0.14	0.38	4.36	1.01	0.07	0.13
A/C9/B6	55.10	23.16	1.44	0.01	0.88	0.14	0.20	2.62	1.05	0.05	0.83
A/C10/B1	59.15	24.74	2.28	0.01	1.33	0.21	0.41	5.18	1.16	0.38	0.41
A/C10/B2	64.83	21.06	1.82	0.01	1.26	0.12	0.28	3.18	1.18	0.04	0.10
A/C12/B5	60.63	16.68	5.11	0.08	3.17	0.75	1.52	3.80	0.78	0.19	0.02
A/C13/B1	59.81	17.21	6.74	0.08	3.70	1.64	1.75	3.48	1.06	0.32	0.04
A/C13/B4	66.28	15.24	4.63	0.05	1.91	2.34	2.70	2.66	0.46	0.21	0.02
B/C1/B1	58.89	19.47	4.37	0.10	1.28	0.17	0.35	3.30	1.07	0.05	0.02
B/C1/B3	45.04	18.22	12.02	0.13	0.65	0.64	0.15	2.32	0.93	0.14	1.32
B/C1/B8	61.75	22.44	1.82	0.04	1.08	0.21	0.57	4.51	1.49	0.07	0.30
B/C2/B1	57.92	24.72	1.59	0.01	1.13	0.16	0.21	3.44	1.14	0.05	0.65
B/C2/B8	39.03	15.00	0.61	0.01	0.08	0.15	0.10	1.31	0.86	0.02	2.36
B/C2/B10	72.23	20.06	0.24	0.004	0.69	0.15	0.32	2.90	1.76	0.03	0.13
C/C2/B4	59.21	16.27	7.07	0.12	3.78	1.71	2.57	3.88	1.14	0.22	0.01
D/C10/B1	58.42	20.61	4.60	0.07	1.25	0.22	0.18	2.60	0.89	0.04	0.07
D/C10/B5	59.66	23.28	2.12	0.01	1.27	0.18	0.21	3.51	1.04	0.04	0.21
D/C10/B7	54.91	20.73	5.95	0.11	1.58	0.23	0.20	3.05	1.23	0.04	0.08
E/C5/B5	61.13	17.05	6.65	0.10	2.66	1.51	1.75	4.31	0.93	0.23	0.02
F/C7/B1	55.41	17.13	6.25	0.18	2.75	0.39	0.33	4.06	1.34	0.10	0.04
AS	58.50	15.00	4.72	-	2.50	3.10	1.30	3.10	0.77	0.16	-

Table 4.3 Depositional environment and paleoproductivity parameters for Kommugudem shales.

Sample	K ₂ O/ Al ₂ O ₃	Al ₂ O ₃ / TiO ₂	Mgo+ Fe ₂ O ₃	EF(Ti)	TCP (Ti)	Ti/Al	P/Al	P/Ti	K/Al	Mg/Al	CIW	CIA	ICV
A/C8/B1	0.25	21.53	3.05	0.99	1.28	0.05	0.002	0.04	0.40	0.08	97.18	77.9 5	0.47
A/C8/B2	0.19	22.52	2.96	0.94	1.29	0.05	0.003	0.05	0.30	0.06	97.77	82.3 4	0.39
A/C9/B6	0.11	22.10	2.32	0.96	1.34	0.05	0.002	0.03	0.18	0.04	98.56	88.6 6	0.27
A/C10/B 1	0.21	21.33	3.61	1.00	1.49	0.05	0.013	0.24	0.33	0.06	97.54	81.0 1	0.43
A/C10/B 2	0.15	17.88	3.08	1.19	1.51	0.06	0.001	0.02	0.24	0.07	98.16	85.4 9	0.37
A/C12/B 5	0.23	21.33	8.28	1.00	1.00	0.05	0.009	0.17	0.36	0.22	88.01	73.3 2	0.91
A/C13/B 1	0.20	16.19	10.44	1.31	1.36	0.07	0.015	0.22	0.32	0.25	83.56	71.4 9	1.07
A/C13/B 4	0.17	33.05	6.53	0.64	0.59	0.03	0.011	0.33	0.27	0.14	75.14	66.4 2	0.97
B/C1/B1	0.17	18.14	5.65	1.17	1.38	0.06	0.002	0.03	0.27	0.07	97.40	83.6 2	0.55
B/C1/B3	0.13	19.65	12.67	1.08	1.19	0.06	0.006	0.11	0.20	0.04	98.35	87.4 2	0.92

B/C1/B8	0.20	15.08	2.90	1.41	1.91	0.08	0.003	0.03	0.31	0.05	96.65	80.9 4	0.43
B/C2/B1	0.14	21.69	2.72	0.98	1.46	0.05	0.002	0.03	0.22	0.05	98.54	86.6 6	0.31
B/C2/B8	0.09	17.52	0.69	1.21	1.10	0.06	0.001	0.02	0.14	0.01	98.74	90.9 0	0.21
B/C2/B1 0	0.14	11.40	0.93	1.87	2.26	0.10	0.001	0.01	0.23	0.04	97.71	85.6 0	0.30
C/C2/B4	0.24	14.28	10.85	1.49	1.46	0.08	0.011	0.14	0.37	0.26	79.21	66.6 3	1.25
D/C10/B 1	0.13	23.24	5.84	0.92	1.14	0.05	0.001	0.03	0.20	0.07	98.29	87.4 6	0.48
D/C10/B 5	0.15	22.45	3.40	0.95	1.33	0.05	0.002	0.03	0.24	0.06	98.38	85.6 8	0.36
D/C10/B 7	0.15	16.91	7.53	1.26	1.57	0.07	0.001	0.02	0.23	0.09	98.13	85.7 6	0.60
E/C5/B5	0.25	18.39	9.31	1.16	1.19	0.06	0.011	0.18	0.40	0.18	83.96	69.2 7	1.05
F/C7/B1	0.24	12.80	9.00	1.66	1.72	0.09	0.005	0.05	0.37	0.18	96.33	78.4 1	0.89

Table 4.4 Aluminum normalized trace elements concentration (ppm) in Kommugudem Formation.

Sample	Sc	Co	Ni	Cu	Zn	Ga	Pb	Th	Rb	U	Sr	Y	Zr	Nb	Ba	Cr	Mo	V
A/C8/B 1	0.8 0	0.8 4	0.9 6	0.6 9	0.26	1.2 6	0.8 2	1.5 9	1.48	0.1 7	0.27	0.7 1	0.94	1.1 1	0.98	0.76	0.3 5	0.76
A/C9/B 4	0.7 8	1.7 2	0.3 9	0.6 7	0.67	1.2 8	0.7 2	1.5 2	0.99	0.4 0	0.37	0.5 7	1.18	1.1 4	0.78	0.69	0.5 2	0.68
A/C13/ B1	1.2 4	2.6 6	0.7 4	1.1 2	1.54	1.2 0	0.8 0	2.7 8	1.04	1.5 4	0.69	1.0 7	1.76	1.1 5	1.54	1.45	1.1 5	1.29
B/C1/B3	2.3 6	1.4 3	1.2 3	1.3 9	3.49	1.4 1	1.1 7	2.2 0	1.18	2.0 6	0.19	1.3 7	1.25	1.1 6	0.86	1.51	1.4 7	1.47
B/C2/B1	1.3 2	1.3 6	0.6 2	0.6 3	1.18	1.5 6	3.6 7	1.0 5	1.04	0.9 7	0.29	0.9 7	1.40	1.3 4	0.77	0.64	0.8 0	0.62
B/C2/B1 0	1.0 2	1.6 7	0.2 7	0.3 8	0.24	1.6 1	1.0 9	2.2 6	0.86	0.3 8	0.22	0.6 9	2.03	2.1 8	0.77	0.81	2.5 1	0.78
C/C2/B4	1.0 8	4.3 9	0.5 8	0.4 2	0.80	1.2 1	0.3 0	1.2 5	0.73	0.0 0	0.16	0.5 3	1.19	0.6 8	0.55	2.15	1.9 9	1.08
D/C10/ B5	0.7 4	3.4 9	0.4 2	0.5 5	0.51	1.0 6	0.5 2	1.7 0	0.58	0.1 4	0.15	0.5 2	1.45	0.8 2	0.92	0.82	0.7 2	0.69
E/C5/B5	1.0 4	1.4 7	1.1 4	1.1 0	1.12	1.7 7	0.7 3	2.8 2	0.95	0.6 8	0.56	0.8 6	0.80	1.1 3	1.66	1.66	0.8 4	1.16
F/C7/B8	1.1 1	2.0 8	1.2 6	1.3 3	1.23	1.5 0	0.7 4	3.2 9	1.62	0.7 3	0.82	1.1 6	0.64	1.2 1	2.12	1.71	1.0 3	1.18
EF (AS)	1.5 0	2.1 5	7.7 0	5.1 0	10.7 0	2.1 0	2.3 0	1.4 0	15.8 0	0.4 2	33.9 0	4.6 0	18.1 0	2.0 0	65.6 0	10.2 0	0.2 9	14.7 0

Table 4.5 REE concentrations (ppm) in Kommugudem Formation, KG Basin.

Samp le	La	Ce	Pr	Nd	Sm	E u	Gd	T b	D y	H o	Er	T m	Y b	L u	LREE/ HREE	LaN/ YbN	GdN/ YbN	Eu/ Eu*	Ce/ Ce*
A/C8/ B1	39. 92	82.6 7	8.1 8	32. 37	6.2 2	1. 44	4.9 2	0. 89	5. 53	1. 17	3. 72	0. 54	3. 38	0. 54	8.25	0.87	0.88	1.22	1.06
A/C9/ B4	59. 66	116. 21	11. 54	45. 80	8.2 3	1. 70	5.7 4	0. 91	5. 29	1. 12	3. 67	0. 54	3. 40	0. 55	11.46	1.30	1.02	1.16	1.02
A/C1 3/B1	81. 44	155. 85	16. 29	66. 56	12. 64	2. 42	10. 05	1. 69	9. 66	1. 94	5. 77	0. 79	4. 70	0. 73	9.49	1.28	1.29	1.01	0.99
B/C1/ B3	18. 56	42.3 0	4.2 1	18. 14	4.0 7	0. 93	3.9 2	0. 78	5. 18	1. 17	3. 69	0. 55	3. 42	0. 55	4.58	0.40	0.69	1.10	1.10
B/C2/ B1	53. 40	100. 20	10. 49	42. 13	8.1 0	1. 63	6.5 0	1. 21	7. 69	1. 71	5. 39	0. 78	4. 59	0. 74	7.55	0.86	0.86	1.06	0.98
B/C2/ B10	49. 47	94.1 3	9.3 9	37. 20	7.6 6	1. 48	6.0 9	1. 02	5. 67	1. 09	3. 24	0. 45	2. 72	0. 43	9.62	1.35	1.36	1.02	1.01
C/C2/ B4	9.1 1	25.4 6	3.0 2	14. 29	3.1 3	0. 82	2.5 6	0. 39	2. 05	0. 39	1. 20	0. 18	1. 17	0. 19	6.88	0.57	1.32	1.36	1.12
D/C1 0/B5	68. 50	130. 53	13. 02	51. 65	8.8 6	2. 29	6.4 9	0. 98	5. 29	1. 09	3. 53	0. 52	3. 23	0. 55	12.69	1.56	1.21	1.43	1.01
E/C5/ B5	90. 57	167. 17	16. 87	68. 48	12. 46	2. 35	9.2 9	1. 48	7. 90	1. 52	4. 51	0. 62	3. 70	0. 57	12.10	1.81	1.52	1.03	0.99
F/C7/ B8	87. 28	172. 58	18. 07	75. 59	14. 80	2. 54	11. 24	1. 78	9. 54	1. 82	5. 26	0. 69	4. 02	0. 63	10.60	1.60	1.69	0.93	1.00
PAAS	38. 20	79.6 0	8.8 3	33. 90	5.5 5	1. 08	4.6 6	0. 77	4. 68	0. 99	2. 85	0. 41	2. 82	0. 43	-	-	-	-	-

Table 4.6 Paleoredox, paleoclimate and paleosalinity indicators are considered in Kommugudem shales of the KG Basin.

Sample	Redox								Paleoclimate			Paleosalinity
	Ni/Co	U/Th	V/Cr	Cu/Zn	U/Al	δU	Mo/TOC	V/(V+N i)	C	Sr/Cu	Ga/Rb	Rb/K
A/C8/B1	4.10	0.03	1.46	1.24	0.07	0.17	0.77	0.60	0.38	2.56	0.11	0.007
A/C9/B4	0.81	0.08	1.43	0.47	0.17	0.38	0.92	0.77	0.37	3.74	0.17	0.007
A/C13/B1	1.00	0.17	1.29	0.35	0.65	0.67	3.05	0.77	0.37	4.08	0.15	0.005
B/C1/B3	3.08	0.28	1.4	0.19	0.86	0.91	0.13	0.69	0.81	0.91	0.16	0.007
B/C2/B1	1.62	0.28	1.38	0.25	0.41	0.91	0.09	0.66	0.39	3.05	0.2	0.007
B/C2/B10	0.58	0.05	1.38	0.75	0.16	0.27	2.17	0.85	0.44	3.72	0.25	0.006
C/C2/B4	0.47	0	0.72	0.25	0.00	0.00	6.88	0.78	1.26	2.45	0.22	0.004
D/C10/B5	0.44	0.02	1.21	0.52	0.06	0.13	0.63	0.76	0.45	1.82	0.24	0.005
E/C5/B5	2.79	0.07	1.01	0.47	0.28	0.36	8.04	0.66	0.36	3.36	0.25	0.005
F/C7/B8	2.16	0.07	0.99	0.51	0.31	0.33	4.56	0.64	0.30	4.09	0.12	0.006

Table 5.1 RockEval-VI pyrolysis data of the Kommugudem Formation. Abbreviations: S1 = total free hydrocarbon; S2 = hydrocarbon released by cracking of kerogen; S3 = organic carbon dioxide; Tmax =Temperature at which the maximum amount of pyrolyzed hydrocarbon (S2 peak) is generated from the kerogen; Hydrogen Index, HI= [100 × S2]/TOC; Oxygen Index, OI=[100×S3]/TOC; Production Index, PI = S1/[S1+S2]; TOC= Total organic carbon; Generation potential, GP= S1+S2; PC: Principle carbon content ; RC: Residual carbon content.

Sample name	Depth (m)	S1 (mg HC/g rock)	S2 (mg HC/g rock)	S3 (mg CO2/g rock)	Tmax (°C)	HI (mg HC/g TOC)	OI (mg CO2/g TOC)	PI (mg HC/g TOC)	TOC (%)	GP (mg HC/g TOC)	PC (%)	RC (%)
A/C8/B1	3342.00	0.09	0.43	0.21	523	28	14	0.17	1.55	0.52	0.05	1.5
A/C8/B2	3342.90	0.69	7.82	0.75	470	65	6	0.08	12.11	8.51	0.77	11.34
A/C8/B3	3343.10	0.04	0.14	0.13	431	41	38	0.21	0.34	0.18	0.02	0.32
A/C8/B4	3344.20	0.05	0.06	0.15	447	13	32	0.42	0.47	0.11	0.02	0.45
A/C8/B5	3345.40	0.05	0.23	1.83	464	26	208	0.19	0.88	0.28	0.33	0.55
A/C8/B6	3346.00	0.05	0.32	0.92	509	34	98	0.14	0.94	0.37	0.07	0.87
A/C9/B1	3395.20	0.1	0.34	0.31	498	34	31	0.22	1.01	0.44	0.05	0.96
A/C9/B3	3397.50	0.07	0.27	0.4	526	21	31	0.2	1.28	0.34	0.04	1.24
A/C9/B4	3398.50	0.2	0.82	0.32	485	40	15	0.19	2.07	1.02	0.1	1.97
A/C9/B6	3399.50	2.67	20.26	1.35	479	66	4	0.12	30.63	22.93	2.08	28.55
A/C10/B1	3466.00	0.07	0.44	0.31	495	25	18	0.13	1.77	0.51	0.06	1.71
A/C10/B2	3470.00	0.42	3.91	0.52	509	47	6	0.1	8.35	4.33	0.41	7.94
A/C11/B2	3669.00	0.03	0.12	0.11	400	60	55	0.22	0.2	0.15	0.03	0.17

A/C11/B5	3672.00	0.04	0.15	0.14	413	83	78	0.2	0.18	0.19	0.03	0.15
A/C12/B5	3834.50	0.04	0.17	0.1	503	21	12	0.2	0.8	0.21	0.03	0.77
A/C12/B7	3835.50	0.03	0.09	0.14	517	36	56	0.26	0.25	0.12	0.02	0.23
A/C13/B1	4202.80	0.05	0.14	0.17	497	15	18	0.25	0.95	0.19	0.02	0.93
A/C13/B2	4203.40	0.04	0.12	0.11	489	60	55	0.25	0.2	0.16	0.02	0.18
A/C13/B4	4206.00	0.04	0.12	0.4	484	75	250	0.25	0.16	0.16	0.03	0.13
B/C1/B1	2867.70	0.15	0.84	2.2	432	51	134	0.15	1.64	0.99	0.18	1.46
B/C1/B3	2869.50	4.76	41.06	1.94	444	162	8	0.1	25.4	45.82	4.06	21.34
B/C1/B5	2871.50	0.14	1.12	0.6	453	61	33	0.11	1.84	1.26	0.13	1.71
B/C1/B8	2873.20	0.26	1.46	1.02	469	68	47	0.15	2.16	1.72	0.23	1.93
B/C1/B10	2875.20	0.02	0.27	0.65	429	38	92	0.05	0.71	0.29	0.05	0.66
B/C2/B1	3192.50	3.81	25.04	1.07	464	85	4	0.13	29.42	28.85	2.53	26.89
B/C2/B2	3193.50	0.03	0.13	0.6	464	45	207	0.21	0.29	0.16	0.04	0.25
B/C2/B3	3194.40	0.09	0.33	10.88	456	20	672	0.22	1.62	0.42	0.91	0.71
B/C2/B5	3196.80	0.07	0.28	1	482	26	93	0.2	1.07	0.35	0.06	1.01
B/C2/B7	3198.20	0.31	1.88	1.89	473	35	36	0.14	5.31	2.19	0.27	5.04
B/C2/B8	3199.20	1.05	6.16	0.77	458	67	8	0.15	9.25	7.21	0.64	8.61
B/C2/B10	3200.20	0.21	1.25	0.35	525	41	11	0.15	3.07	1.46	0.14	2.93
C/C2/B3	3037.20	0.04	0.2	0.34	469	67	113	0.17	0.3	0.24	0.03	0.27
C/C2/B4	3037.50	0.08	0.43	0.98	477	50	114	0.16	0.86	0.51	0.1	0.76
C/C2/B7	3040.50	0.02	0.04	0.53	446	50	662	0.32	0.08	0.06	0.02	0.06
D/C10/B1	4341.40	0.09	0.22	0.23	607	8	8	0.28	2.71	0.31	0.04	2.67
D/C10/B3	4342.50	0.03	0.07	0.22	317	78	244	0.28	0.09	0.1	0.02	0.07
D/C10/B4	4343.50	0.63	1.46	0.25	607	11	2	0.3	12.82	2.09	0.2	12.62

D/C10/B5	4344.40	0.09	0.27	0.18	607	6	4	0.25	4.48	0.36	0.04	4.44
D/C10/B6	4345.40	0.23	0.27	6.64	604	10	239	0.46	2.78	0.5	0.24	2.54
D/C10/B7	4346.50	0.09	0.22	0.13	607	6	3	0.3	3.79	0.31	0.04	3.75
E/C5/B1	2806.20	0.02	0.07	0.23	328	117	383	0.26	0.06	0.09	0.02	0.04
E/C5/B5	2810.50	0.05	0.16	0.22	485	59	81	0.24	0.27	0.21	0.03	0.24
F/C5/B4	2937.50	0.02	0.05	0.13	322	83	217	0.34	0.06	0.07	0.01	0.05
F/C5/B6	2939.20	0.02	0.04	0.14	356	133	467	0.35	0.03	0.06	0.01	0.02
F/C5/B7	2940.50	0.03	0.14	0.06	476	140	60	0.18	0.1	0.17	0.02	0.08
F/C6/B3	2969.50	0.04	0.16	0.07	505	114	50	0.19	0.14	0.2	0.02	0.12
F/C6/B4	2970.80	0.03	0.12	0.05	475	109	45	0.18	0.11	0.15	0.01	0.1
F/C7/B1	3876.60	0.06	0.23	0.09	507	34	13	0.21	0.67	0.29	0.03	0.64
F/C7/B2	3877.70	0.04	0.08	0.16	499	13	27	0.34	0.6	0.12	0.02	0.58
F/C7/B3	3878.50	0.03	0.05	0.12	498	13	31	0.35	0.39	0.08	0.01	0.38
F/C7/B5	3879.30	0.04	0.09	0.18	511	14	28	0.28	0.64	0.13	0.02	0.62
F/C7/B6	3880.50	0.01	0.01	0.27	486	7	193	0.67	0.14	0.02	0.01	0.13
F/C7/B8	3881.20	0.04	0.09	0.16	515	17	30	0.3	0.54	0.13	0.02	0.52

Table 5.2 Vitrinite reflectance data of shale samples from the Kommugudem Formation.

Sample name	Depth (m)	Vitrinite Reflectance (VRo%) range	Mean VRo (%)	Estimated VRo (ERo%)
A/C9/B6	3399.5	1.21-1.36	1.25	1.46
A/C10/B2	3470	0.97-1.25	1.08	2.00
B/C1/B3	2869.5	0.77-0.89	0.83	0.83
B/C2/B8	3199.2	1.12-1.29	1.21	1.08
C/C2/B4	3037.5	0.80-1.09	0.94	1.42
D/C10/B1	4341.4	1.43-1.76	1.55	3.77
D/C10/B7	4346.5	1.40-1.88	1.64	3.77
E/C5/B5	2810.5	0.61-0.90	0.74	1.57
F/C7/B1	3876.6	0.70-0.97	0.83	1.97

Table 5.3 *n*-alkane biomarker ratios for Kommugudem shales.

Sample	Depth (m)	Pr/Ph	Paq	Pwax	Pr/n- C17	Ph/n- C18	ACL	TAR	CPI- 1	CPI- 2	CPI	OEP1	OEP2
A/C8/B2	3342.9	0.94	0.99	0.05	0.19	0.19	25.32	0.01	1.12	1.08	1.11	1.04	0.90
A/C9/B6	3399.5	0.56	0.97	0.12	0.19	0.19	25.69	0.06	1.04	1.11	1.02	0.92	0.91
A/C10/B2	3470	1.31	1.00	0.00	0.36	0.22	25.00	0.00	1.01	1.05	1.01	1.04	0.41
B/C1/B3	2869.5	0.80	0.96	0.15	0.34	0.29	25.87	0.07	1.00	1.14	0.99	0.94	0.98
B/C1/B8	2873.2	0.57	0.95	0.14	0.29	0.31	25.88	0.07	0.94	1.05	0.91	0.97	0.78
B/C2/B1	3192.5	0.64	0.97	0.12	0.10	0.11	25.74	0.04	0.99	1.13	0.97	0.97	0.86
B/C2/B7	3198.2	0.63	1.00	0.08	0.24	0.23	25.40	0.04	1.08	1.06	1.08	0.98	1.10
B/C2/B8	3199.2	0.66	0.95	0.16	0.39	0.37	25.99	0.07	1.00	1.13	0.98	0.98	0.93
B/C2/B10	3200.2	0.92	0.95	0.16	0.21	0.21	25.92	0.05	1.05	1.49	1.01	0.92	1.10
C/C2/B4	3037.5	1.23	0.90	0.23	0.26	0.16	26.34	0.14	0.99	1.11	0.97	0.97	0.96
D/C10/B1	4341.4	0.64	1.00	0.10	0.29	0.30	25.56	0.02	0.89	0.99	0.89	0.89	1.05
D/C10/B5	4344.4	0.93	0.97	0.15	0.30	0.23	25.86	0.04	0.90	1.01	0.89	0.89	0.87
D/C10/B7	4346.5	0.21	1.00	0.02	0.06	0.19	25.17	0.01	0.91	1.04	0.91	0.97	0.63

E/C5/B5	2810.5	0.77	1.00	0.12	0.38	0.29	25.54	0.05	1.00	0.97	1.00	0.94	1.08
F/C7/B1	3876.6	0.60	0.97	0.17	0.28	0.29	25.94	0.06	0.88	1.06	0.86	0.93	0.80

Table 5.4 Peak assignment of absorbance of the shales from FTIR spectral analysis. Abbreviations: M=medium and W=weak.

Wavelength	Peak Assignment	Characteristic absorbance intensities									
		E/C5/B5	B/C1/B1	B/C1/B3	B/C1/B5	C/C2/B4	A/C8/B2	A/C9/B6	F/C7/B1	D/C10/B 1	D/C10/B 6
3600–3100	-OH stretching vibrations	W	M	W	M	M	M	M	M	M	M
3100–3000	Aromatic C-H stretching vibrations	W	W	W	W	W	W	W	W	W	W
3000–2800	Aliphatic C-H stretching vibrations	W	W	W	W	W	M	M	M	W	M
2960	Asymmetric aliphatic CH ₃ stretching vibration	W	W	W	W	W	W	W	W	W	W
2920	Asymmetric aliphatic CH ₂ stretching vibration	W	W	W	W	W	M	M	M	W	M
2850	Symmetric aliphatic CH ₃ stretching vibration	W	W	W	W	W	M	M	M	W	M
1700	Aliphatic C=O and -COOH stretching vibrations	W	W	W	W	W	W	W	W	W	W
1680–1500	Aromatic C=C stretching modes	W	W	W	W	M	M	M	W	M	M
1650	Aromatic C=O stretching vibration	W	W	W	W	W	W	W	W	W	W
1600	Aromatic C=C stretching vibrations of aromatic rings	W	W	W	W	M	M	M	W	M	M
1460	Aromatic C=C stretching vibration	W	W	W	W	W	W	W	W	W	W
1435	Aliphatic CH ₂ and CH ₃ bending vibration	W	W	W	W	M	M	M	W	M	M
	1400-680	Masked by mineral matter									
		0.4	5.1	0.5	0.6	0.6	0.7	0.6	0.6	0.53	0.62
	IAL	4	6	6	3	2	4	9	4		

	0.5	3.2	0.4	0.3	0.3	0.2	0.3	0.3	0.47	0.38
IAR	6	5	4	7	8	6	1	6		
	25.	263	90.	38.	30.	48.	45.	21.	4.24	6.22
IHG	94	.12	01	31	80	15	29	67		

Table 6.1 Pore characterization parameters estimated from low-pressure N₂ adsorption isotherm experiment.

Sample Name	BET-SSA (m²/g)	Total PV (cc/g)	Micropore Volume (cc/g)	Average Pore Diameter (nm)	Fractal dimension (D)
K1	11.37	0.04	0.004	36.0845	2.66
K4	11.39	0.03	0.004	36.0761	2.75
M5	3.11	0.01	0.001	-	2.66
M8	2.47	0.01	0.001	34.7975	2.59
D2	24.57	0.08	0.003	26.2226	2.60

CURRICULUM VITAE WITH LIST OF PUBLICATIONS

SHUBHANGI KALA

DST-INSPIRE FELLOW (SRF)

Department of Petroleum Engineering and Earth Science

University of Petroleum and Energy Studies, India.

Email: kalashubhangi@gmail.com

Contact No.: +91-9998183471

WORK EXPERIENCE

Senior Research Fellow (SRF), Inspire scheme of Department of Science and Technology (Govt. of India) for the duration of September 2019-August 2022.

Junior Research Fellow (JRF), Inspire scheme of Department of Science and Technology (Govt. of India) for the duration of March 2016-August 2019.

RESEARCH INTEREST

Gondwana climate and paleoenvironment, petrography, analytical and organic geochemistry.

EDUCATION

DEGREE	INSTITUTE/BOARD	YEAR
M.Sc. (Geology)	The M.S. University of Baroda, Vadodara, India	2015
B.Sc. (Geology)	The M.S. University of Baroda, Vadodara, India	2013

PROFESSIONAL MEMBERSHIP

1. EAG student member.
2. EAGE student member.
3. TSOP student member.

JOURNAL PUBLICATIONS

1. **Kala, S.,** Devaraju, J., De, S., & Rasheed, M. A. (2022). Multiproxy geochemical characterization of Kommugudem Formation, Krishna Godavari Basin, India: Implication on hydrocarbon potential and shale brittleness. *Geological Journal*, 57(4), 1373-1390. <https://doi.org/10.1002/gj.4346>

(Journal Info: IF: 2.5; Q1; SCIE indexed)

2. **Kala, S.,** Devaraju, J., Tiwari, D. M., Rasheed, M. A., & Lakhan, N. (2021). Organic petrology and geochemistry of Early Permian shales from the Krishna-Godavari Basin, India: Implications for Gondwana paleoenvironment and climate. *Geological Journal*, 56(11), 5621– 5641. <https://doi.org/10.1002/gj.4262>

(Journal Info: IF: 2.5; Q1; SCIE indexed)

3. **Kala, S.,** Turlapati, V. Y., Devaraju, J., Rasheed, M. A., Sivaranjane, N., & Ravi, A. (2021). Impact of sedimentary environment on pore parameters of thermally mature Permian shale: A study from Kommugudem Formation of Krishna Godavari Basin, India. *Marine and Petroleum Geology*, 132, 105236. <https://doi.org/https://doi.org/10.1016/j.marpetgeo.2021.105236>

(Journal Info: IF: 4.5; Q1; SCIE indexed)

CONFERENCE AND WORKSHOPS

1. **Kala, S.,** Devaraju, J., & Rasheed, M. A. (2022). Assessment of brittleness and hydrocarbon potential of deep Permian shales in Krishna Godavari Basin, India. **In EGU, General Assembly, Vienna, Austria, EGU22-275.**

2. **Kala, S.,** Boruah, A., Devaraju, J., & Rasheed, M. A. (2019). Facies, Mineralogical and Geochemical Analysis of Permian Shales in Krishna Godavari Basin, India. **In Goldschmidt, Barcelona, Spain, 1592.**

3. Advanced Training Program on Analytical Geochemistry, NGRI, Hyderabad (10th-19th Feb 2020).

4. Unconventional Resources: Shale Gas & CBM Exploration & Exploitation (25th-26th June 2020) (Virtual; UPES).

final

ORIGINALITY REPORT

9%	8%	2%	2%
SIMILARITY INDEX	INTERNET SOURCES	PUBLICATIONS	STUDENT PAPERS

PRIMARY SOURCES

1	Submitted to Indian School of Mines Student Paper	1%
2	www.mdpi.com Internet Source	1%
3	ir.amu.ac.in Internet Source	<1%
4	core.ac.uk Internet Source	<1%
5	theses.dur.ac.uk Internet Source	<1%
6	hdl.handle.net Internet Source	<1%
7	shareok.org Internet Source	<1%
8	pericles.pericles-prod.literatumonline.com Internet Source	<1%